

TOWARDS ON-CHIP INTEGRATED SENSORS:
PHOTONIC CRYSTAL OPTICAL
SENSORS AND LASERS

by
ZHONGHE LIU

Presented to the Faculty of the Graduate School of
The University of Texas at Arlington in Partial Fulfillment
of the Requirements for the degree of

DOCTOR OF PHILOSOPHY
IN ELECTRICAL ENGINEERING

THE UNIVERSITY OF TEXAS AT ARLINGTON

August 2022

Copyright © by ZHONGHE LIU 2022

All Rights Reserved



To my parents Caixia Chen and Yanqi Liu

ACKNOWLEDGEMENTS

My greatest gratitude is for my supervising professor Dr. Weidong Zhou. Dr. Zhou is a passionate scholar and expert in the field of semiconductor optoelectronic devices. His enthusiasms for work have not only inspired and encouraged me to develop high efficiency and productivity in my research in the field of opto-electronics, but also have a great impact on my way of thinking in general. He not only supports me for the work in the lab with ideas and funding opportunities, but also helps me build connections in the industry around the DFW area, which could enormously benefit my career later. It is an honor to have him as my PhD supervisor.

I would like to express my appreciations to my dissertation committee member, Prof. Robert Magnusson, Prof. Yuze (Alice) Sun, Prof. Michael Vasilyev, and Prof. Georgios Alexandrakis. Their guidance and input have made this work more conclusive. My deep gratitude to all the collaborators in my program, Prof. John Rogers from Northwestern University, Dr. Luke Graham from Dallas Quantum Devices, Dr. Jian Liu and Matthew Sampsell from AMS Sensors.

I am also so grateful for the opportunity to work with such a great team, my whole journey in the program would not be as exciting without the collaboration and help from all the wonderful former members, Dr. Hongjun Yang, Dr. Deyin Zhao, Dr. Xiaochen Ge, Dr. Shih-Chia Liu, Dr. Yonghao Liu and Dr. Akhil Kalapala, as well as the current member in the group, Dr. Mingsen Pan, Yudong Chen and Chabindra Gautam.

I appreciate all the training and support from staffs at UTA NanoFab Center, Richard (Kevin) Chambers, Dennis Bueno, and Huan (Mick) Nguyen. Their expertise with the facilities in the cleanroom has made my fabrication a pleasant and enriching experience. I would also like to thank the support from UT Austin MRC and UT Dallas cleanroom, their training and assistance have extended my skills in semiconductor micro fabrication.

Lastly, I am deeply indebted to my family for their unconditional love and support for all these years. My parents have been working so hard endlessly ever since when I was a child. They have suffered poverty, illness, and desperation in the last 40 years, to which I lost my father's life 10 years ago. He was and will always be the hero in my life, supporting me with his undefeated spirit. I am always grateful for the support of my younger brother to me and to the family. All these years I have been pursuing my dreams away from home in college and in graduate schools overseas, he has put countless efforts taking care of the family. It is impossible for me to finish this program without all their love, understanding and support. I cannot wait for the reunion with them and to be with them.

June 23, 2022

ABSTRACT

TOWARDS ON-CHIP INTEGRATED SENSORS: PHOTONIC CRYSTAL OPTICAL SENSORS AND LASERS

ZHONGHE LIU, Ph.D.

The University of Texas at Arlington, 2022

Supervising Professor: Weidong Zhou

The field of compact integrated optical platform has developed into a new era in the past two decades. On one hand, the semiconductor optoelectronic devices are becoming smaller and cheaper thanks to the development of complementary metal-oxide semiconductor (CMOS) fabrication technologies; on the other hand, the applications of optoelectronics have been deeply coupled to other fields to realize more complicated implementations. Photonic crystal slab (PCS) structure has been playing an increasingly important role in these optical devices, active or passive, by enabling a variety of light-matter interaction mechanisms. The objective of this dissertation is to investigate photonic crystal devices towards on-chip integration of optical sensing system. In addition to PCS optical sensing structures, compact photonic crystal lasers and laser cavities are also being investigated. The phase tuning capabilities in PCSs have also been studied theoretically, for applications in high sensitivity sensing, and in phase front engineering for flat optic metalens. The background and motivations of this dissertation will be discussed in more details in Chapter 1.

Bioresorbable implantable optical sensors are an emerging optical sensor which dissolves in the body after pre-defined performance period. As described in Chapter 2, we first investigated the design and fabrication of optical pressure and temperature sensors with standard CMOS process

from bioresorbable materials. Millimeter-scale Fabry-Perot cavities and two-dimensional photonic crystal structures are designed and fabricated entirely with bioresorbable materials to enable precise, continuous measurements of pressure and temperature across physiologically relevant ranges, for clinically relevant timescales before naturally resorbing into the body. Combined mechanical and optical simulations reveal the fundamental sensing mechanisms in both cases. In vitro studies and histopathological evaluations quantify the measurement accuracies, the operational lifetimes, and the biocompatibility of these systems. Demonstrations in intracranial pressure and temperature monitoring in live animal models establish clinically relevant performance attributes.

Large area monolayer 2D material integrated PC laser has also been investigated, as shown in Chapter 3. The viscoelastic stamp transfer technique was developed for large area (over 100 mm sized) monolayer 2D WS₂ material preparation and integration processes. Wafer scale monolayer 2D materials were also used in the project for the demonstration of large array size lasers based on WS₂ material. 2D material transfer-printing process on an automatic assembly platform was also developed for high quality 2D material transfer printing and stacking.

Additionally, photonics crystal nanobeam (PCNB) cavity is an ideal candidate for high performance, low energy consumption and high-speed semiconductor lasers for its superior characteristics of ultra-compact size, extreme low mode volume (V), and high quality (Q) factor. We investigate the design, fabrication, and characterization of suspended arrays of small volume, high quality factor (Q) silicon nitride photonic crystal nanobeam (PCNB) cavities with lateral nanorod fin structures. The work is presented in Chapter 4. By controlling the alignment position of the fins with respect to the air holes, the resonance wavelength and Q-factor of the PCNB cavities can be tuned to realize the desired performance. Measured Q-factors and resonant wavelength tuning ranges of 2×10^4 and 10 nm are achieved respectively, with the highest Q-factor measured at 2.5×10^4 . Incorporating such nanorod fins to the nanobeam cavity is demonstrated to provide improved

mechanical support, thermal transport, and channels of lateral carrier injection for the suspended PCNB.

Finally, as shown in Chapter 5, we investigated reflective and transmissive photonic crystal optical cavities to achieve high sensitivity phase sensing with full 2π phase shift, with great potentials for high-speed phase tuning. Measurement of phase information was also demonstrated on single layer photonic crystal cavities. We also investigated an amorphous silicon photonic crystal slab (PCS) metalens structure with full 2π phase modulation, high transmission efficiency and broadband operation centered at 940 nm. The structure is an ideal candidate for large area phase manipulation with compact, reliable, and low aspect ratio patterning on a thin film. Simulation results show continuous 2π transmission phase control by tuning the air hole filling size near the degenerate band edge, and the metalens structure is achieved with efficiency above 80% and the operation wavelength over 100 nm.

TABLE OF CONTENTS

ACKNOWLEDGEMENTS.....	iv
ABSTRACT.....	vi
TABLE OF CONTENTS.....	ix
LIST OF FIGURES	xii
LIST OF TABLES.....	xvi
CHAPTER 1. INTRODUCTION	1
1.1 Motivation	1
1.2 State of the art	2
1.3 Introduction to photonic crystal	2
1.4 Photonic band gap and mode distribution	6
1.4.1. Photonic bands	6
1.4.2. Two-dimensional (2D) photonic crystal	6
1.5 Different photonic crystal design with applications.....	8
1.5.1. Fano resonance PhC optical filters.....	8
1.5.2. Lateral confinement enhancement with heterostructure PhC	9
1.5.3. 1D defect mode PhC nanobeam cavity	10
1.6 Numerical utilities.....	11
1.6.1. Rigorous coupled wave analysis method with S4.....	11
1.6.2. Finite-difference time-domain (FDTD) method	12
1.6.3. Calculation of photonic bands.....	14
1.7 Fabrication of photonic crystal.....	15
1.7.1. Electron beam lithography.....	15
1.7.2. Reactive ion etching.....	17
1.8 Content overview of the dissertation.....	20

CHAPTER 2. bioresorbable implantable optical SENSORS	22
2.1 Introduction	22
2.2 FPI pressure sensor on fiber tip.....	25
2.2.1. Design and Fabrication	25
2.2.2. FPI pressure sensor integration with fiber, calibration, and temperature influence	28
2.3 Development of FPI and photonic crystal (PhC) temperature sensor	33
2.3.1. Temperature dependence of refractive index of silicon.....	33
2.3.2. Photonic crystal temperature sensor on SOI substrate.....	34
2.3.3. Proposed FPI pressure sensor with PhC feature for temperature compensation	35
2.4 Bio-implantable angle independent free-space temperature sensor.	37
2.4.1. Individual Fabray-Perot and DBR cavities	37
2.4.2. Design, fabrication, and testing of F-P/DBR multilayer temperature sensor	40
2.5 Summary of sensors	44
CHAPTER 3. single sheet 2D material PHOTONIC CRYSTAL LASERS	47
3.1 Introduction	47
3.2 Laterally confined heterostructure 2D photonic crystal cavities	47
3.3 Integrated 2-dimensional material laser	49
3.3.1. Monolayer WS ₂ transfer printing.....	49
3.3.2. Heterostructure PhC laser characterization.....	51
3.3.3. Lattice design comparison	53
3.3.4. 2D material metrology comparison.....	54
CHAPTER 4. PHOTONIC CRYSTAL NANOBEAM cavities with fins.....	56
4.1 Introduction	56
4.2 Photonic crystal nanobeam cavity design	58
4.3 Photonic crystal nanobeam cavity fabrication and measurement.....	60
4.3.1. Fabrication	60

4.3.2.	Measurement and analysis	61
4.4	Summary	64
CHAPTER 5. PHOTONIC CRYSTAL SLAB METALENS.....		66
5.1	Introduction of transmissive photonic crystal metalens	66
5.2	Metalens flat optics constructed by meta-atoms	66
5.2.1.	Polarization dependent meta-atom.....	67
5.2.2.	Polarization independent meta-atom.....	68
5.2.3.	Construction of phase array for focusing lens.....	69
5.2.4.	Focusing lens lattice choice	70
5.2.5.	Spot size dependence on NA	71
5.2.6.	Broad-band operation.....	72
5.3	Transmissive 2π phase on photonic crystal slabs.....	74
5.3.1.	Coupled mode theory and formation of 2π phase continuity.....	75
5.3.2.	Degenerate PC mode and formation of 2π transmission phase.....	77
5.3.3.	Construction of PC metalens.....	79
5.3.4.	Conclusion: PCS versus meta-atoms	80
5.4	Reflective 2π phase transition	82
5.4.1.	Continuous reflection 2π phase on photonic crystal slabs	82
5.4.2.	Tunable sensitivity	84
CHAPTER 6. CONCLUSION REMARKS AND FUTURE RESEARCH		86
6.1	Conclusion.....	86
6.2	Future work	86
LIST OF PUBLICATIONS		88
BIOGRAPHICAL STATEMENT		91
REFERENCES		92

LIST OF FIGURES

Figure 1 A simple sketch of integrated optical system on chip.	1
Figure 2 Periodically arranged materials in one-, two- and three-dimensions.....	3
Figure 3 Photonic band diagram of 1-dimensional multilayer PhC.....	7
Figure 4 Photonic band diagram of a 2D PhC on SOI substrate.....	8
Figure 5 SEM and reflection spectrum of a 2D PhC on SOI substrate.....	9
Figure 6 SEM and reflection spectrum of a 2D PhC on Si ₃ N ₄ substrate.....	10
Figure 7 Schematic of a Nanobeam Cavity Design.	11
Figure 8 Cartoon illustration of the S4 layered structure and coordinates convention.	12
Figure 9 3D sketch models built in Tidy3D.....	13
Figure 10 Photonic band structure calculated in Legume.	14
Figure 11 Spin curve of ZEP520A.....	15
Figure 12 SEM of properly exposed ZEP520A resist on GaAs substrate	17
Figure 13 SEM of PhC on Si	18
Figure 14 SEM of Si ₃ N ₄ PhC slab on Si	19
Figure 15 SEM of GaAs PhC.....	20
Figure 16 SEM of GaAs PhC.....	20
Figure 17 Schematics of FPI pressure sensor	26
Figure 18 Sketch illustration of the FPI pressure sensor fabrication flow	27
Figure 19 Photograph and spectra of FPI pressure sensor calibration.....	29
Figure 20 Illustration of the testing setup for fiber integrated FPI sensors.....	30

Figure 21 Measured spectrum of 10 μ m thick FPI pressure sensor.....	31
Figure 22. Photograph and measured spectra of an FPI temperature sensor	33
Figure 23 Schematic and spectra of PhC temperature sensor.....	35
Figure 24 Sketch and simulated spectra of FPI+PhC sensor	36
Figure 25 Simulated and measured spectra of the Si FPI and Oxide/Nitride BDR Cavities	38
Figure 26 Reflection intensity maps of FPI and DBR cavities.....	39
Figure 27 Structure of the DBR defect temperature sensor	40
Figure 28 DBR temperature sensor fabrication flow.....	41
Figure 29 Measured and simulated spectra of the DBR temperature sensor	42
Figure 30 Measurement principle of the DBR temperature sensor.....	43
Figure 31 Design of the lateral confined heterostructure photonic crystal cavities.....	49
Figure 32 Processing flow of integrating large area synthesized WS ₂ onto Si ₃ N ₄ PhC cavity.	50
Figure 33 Schematics and micrograph of WS ₂ integrated laser.....	51
Figure 34 Optically pumped photonic crystal illumination	52
Figure 35 Laser characteristics of the heterostructure PCSEL	53
Figure 36 Comparison of illumination from rectangular and circular airhole hetero PhC	54
Figure 37 Comparison of laser characteristic from 2 types of WS ₂ material.....	55
Figure 38 Schematics and SEM of suspended nanobeam cavities	57
Figure 39 Design parameters of the nanobeam cavity	59
Figure 40 Simulation of field distribution of nanobeam cavity with and without fins	59
Figure 41 SEM of PCNB with fins in array layout.....	60

Figure 42 Photonic bands and characterization of nanobeam without fins.....	62
Figure 43 Characterization of nanobeam cavity with fins	63
Figure 44 Influence of fin width and airhole radius.....	64
Figure 45 Refractive indices of crystal (c-Si) and amorphous silicon (a-Si).....	67
Figure 46 Schematics and transmission phase of meta-atoms	68
Figure 47 Refractive indices of crystal and amorphous silicon	69
Figure 48 Meta-atoms arranged in different lattices	70
Figure 49 Distribution of $ \mathbf{E} ^2$ on x-z plane for plane wave transmission.....	70
Figure 50 Distribution of $ \mathbf{E} ^2$ on x-z plane for at NA = 0.1~0.9	71
Figure 51 Focal length and spot size for at NA = 0.1~0.9	72
Figure 52 Transmission intensity and phase of nano-rod metalens	73
Figure 53 In-plane phase distribution of the metalens built from the nano-rod metalens	73
Figure 54 Focusing effect of the metalens built from nano-rod meta-atoms.....	74
Figure 55 3D sketch of the coupling ports on a PCS	76
Figure 56 Degerate mode near the high transmission band edge	77
Figure 57 Coupled mode theory analysis of the degenerate mode	78
Figure 58 Optimized PCS continuous phase mode	79
Figure 59 Focusing effect of the metalens built from PCS.....	80
Figure 60 3D sketch of metalens composed of meta-atom and PCS	81
Figure 61 PCS reflective 2π mode.....	82
Figure 62 2π reflection phase on PCS with defferent parameters	83
Figure 63 Tunability of the reflective 2π phase PCS mode	84

This page is left blank intentionally

LIST OF TABLES

Table 1 EBL process steps.....	16
Table 2 Comparison of deferent FPI pressure sensor and PhC pressure sensor performance	32
Table 3 Temperature and angle sensitivity of F-P modes and DBR mode.....	39
Table 4 Summary of all bioresorbable optical sensors	44
Table 5 Comparison of meta-atom and PC candidacy for metalens.....	81

CHAPTER 1.

INTRODUCTION

1.1 Motivation

The demand for small size, high performance semiconductor optical components including the light source, optical lens and optical sensors has been grown rapidly in recent years. For the light sources such as lasers and light emitting diodes (LEDs), the characteristics in need are higher power, higher speed, mode control and lower power consumption. The applications include telecommunication, consumer electronics, autonomous driving. For the optical lenses, the properties of miniaturization towards flat optics and configurability are particularly popular. The applications are for compact wearable electronics such are smart glasses and virtual reality headsets. For the optical sensors, the compatibility to bio implantation is drawing more and more attention, the applications include biomedical diagnosis and all-optical sensing/ imaging for implanted sensing.

We are thus motivated to work on each of these components for an integrated high performance optical platform on a chip. When each device is improved individually, it is then possible to bring them together into one system as shown in Figure 1. In this system, the compact low energy cost laser delivers light through flat optical lenses, to the interested zone where the optical sensors can detect the changes in the environment.

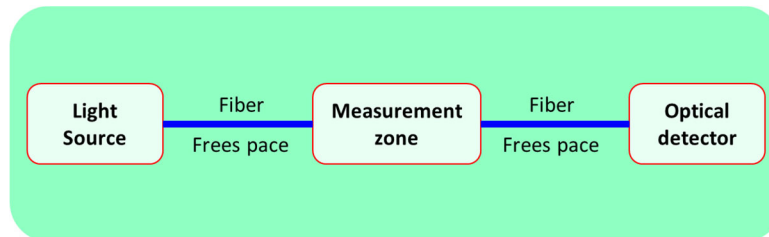


Figure 1 A simple sketch of integrated optical system on chip.

1.2 State of the art

For compact high performance lasers, photonic crystal (PC) devices are particularly drawing more attention for small footprint, highly efficient confinement lasers as it could provide tight spatial confinement [1]. Another promising approach is the Lambda-Scale Embedded Active-Region Photonic Crystal (LEAP) lasers. Currently the energy cost of directly modulated lasers is reduced to 8 fJ/bit [1]. We will investigate PC nanobeam cavity for high speed, low energy cost laser applications in Chapter 3, as well as integration of single-sheet materials for extremely low threshold devices in Chapter 4.

For flat optics, meta-atom based metalens is drawing a great amount of attention for its reconfigurability. Focusing efficiency above 70% has been achieved on multi-color focusing [2] metalens in the visible range. Other novel metalenses such as multi-objective metalens [3] are also well studied. We will investigate the performance of PC based metalens and compare it to the meta-atom based metalens in Chapter 5.

In the field compact optical sensors, the demand is growing for sensors that can be constructed to dissolve harmlessly in biofluids at well-defined, programmable rates to biologically benign end products. Recent demonstrations include biophysical sensors of pressure, temperature, flow rate, and motion [4-6]. We will investigate the bioresorbable optical sensors for brain implantation with advantages over the conventional electrical sensor in Chapter 2.

1.3 Introduction to photonic crystal

The concept of “crystal” or “crystal lattice” in photonics is analogy to the same term in solid state electronics, where it refers to the periodically arrangement of atoms or molecules in space [7]. The significance of crystal lattice in solid state physics is that it presents periodic potentials for electrons propagating through the material and thus the formation of electron energy band in the momentum space. It is the building block of modern electronics and solid state electronic devices that deeply transformed our life today.

The terminology of photonic crystal is then borrowed by photonics to describe the material properties of permittivity for electromagnetic wave propagating through the material. Consequently, there are equivalent phenomena of energy band gaps where the propagation of certain frequency of photons are prohibited in photonic crystal. Shown in Figure 2 is a simple cartoon illustration (by 3Ds Max tool) of one-, two- and three-dimensional photonic crystal (PhC, or PC) structure where different materials (in different colors) are periodically arranged in space.

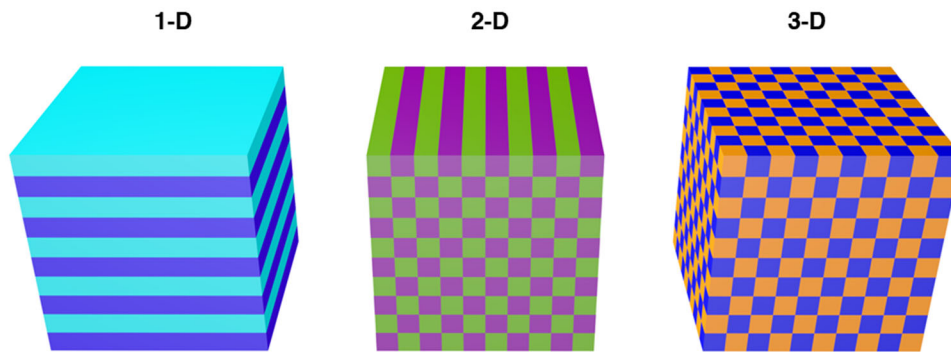


Figure 2 Periodically arranged materials in one-, two- and three-dimensions.

Following the fundamental theory in the “photonic crystal bible” [8], we remind ourselves to keep in mind the basic laws that rule the electromagnetic wave propagating in dielectric medium which is what we deal with most of the time in photonics.

The very first law is the macroscopic Maxwell equations:

$$\begin{aligned}\nabla \cdot \mathbf{B} &= 0, \quad \nabla \times \mathbf{E} + \frac{\partial \mathbf{B}}{\partial t} = 0 \\ \nabla \cdot \mathbf{D} &= \rho, \quad \nabla \times \mathbf{H} + \frac{\partial \mathbf{D}}{\partial t} = \mathbf{J}\end{aligned}\tag{1}$$

In a space with no charge or current source, $\rho = 0$, $\mathbf{J} = 0$. We make the following approximation for dielectric materials:

- (1). Assume that the field strength is small enough so that the permittivity is in linear regime, or the relationship between Displacement field and electric field is $D_i/\epsilon_0 = \sum_j \epsilon_{ij} E_{ij}$.
- (2). Assume that the material is macroscopic and isotropic.
- (3). In most cases, ignore the material dispersion in the frequency range where the permittivity can be approximated to a constant.
- (4). Focus on the transparent materials, consider $\epsilon(\mathbf{r})$ as real and positive.

These assumptions effectively give the following relations:

$$\begin{aligned}\mathbf{B}(\mathbf{r}) &= \mu_0 \mu(\mathbf{r}) \mathbf{H}(\mathbf{r}) \\ \mathbf{D}(\mathbf{r}) &= \epsilon_0 \epsilon(\mathbf{r}) \mathbf{E}(\mathbf{r})\end{aligned}\tag{2}$$

where $\mu_0 = 4\pi \times 10^{-7} \frac{\text{Henry}}{\text{m}}$, $\epsilon_0 \approx 8.85 \times 10^{-12} \frac{\text{Farad}}{\text{m}}$ are the permeability and permittivity of the vacuum.

Substituting the relations into Equation (1), it then becomes:

$$\begin{aligned}\nabla \cdot \mathbf{H}(\mathbf{r}, t) = 0 \quad , \quad \nabla \times \mathbf{E}(\mathbf{r}, t) + \mu_0 \frac{\partial \mathbf{H}(\mathbf{r}, t)}{\partial t} = 0 \\ \nabla \cdot [\varepsilon(\mathbf{r})\mathbf{E}(\mathbf{r}, t)] = 0 \quad , \quad \nabla \times \mathbf{H}(\mathbf{r}, t) + \varepsilon_0 \varepsilon(\mathbf{r}) \frac{\partial \mathbf{E}(\mathbf{r}, t)}{\partial t} = \mathbf{0}\end{aligned}\tag{3}$$

For the time harmonic expansion of fields:

$$\mathbf{H}(\mathbf{r}, t) = \mathbf{H}(\mathbf{r})e^{-i\omega t} \quad , \quad \mathbf{E}(\mathbf{r}, t) = \mathbf{E}(\mathbf{r})e^{-i\omega t}\tag{4}$$

The Maxwell equations become:

$$\nabla \cdot \mathbf{H}(\mathbf{r}) = 0 \quad , \quad \nabla \cdot [\varepsilon(\mathbf{r})\mathbf{E}(\mathbf{r})] = 0\tag{5}$$

And,

$$\begin{aligned}\nabla \times \mathbf{E}(\mathbf{r}) - i \omega \mu_0 \mathbf{H}(\mathbf{r}) = 0 \\ \nabla \times \mathbf{H}(\mathbf{r}, t) + i \omega \varepsilon_0 \varepsilon(\mathbf{r})\mathbf{E}(\mathbf{r}) = \mathbf{0}\end{aligned}\tag{6}$$

This is a coupled equation set and could be simplified using the definition of the vacuum speed of light $c = 1/\sqrt{\varepsilon_0\mu_0}$,

$$\nabla \times \left(\frac{\mathbf{1}}{\varepsilon(\mathbf{r})} \nabla \times \mathbf{H}(\mathbf{r}) \right) = \left(\frac{\omega}{c} \right)^2 \mathbf{H}(\mathbf{r})\tag{7}$$

Equation (7) is the so-called master equation of eigen problems in dielectric materials. Equation (5) means that the propagating electromagnetic waves are transverse (field perpendicular to the wave vector).

Notice that the derivation based on the assumptions above are still valid when isotropic condition and the non-dispersion condition are extended to anisotropic and dispersive materials, with extra terms brought in by the extension.

1.4 Photonic band gap and mode distribution

Following the fundamental theoretical analysis in [8], this section will explore the formation of photonic band gap and how photonic crystal modes distribute inside the media.

1.4.1. Photonic bands

The eigenstate in Brillouin zone of the periodic structure with Bloch wave vector \mathbf{k} takes the form

$$\mathbf{H}_k(\mathbf{r}) = e^{i\mathbf{k}\cdot\mathbf{r}}\mathbf{u}_k(\mathbf{r}) \quad (8)$$

Substituting this state into the master equation leads to:

$$\hat{\Theta}_k\mathbf{u}_k(\mathbf{r}) = \left(\frac{\omega(\mathbf{k})}{c}\right)^2 \mathbf{u}_k(\mathbf{r}) \quad (9)$$

Where the new Hermitian operator is defined as,

$$\hat{\Theta}_k = (i\mathbf{k} + \nabla) \times \frac{\mathbf{1}}{\varepsilon(\mathbf{r})} (i\mathbf{k} + \nabla) \times \quad (10)$$

Now the new function \mathbf{u} is the mode profile that satisfies the periodic boundary condition. So, for each value of \mathbf{k} there exist an infinite set of modes with discretely spaced frequencies that can be labeled by an integer index n . These solutions form the **photonic bands** in the energy-momentum space (E- k space, or frequency-wave number ω - k space). The formation of photonic bands is analogous to the energy quantization in Quantum mechanics where wave function is subjected to periodic boundary condition (one simple but less accurate example is the 1D quantum well problem leading to the discretization of electron energy levels).

1.4.2. Two-dimensional (2D) photonic crystal

As a result of periodic modulation of medium permittivity, **photonic band gap** (PBG) is formed in the band diagram. This could be explained by the variational theorem, which found that the lower frequency modes concentrate larger portion of its energy in higher ϵ medium (and thus referred as dielectric band) and higher frequency modes have larger portion of its energy in low- ϵ medium (referred as air band). In the photonic band gap, no mode is allowed at any k value. The field distribution of different mode is quantified by the concentration factor as,

$$\text{concentration factor} \triangleq \frac{\int_{\text{high-}\epsilon} dv \cdot \epsilon(\mathbf{r}) \cdot |\mathbf{E}(\mathbf{r})|^2}{\int_{\text{total}} dv \cdot \epsilon(\mathbf{r}) \cdot |\mathbf{E}(\mathbf{r})|^2} \quad (11)$$

The concentration factor is a measure of the fraction of electric-field energy located inside the high- ϵ medium of the total energy. In the photonic band, the boundary line $\omega(k) = ck/\sqrt{\epsilon}$ is referred as the light line.

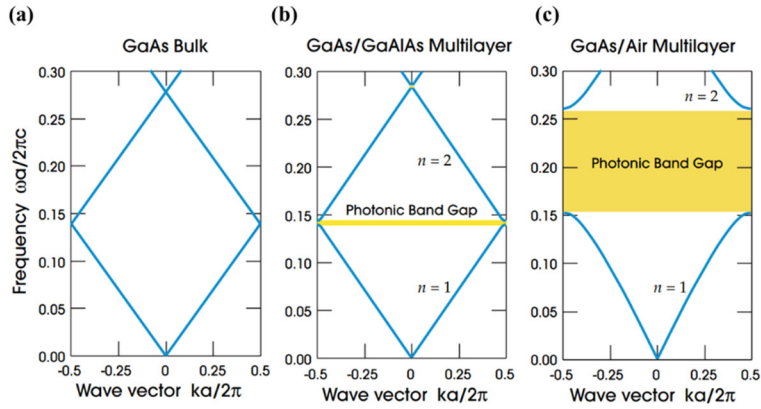


Figure 3 Photonic band diagram of 1-dimensional multilayer PhC.

(a) Every layer has the same dielectric constant ϵ -13, (b) layers alternate between ϵ of 13 and 12, (c) layers alternate between ϵ of 13 and 1. (image reused from Ref. [8])

A simple interpretation of photonic band gap is given in the “PhC Bible” [8] for 1D PhC. As shown in Figure 3, ω - k relationship is plotted for 3 different multilayer films. The size of the PBG reflects the contrast in dielectric constants $\Delta\epsilon$ of the perturbation, it increases with the $\Delta\epsilon$.

The applications of photonic band gap in two-dimensional photonic crystal are vast and promising. It could form high confinement narrow bandwidth filters [9], or high reflectance broadband reflectors [10,11].

Shown in Figure 4 is the photonic band diagram of a 2D PhC Fano filter [12], the PhC is fabricated on a silicon-on-insulator (SOI) wafer with square lattice constant a , airhole radius $0.19a$ and slab thickness $0.417a$.

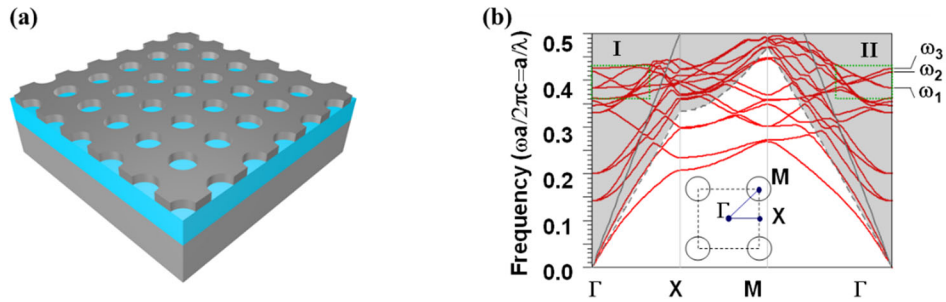


Figure 4 Photonic band diagram of a 2D PhC on SOI substrate.

(a) 3D schematic illustration and (b) photonic band diagram (from Ref. [12])

1.5 Different photonic crystal design with applications

In this dissertation, we will cover several types of 2D PhC for different application purposes: Fano resonance optical filter PhC, heterostructure PhC, 1D nanobeam PhC, and 2D metalens PhC.

1.5.1. Fano resonance PhC optical filters

In photonic crystal slabs (PCS), in addition to the guided modes that are completely confined by the slab without coupling to external radiations, there are also interactions between in-plane modes and out-of-plane radiation. One particularly interesting phenomenon observed is guided resonance, which has the electromagnetic power strongly confined within the slab, while also has modes that can couple to the external radiation [13]. In general, the line shape of the transmission or reflection of these modes are asymmetric and can be characterized by Fano resonance.

We will adopt the Fano resonance PhC for optical filter or sensor applications. Shown in Figure 5 are (a) scanning electron microscope (SEM) image and (b) Measured and simulated spectra of a 2D PhC on SOI substrate with lattice constant $a=0.97\mu\text{m}$ and airhole radius $r=65\text{ nm}$. The Fano resonance wavelength is subjective to the refractive index and lattice dimension change which will be implemented as the principle of optical sensing applications.

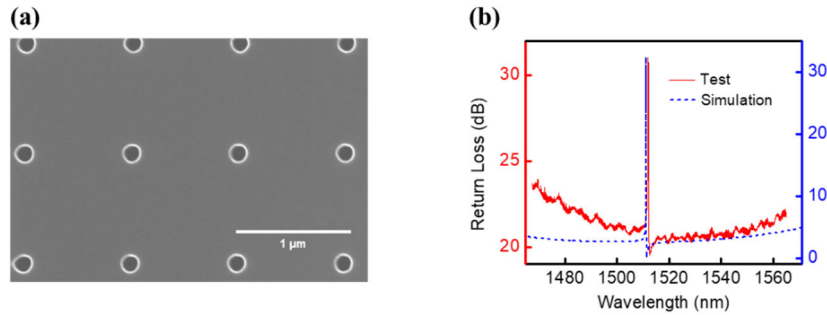


Figure 5 SEM and reflection spectrum of a 2D PhC on SOI substrate.

(a) Scanning electron microscope (SEM) image and (b) Measured and simulated spectra.

1.5.2. Lateral confinement enhancement with heterostructure PhC

Enabled by the slow light phenomenon at the band edge of photonic crystals. Photonic crystal heterostructure cavities have been widely used for achieving lateral confinement within two-

dimensional photonic crystal slabs. Heterostructure cavities can be formed by either modulating the filling factors [14-17] or embedding different types of lattices [18].

For heterostructure PC design, we show that without a complete photonic band gap, it is still possible to achieve efficient lateral confinement and high Q within a hexagonal lattice by a heterostructure formed by tuning the hole radii. The fact that the starting modes are above the light cone means that the requirement of refractive index contrast can be relaxed as there is no need for opening a complete photonic band gap, which is beneficial for visible wavelengths where high refractive index material is limited.

Shown in Figure 6 is a 2D heterostructure PhC on Si_3N_4 film on quartz substrate. The PhC is formed by a hexagonal lattice of air holes with period $a = 460$ nm, while the thickness of the silicon nitride slab is $h = 160$ nm. The heterostructure cavity is composed of three regions, denoted as the core region, the transitional region and the cladding region from the center to the edge of the PhC lattice with decreasing hole radii ($R_{\text{core}} = 0.24a$, $R_{\text{trans}} = 0.22a$ and $R_{\text{clad}} = 0.20a$).

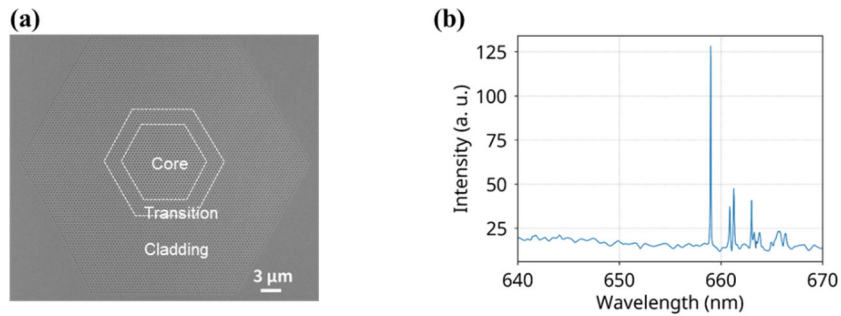


Figure 6 SEM and reflection spectrum of a 2D PhC on Si_3N_4 substrate.

(a) Scanning electron microscope (SEM) image and (b) Measured spectrum.

1.5.3. 1D defect mode PhC nanobeam cavity

Point defect in periodic dielectric waveguides can create incomplete band gap where the modes above the light cone can couple to the defect mode and becomes leaky mode or resonance. In the current micro laser technology, bandgap defect states in nanobeam structures have higher Q ($\sim 10^6$) while maintaining a low mode volume ($\sim 0.09 \mu\text{m}^3$) [19]. Equipped with the lateral current injection scheme, reference [20,21] demonstrate nanobeam cavities with mode volume of $0.02 \mu\text{m}^3$.

The schematic of the design of our one-dimensional PhC nanobeam cavity (PCNB) on suspended Si_3N_4 thin waveguide is shown in Figure 7. The air holes with uniform spacing are designed outside taper region to serve as Bragg mirrors and provide mode confinement [20,22], a gradually increasing air hole radius in the taper region introduces the adiabatic change of effective refractive index to reduce the mode scattering and enhance mode confinement more effectively.

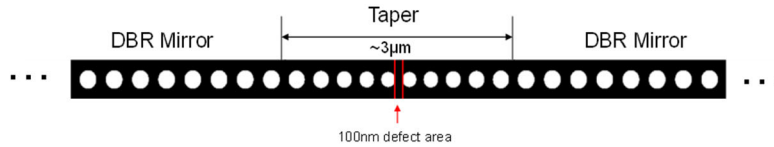


Figure 7 Schematic of a Nanobeam Cavity Design.

The nanobeam cavity is formed by a defect region surrounded by tapered air holes and confined by the DBR mirrors. A 100nm defect area can support a fundamental mode at the wavelength of 620nm.

1.6 Numerical utilities

1.6.1. Rigorous coupled wave analysis method with S4

Stanford Stratified Structure Solver (S4 or S⁴) [23], is a frequency domain code to solve the linear Maxwell's equations in layered periodic structures. Internally, it uses Rigorous Coupled Wave Analysis (RCWA; also called the Fourier Modal Method (FMM)) and the S-matrix algorithm. The program is implemented using a Lua frontend, or alternatively, as a Python extension. S⁴ was

developed by Victor Liu of the Fan Group in the Stanford Electrical Engineering Department in 2012.

S4 is particularly popular for solving the reflection and transmission problems of in-plane periodic layered structure. It constructs the pseudo 3D structures by defining all the layer properties (dielectric constant, thickness, pattern in the layer) within a unit cell. A few conventions need to be noted as shown by the illustration cartoon in Figure 8:

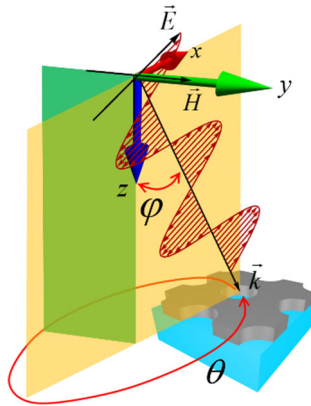


Figure 8 Cartoon illustration of the S4 layered structure and coordinates convention. The yellow plane is the x-z plane, the green plane is the y-z plane.

- (1). There are 2 Cartesian coordinates: x - y - z , and \mathbf{E} - \mathbf{H} - \mathbf{k} .
- (2). Angle φ is defined as angle of \mathbf{E} - \mathbf{H} - \mathbf{k} rotates about y axis, $(0, 180)^\circ$.
- (3). Angle θ is defined as angle of \mathbf{E} - \mathbf{H} - \mathbf{k} rotates about z axis, $(0, 360)^\circ$.
- (4). At angle $\varphi = 0^\circ$, $\theta = 0^\circ$, an s -polarized input light has only y component. “ s ” stands for senkrecht or perpendicular, which means the incident plane is x - z plane.

1.6.2. Finite-difference time-domain (FDTD) method

Finite-difference time-domain (FDTD) or Yee's method [24] is a numerical analysis technique used for modeling computational electrodynamics. There are several well-known FDTD tools that can run on across platforms.

MIT Electromagnetic Equation Propagation (MEEP) [25] is an open source software package for electromagnetics (EM) simulation via the FDTD method spanning a broad range of applications. It has the interface with Python or Scheme languages for programming the structure of EM problems and running the simulation. The components that can be defined are sources, geometries, monitors, run-time, resolution, and boundary conditions and more.

While being a powerful tool with the freedom of programming the input and output, MEEP often take huge computational resources for large number of grids, especially when the geometry input is 3-dimensional. So, it often is installed and run on servers instead of individual computers.

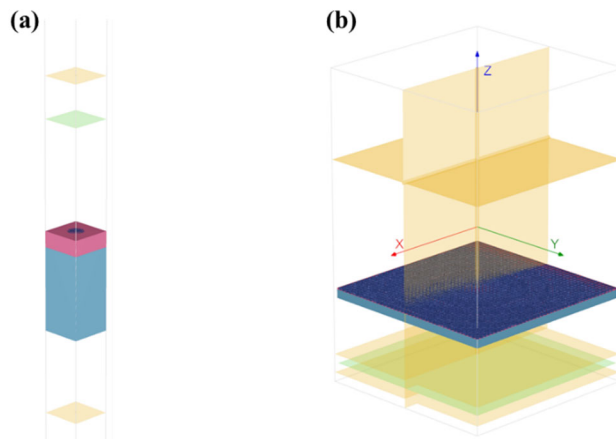


Figure 9 3D sketch models built in Tidy3D.

(a) A PhC unit cell model and (b) a metalens model. The yellow planes are the field monitors, the green plane is the light source.

There is a newly built FDTD tool Tidy3D [26] that has the potential to solve the computing power issue and save running time tremendously. Tidy3D is a finite-difference time-domain solver

providing speed and scale for extremely large problems. The Python API can be used to build simulation models, submit jobs, and analyze results of complete runs. Similar to settings in MEEP, it also defines the components locally and submits the task to the server that is maintained by the developers' team. As shown in Figure 9, the simulation is run on cloud based servers and the result can be downloaded along with the 3D model. Tidy3D could finish simulation in a few seconds for task that could take hours on other tools.

1.6.3. Calculation of photonic bands

Calculation of PBG structure is often done in MEEP with its module MIT photonic band (MPB), or in commercial software such as COMSOL Multiphysics. One simple yet power tool under open source license is Legume [27], which adopts the plane wave expansion (PWE) and guided mode expansion (GME) methods to find the modes in stacked layers with patterns and periodic boundary conditions in the lateral dimension.

Figure 10 shows the calculated PBG structure of a 2D PhC slab on quartz in Legume.

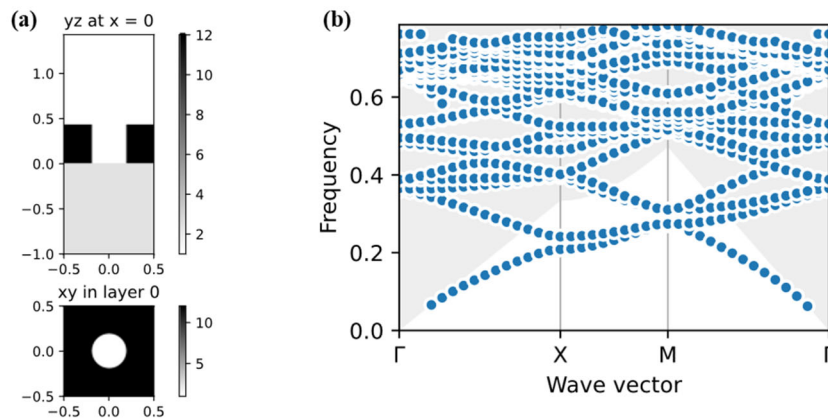


Figure 10 Photonic band structure calculated in Legume.

(a) Dielectric profiles in y - z plane and x - y plane, and (b) calculated band structure.

1.7 Fabrication of photonic crystal

In visible to infrared spectrum, most of the PhC structures, pillar-like to airhole-like, have subwavelength unit cell dimensions, with the perturbation geometry under 500 nm. Feature size of PhC is then too small for most photolithography process. Patterning PhC on slab or with deposition consists of electron beam (e-Beam) lithography and PhC layer etching/deposition.

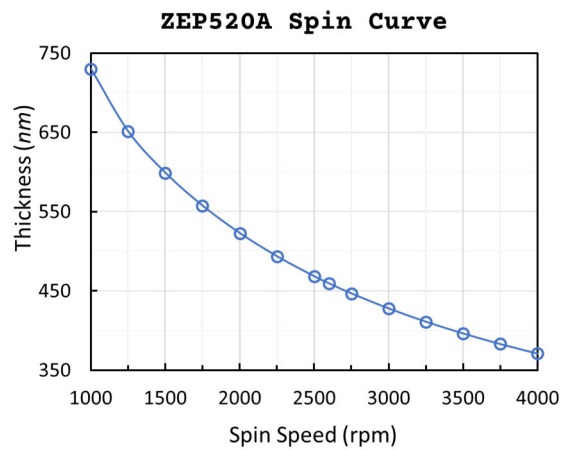


Figure 11 Spin curve of ZEP520A

1.7.1. Electron beam lithography

Electron-beam lithography (often abbreviated as e-beam lithography, EBL) is the practice of scanning a focused beam of electrons to draw custom shapes on a surface covered with an electron-sensitive film called a e-Beam resist (exposing).

The e-Beam resist we use is a positive e-beam resist ZEP 520A (Zeon Corporation). The spin curve of the resist is shown in Figure 11. The EBL process flow is shown in Table 1.

The first step is to design and load the pattern files to the EBL exposing tool. We use the open source Python packages gdspsy and gdsCAD for designing of PhC patterns. These packages offer powerful and flexible control of the patterns by defining the coordinates of each point (in GDS format, there are only two types of entities: path whose end points does not connect, and boundary whose end points are connected).

We run EBL exposure on a Nability nano pattern generation system (NPGS) that is an add-on to a Zeiss SEM.

Table 1 EBL process steps

Step	Process	Substrate					
		Insulating			Conducting		
1	Dehydration Dry		/			/	
2	ZEP 520A Spin Coating	2000rpm, 1000rpm/s	60s	460nm	2000rpm, 1000rpm/s	60s	460nm
4	Pre Bake (Soft Bake)	180 °C	3min		180 °C	60s	
3	Eletra 92 Spin Coating	2000rpm, 1000rpm/s	60s	523nm		/	
4	Pre Bake (Soft Bake)	90 °C	2min			/	
5	Exposure						
6	Post Bake		/			/	
7	Eletra 92 Removal	DI Water	2min			/	
8	Developing	n-Amyl Acetate	1min		n-Amyl Acetate	1min	
9	Rinse	IPA	30s		IPA	1min	
10	Rinse	DI Water	20 ~ 30s				
11	Etching						
12	ZEP 520A Removal	NMP 70°C Ultrasonication	>2min				

It is critical to calibrate the exposure process for each type of pattern. Generally, thicker resist requires higher dose to clear out the resist, smaller exposure area requires higher dose to clear. Most of the time, we desire straight sidewall profile on the resist as shown in Figure 12, though it is also possible to achieve slanted sidewall profile by overdosing the pattern area.

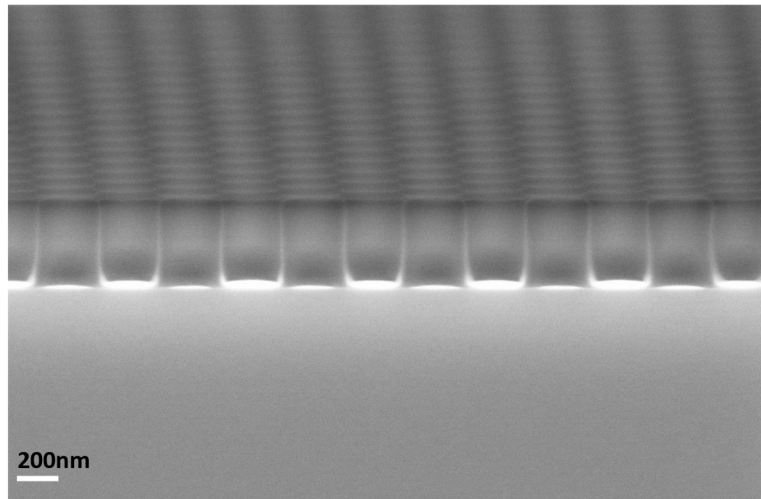


Figure 12 SEM of properly exposed ZEP520A resist on GaAs substrate

1.7.2. Reactive ion etching

Reactive-ion etching (RIE) is a dry etching technology which uses chemically reactive plasma to remove material deposited on wafers. The plasma is generated under low pressure (vacuum) by an electromagnetic field. High-energy ions from the plasma attack the wafer surface and react with it. It often works together with inductively couple power (ICP) plasmas.

The ions in RIE process etches the target material in two ways: physical bombardment by high kinetic energy ions that does not react with the target ions, and chemical reaction of the etchant ion with the target ions on the surface. The etching parameters of a RIE recipe contains the gas

constituents, gas flow rate, pressure of the reaction chamber, RIE power, ICP power and run time. One key point for tuning a good PhC RIE recipe is to keep the chamber pressure at minimum with small gas flow rate to achieve a slow but smooth etching profile. Another general rule to keep in mind is that for different sizes of opening, parameters also need to be tuned for the best etching result. Appendix B discusses in detail the PhC etching recipes for Si, Si₃N₄, GaAs that we tuned out in NanoFab at UTA.

For Si PhC etching, the gases used are SF₆ for etching, CHF₃ for passivation, O₂ and Ar for physical etching. Shown in Figure 13 is an SEM of PhC etched by RIE on Si. The RIE tool is a TRION DRIE Si etcher. The selectivity of this recipe is around 1:1. It consumes the resist as much as it etches the substrate due to the lack of low-pressure capability of the tool.

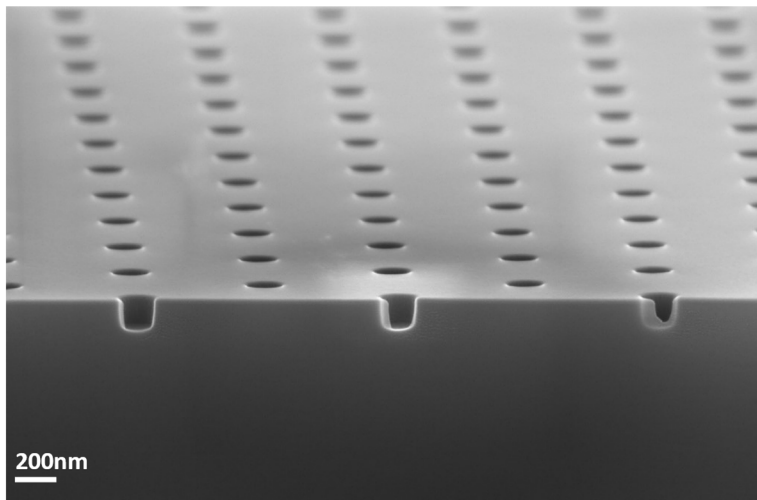


Figure 13 SEM of PhC on Si

Si₃N₄ PhC etching recipe is very similar to that of Si, using SF₆ for etching, CHF₃ for passivation, and adding some He for dilution of the etchant ions. On the same tool (TRION DRIE etcher), we developed the RIE recipe for low pressure chemical vapor deposition (LPCVD) Si₃N₄

material. Shown in Figure 14 is an SEM of Si_3N_4 PhC on Si substrate. The selectivity of this recipe is 1:1.2 for EBL resist.

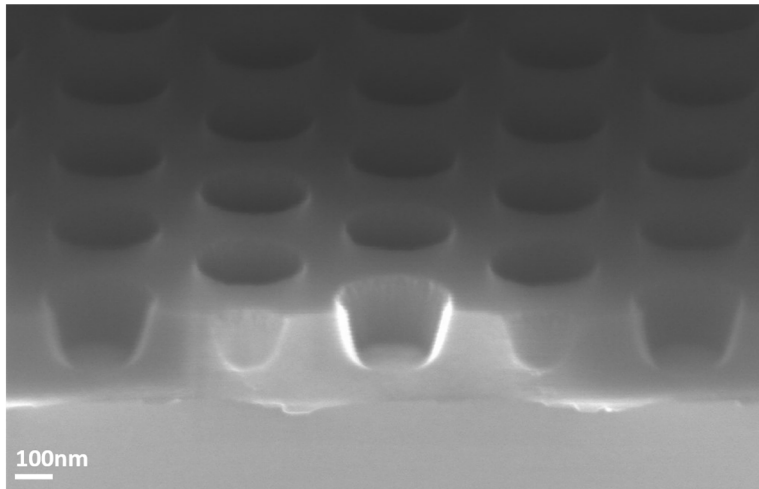


Figure 14 SEM of Si_3N_4 PhC slab on Si

The GaAs PhC RIE recipe we developed on a TRION MiniLock uses SiCl_4 as the etching gas solely or with Ar gas for dilution. This recipe is capable of etching ultra-small openings with etching rate 45 nm/min for airhole radius of 63 nm. The SEM image shown in Figure 15 is a PhC etched on.

Another more common option for GaAs PhC etching is to use Cl_2 and BrCl_3 as the etching gases. This recipe is developed at the Cleanroom research laboratory at UT Dallas. Show in is the SEM of GaA PhC, the top portion of the structure is the left-over of the e-Beam resist. There is a thin layer of coated by-product in the opening which does not affect the etching process and could be completely cleaned out in the following resist-stripping process and HF (1:10) dipping step.

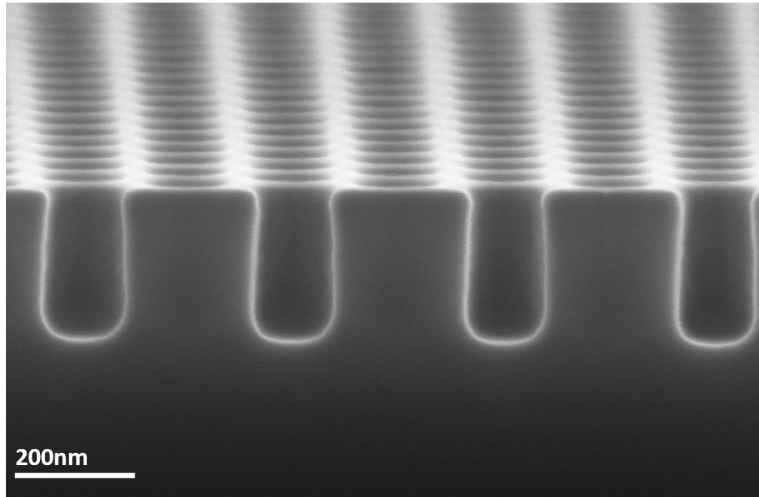


Figure 15 SEM of GaAs PhC

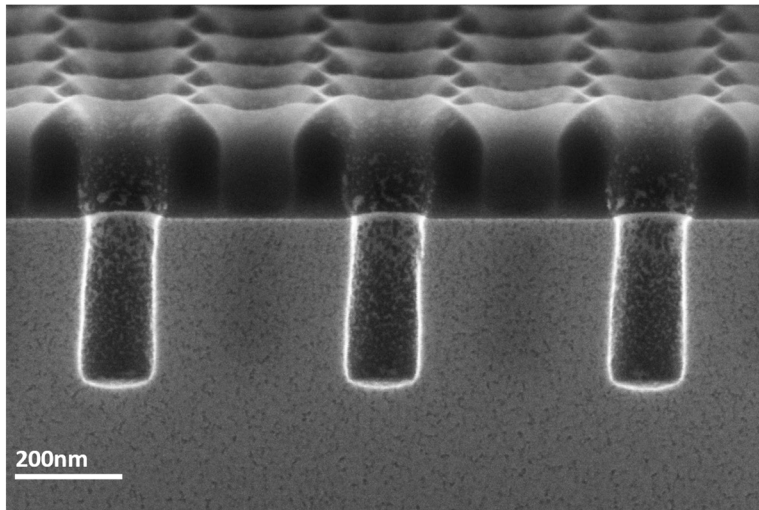


Figure 16 SEM of GaAs PhC

1.8 Content overview of the dissertation

The content of this dissertation is focused on the topic of photonic crystal laser and sensor devices. The organization of the contents are as follows:

In Chapter 1, we cover in detail the electromagnetic principle, the state of the art in the field of integrated optical system on chip, the optical design, the numerical calculation methods, and the fabrication process of different PhC structures. From Chapter 2 to Chapter 5, we discuss about the PhC devices for laser and sensor applications. Chapter 2 discusses the photonic crystal and Fabry-Perot membrane optical sensors for biomedical applications. Chapter 3 discusses the heterostructure PhC cavity for integrated laser with 2D materials. Chapter 4 investigates the PhC nanobeam structure with defect mode for external emission. Chapter 5 discusses the design of PhC phase plate and applications in metalens. And finally in Chapter 6, we summarize the work done and look into the future development proposals of the works. The appendices afterwards will cover the details of EBL dose tuning process and RIE recipe developments.

A list of publications in the PhD program is included at the end, followed by the complete reference list for this work.

CHAPTER 2.

BIORESORBABLE IMPLANTABLE OPTICAL SENSORS

2.1 Introduction

Implantable sensors capable of precise, continuous monitoring of pressure and temperature within organ spaces associated with the brain, heart, eyes, and bladder provide essential diagnostic information for defining treatment protocols for diseases such as traumatic brain injury, cardiovascular abnormalities, glaucoma, and neurogenic bladder dysfunction, respectively [28-30]. Among various conventional sensor technologies, optical devices are finding increasing utility in these and other contexts due to their immunity to electromagnetic fields, thereby offering improved compatibility with clinical imaging techniques such as magnetic resonance imaging (MRI) [31-33]. More specifically, the absence of conductive traces and electrically powered circuit components greatly reduces adverse events that can arise from Joule heating [34,35], dislocation [36], and image distortion [37] induced by electromagnetic interactions during the MRI, or current leakage that could follow from defects in the device encapsulation [38]. The permanent nature of the constituent materials represents a disadvantage for all existing sensors, both electrical and optical, because of their need for surgical removal after a useful operating period. These procedures are costly and can lead to additional complications and risks to the patient [39]. Such permanent devices can also serve as a nidus for infection [40,41] and they can lead to immune-mediated inflammatory responses.

Solutions to these challenges may follow from the use of materials, device designs, and fabrication strategies in emerging classes of bioresorbable electronic sensor systems. Such types of devices can be constructed to dissolve harmlessly in biofluids at well-defined, programmable rates with biologically benign end-products. Here, processes of bioresorption naturally eliminate the devices at their sites of implantation after relevant operational time frames, thereby bypassing the need for surgical extraction. Recent demonstrations include biophysical sensors of pressure,

temperature, flow rate, and motion [42-44], several types of biochemical sensors [42,45], neural electrodes [46], and power supplies [47]. Published in vivo studies include deployments in the intracranial and intra-abdominal spaces and in the leg cavities [42,44], on cortical surfaces [46,48], and in subdermal regions [49]. Substituting basic components of these systems, such as the sensing element (silicon nanomembranes), device architectures (micro-electro-mechanical or thin-film designs), and electrical interconnections (bioresorbable metal electrodes), with optical analogues offers the potential to establish routes to diverse types of bioresorbable optical sensors. Device designs adapted from conventional, non-resorbable optical sensor technologies, such as Fabry-Pérot interferometer (FPI) sensors, with sensitivities, accuracies, and measurement ranges that meet various clinical needs, are of particular interest.

A major challenge in the development of bioresorbable sensors as implantable monitors with clinical-grade performance is in realizing consistent mechanical and electrical/optical behavior while immersed in biofluids throughout the clinically relevant monitoring periods, prior to undergoing complete bioresorption. Most bioresorbable pressure and temperature sensors operate stably in simulated biofluids for only a few days, which is insufficient for many envisioned applications, such as in intracranial monitoring during a recovery period following traumatic brain injury [42,43]. In other cases, the stability remains to be studied thoroughly [50-52]. The limitations arise mainly from the inability of bioresorbable encapsulation layers, including polymers such as silk fibroin [49] and poly(lactic-co-glycolic acid) (PLGA) [47] and inorganic layers such as silicon dioxide [53,54] and various metal oxides [55] formed by chemical or physical vapor deposition, to prevent permeation of water into the active regions of the devices for extended periods of time. Recent work demonstrates that ultrathin layers of silicon dioxide thermally grown on device-grade silicon wafers (t-SiO₂) can be used as bioresorbable encapsulation layers, to enable stable operation of intracranial pressure and temperature sensors over a period of 25 days in rats [44].

Here, we demonstrate two types of bioresorbable optical pressure sensors that build on and exploit some of these ideas. One uses a Fabry-Pérot interferometer (FPI) design and the other exploits photonic crystal (PC) structures. Both systems rely on pressure-induced deflections of silicon nanomembrane (Si NM) diaphragms, and the resulting changes in the thickness of an air cavity or in the lattice parameters of a PC, both of which cause shifts in resonant peak positions in the reflection spectra. These platforms can also be configured to sense temperature in a manner that relies on the temperature-dependent refractive index of silicon. Fabrication procedures based on wafer bonding of SOI wafers followed by back-etching of the handle wafers enable device structures encapsulated in thin layers of t-SiO₂, with stable operating times of over a week. Both PLGA optical fibers and free-space detection set-ups serve as bioresorbable optical interfaces. In vitro dissolution studies and histopathological evaluations confirm the biodegradability of these complete systems. Acute measurements of intracranial pressure and temperature in rats suggest some potential for clinical application. The results not only establish routes to pressure and temperature sensor technologies that are completely bioresorbable and MRI compatible, but they also represent generalizable platforms for other classes of bioresorbable optical sensors. Here, we demonstrate two types of bioresorbable optical pressure sensors that build on and exploit some of these ideas. One uses a Fabry-Pérot interferometer (FPI) design and the other exploits photonic crystal (PC) structures. Both systems rely on pressure-induced deflections of silicon nanomembrane (Si NM) diaphragms, and the resulting changes in the thickness of an air cavity or in the lattice parameters of a PC, both of which cause shifts in resonant peak positions in the reflection spectra. These platforms can also be configured to sense temperature in a manner that relies on the temperature-dependent refractive index of silicon. Fabrication procedures based on wafer bonding of SOI wafers followed by back-etching of the handle wafers enable device structures encapsulated in thin layers of t-SiO₂, with stable operating times of over a week. Both PLGA optical fibers and free-space detection set-ups serve as bioresorbable optical interfaces. In vitro dissolution studies and

histopathological evaluations confirm the biodegradability of these complete systems. Acute measurements of intracranial pressure and temperature in rats suggest some potential for clinical application. The results not only establish routes to pressure and temperature sensor technologies that are completely bioresorbable and MRI compatible, but they also represent generalizable platforms for other classes of bioresorbable optical sensors.

2.2 FPI pressure sensor on fiber tip

2.2.1. Design and Fabrication

Figure 17(a) shows the material and structure break-down of the device consisting entirely of inorganic materials such as coatings of thermally-grown silicon dioxide (t-SiO₂, ~10 nm), single-crystalline silicon nanomembrane (Si NM; 250 nm), adhesion layers of amorphous silica (~200 nm), and a slab of silicon with a square cavity (dimensions: 750μm × 750μm × 10μm, cavity area: 250μm×250μm) defined by etching a structure of relief onto its surface. Bonding layers of t-SiO₂ and Si NMs onto the top and bottom sides of this slab yields two pressure-sensitive diaphragms that float over a sealed air chamber in between.

Figure 17(b) shows the cartoon of the cross-section view of our pressure sensor. Conventional optical fiber is attached to one of the Si NMs by optical glue. The optical sensing mechanism involves detecting the changes induced to the effective optical path length (OPL). The sealed air cavity by silicon Si NM responds to the ambient pressure change by deforming free-hang Si NM towards optical fiber side. Optical fibers connected to a tunable laser and photodetector couple light in and out of the device to enable measurement of pressure and temperature via changes in measured reflection spectra.

The designing of the FPI devices involves optimizing the sensing range while maintaining the sensitivity, lowering the temperature influence, and sustaining the required lifetime. All these

characteristics are determined by the parameters of membrane thickness, chamber wafer thickness and chamber size.

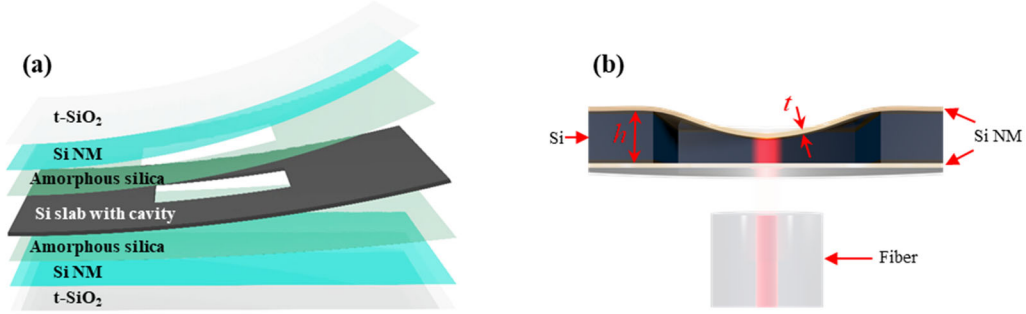


Figure 17 Schematics of FPI pressure sensor

(a) material and components; and (b) illustrative cartoon of the fiber integrated FPI pressure sensor

For very thin devices, our first consideration of design is to have at least one mode within our target wavelength range ($1550 \pm 50 \text{ nm}$). The simplified F-P resonance peak wavelength (resonance mode) expression is

$$\lambda_q = \frac{2nh}{q}$$

where n is refractive index of the medium, h is the thickness of the medium where light propagates normally, and q is the mode number. We define our sensing dynamic range to be the range within which mode catching happens. The separation of 2 modes in wavelength domain $(\Delta\lambda_0)_{f_{SR}}$, and the chamber thickness change $\delta h_{\lambda_q=\lambda_{q-1}}$ at which the mode catching occurs are,

$$(\Delta\lambda_0)_{f_{SR}} \approx \frac{\lambda_0^2}{2nh}, \quad \delta h_{\lambda_q=\lambda_{q-1}} = \frac{h}{q}$$

The fabrication of the FPI pressure sensor on a fiber tip consists of the sensor fabrication process initially developed by UIUC group based on a previously available CMOS compatible procedures, and the fiber alignment and bonding process developed at UTA. The sensor fabrication

process starts with preparing 2 types, 3 pieces of silicon-on-insulator wafer (SOI) wafers, followed by multiple steps of pattern transfer and wafer bonding to construct the stand-alone pressure sensor. The fiber integration utilizes the optical alignment tools and instruments to optimize the fiber tip alignment to the sensor, followed by optical adhesive bonding the fiber to one side of the Si NM.

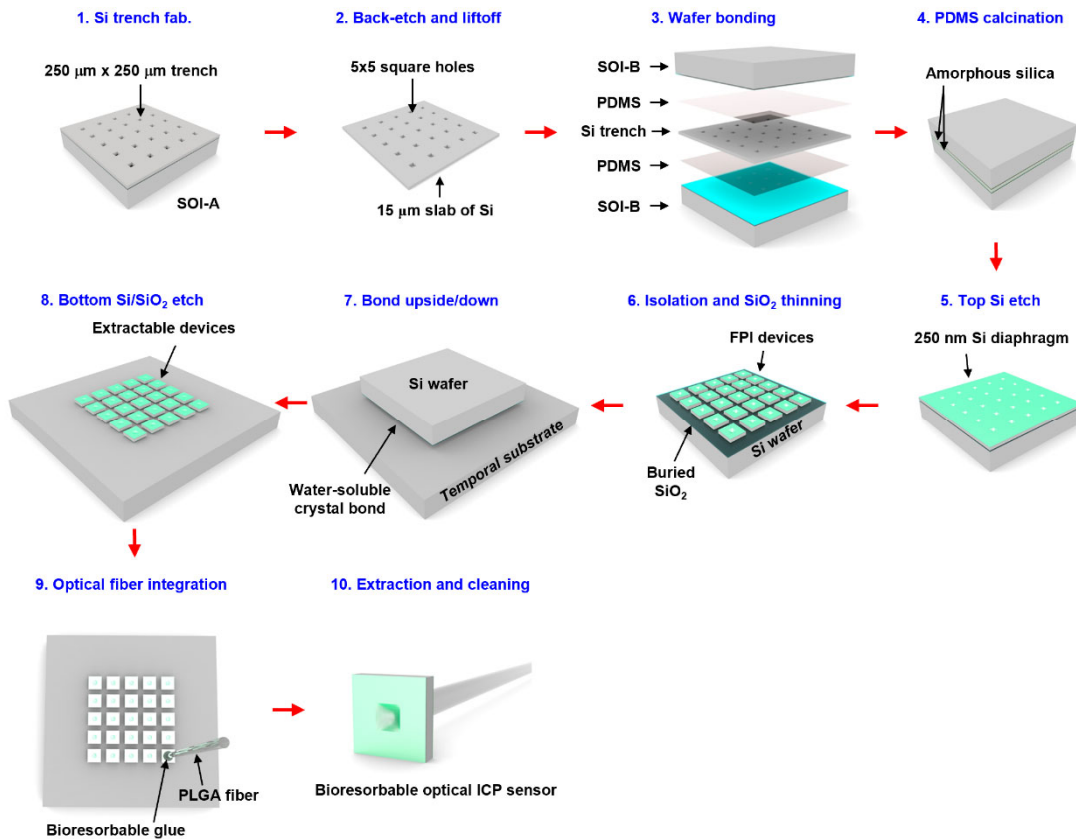


Figure 18 Sketch illustration of the FPI pressure sensor fabrication flow

Figure 18 shows the process illustration of fabricating the FPI pressure sensor. Mechanical back-grinding (Syagrus Systems, USA) reduces the thickness of the silicon handle wafer of a silicon-on-insulator wafer (SOI-A, top Si ~10μm, buried SiO₂ ~600 nm, Si wafer ~90μm; University Wafers, USA) prior to device fabrication. Photolithography and deep reactive ion etching

(STS Pegasus ICP-DRIE) forms a 5×5 array of square trenches ($250\mu\text{m} \times 250\mu\text{m} \times 10\mu\text{m}$) on the top Si layer. ICP-DRIE and wet etching in hydrofluoric acid (HF, Transene Company Inc., USA) removes the Si wafer and buried SiO₂ layer to release a $10\mu\text{m}$ -thick slab of Si with trenches on its surface. Then, photolithography and ICP-DRIE defines an array of vent holes (area: $100\mu\text{m} \times 100\mu\text{m}$) through the thickness of SOI-B. The next step of wafer bonding process involves spin-coating a layer of diluted poly(dimethylsiloxane) (PDMS, part A/part B/hexane = 10:1:100 by weight, Sylgard 184; Dow Corning, USA) to a thickness of $3\mu\text{m}$ on two SOI-B wafer samples, partially curing the PDMS at 110°C for 1 minute, transferring the silicon trench on top of one SOI-B, transferring the other SOI-B on top upside-down, pressing the wafers together in a steel vise (Toomaker's vise; Tormach, Inc., USA), and fully curing the PDMS by placing the vise in a 70°C convection oven for 2 hours. Further heating the vise in a furnace, raising the temperature gradually to 550°C over 2 hours and maintaining this temperature for an additional 2 hours converts the PDMS to amorphous silica. Next, the bonded device goes through the similar patterning, dry and wet etching process to remove the extra material. Lastly, bonding the sample upside-down on a temporary Si carrier wafer using water-soluble crystal bond (Structure Probe Inc., USA), followed by ICP-DRIE and wet etching in BOE to thin the buried SiO₂ yields individual bioresorbable FPI sensors.

2.2.2. FPI pressure sensor integration with fiber, calibration, and temperature influence

Figure 19 shows (a) the photograph of one FPI device, (b) the optical spectrum of $10\mu\text{m}$ chamber device during the alignment process, and (c) the optical spectrum comparison of a $10\mu\text{m}$ (T44) and a $100\mu\text{m}$ (T35) chamber device.

For fiber alignment and bonding process, a set of stages and positioners (ULTRAlign Precision Fiber Optic Alignment Stages and Positioners; Newport, USA) launches a pigtail single mode fiber (SMF) close to the FPI sensor bonded to a temporary carrier wafer by the water-soluble

crystal bond (Structure Probe Inc., USA). As shown in Figure 20, the other side of the SMF is connected to port 2 of an optical fiber circulator, where port 1 is connected to the super luminescent diode (SLD, Model S5FC1550P-A2; Thorlabs Inc., USA) and port 3 is connected to the optical spectrum analyzer (OSA) (Model AQ6370B; Yokogawa Test & Measurement Corporation, Japan). Adjusting the fiber launching angle and x-y-z position optimizes the alignment when the largest return intensity is observed on OSA. This alignment is secured by applying a micrometer size optical glue (NOA81, Norland Products Inc., USA) at the site of fiber-sensor proximity without disturbing the alignment and exposing the area with ultraviolet light (SpotCure-B6, Lightning Enterprises LLC, USA) for 60s. Applying heat by blowing hot air to the bonding area liquidizes the crystal bonding and the FPI sensor on fiber tip can then be released as a standalone functional device.

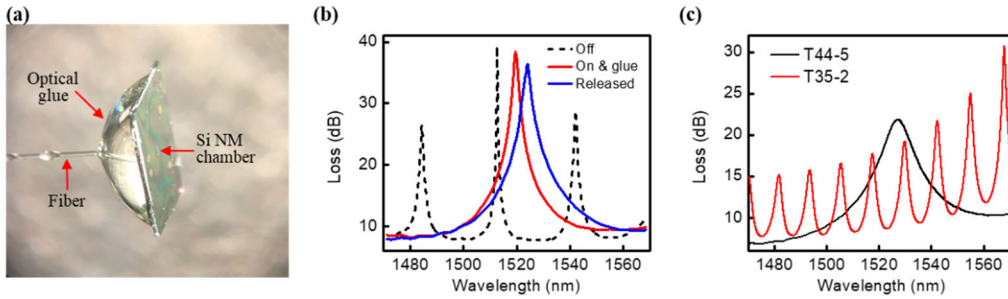


Figure 19 Photograph and spectra of FPI pressure sensor calibration

(a) Photo of one FPI device; (b) the spectrum of return signal during alignment where the fiber tip is aligned to different areas on the device surface; and (c) the optical spectrum of device T35-2 (100 μm chamber) and of device T44-5 (10 μm chamber) measured at room temperature and 102.3kPa (767.313 mmHg).

Figure 20 show the in vitro test set-up used for calibrating the pressure and temperature responses of the bioresorbable FPI sensors. The set-up included an airtight test chamber (built from a plastic container fitted with rubber rings) that contained a beaker filled with phosphate buffered saline (PBS, pH 7.4, 0.01 M; Sigma-Aldrich, USA), in which the FPI sensor and a commercial thermistor (DigiKey, USA) were immersed. A thermoelectric heater/cooler installed underneath the platform enabled temperature control. Specifically, a thermoelectric controller (Model TC-720;

TE Technology Inc. USA), connected with the thermistor and thermoelectric heater/cooler, located outside of the chamber maintained the desired temperature of the PBS via automated proportional-integral-differential (PID) feedback control of the temperature. Plastic tube connections to a plastic syringe through a one-way valve (Plastic Double Head Check Valve; Tasharina Corp., USA), and a commercial pressure sensor (NeuLog, USA) allowed for control and measurement of the pressure inside the chamber, respectively. An integrated tunable laser source-photodetector (8163B Lightwave Multimeter; Keysight Technologies Inc., USA) system connected with a circulator (Model 6015-3-APC; Thorlabs Inc., USA) enabled optical communication with FPI sensors. Collecting optical spectra at different pressures by pumping air into the chamber using the syringe allowed calibration of the pressure response. Calibration of the temperature response involved obtaining optical spectra at different temperatures, controlled by the thermoelectric control system, while leaving the chamber open to atmospheric pressure.

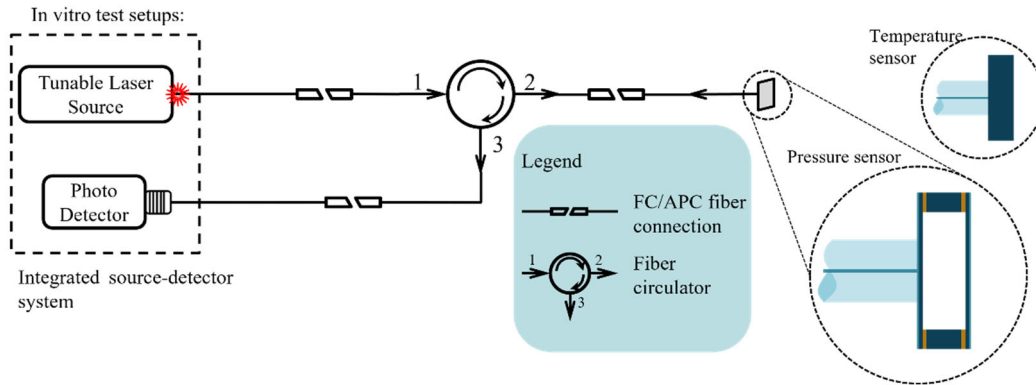


Figure 20 Illustration of the testing setup for fiber integrated FPI sensors.

We fabricated several sets of devices with different parameters as seen in Table 2, along with the summary of their performances. Notice that the sensitivity and the dynamic sensing range are tradeoffs of each other, while the temperature influence is determined more by the volume of the air chamber than the thickness of the Si NM. Figure 21 shows the spectrum of 10 μm thick FPI pressure sensor when (a) under varying pressure at 36 $^{\circ}\text{C}$ and (c) at rising temperatures under 1atm

pressure. The mode shift dependence on pressure and temperature are shown in (b) and (d) respectively. Mechanical and optical simulations yield insights into the mechanisms associated with these measured responses.

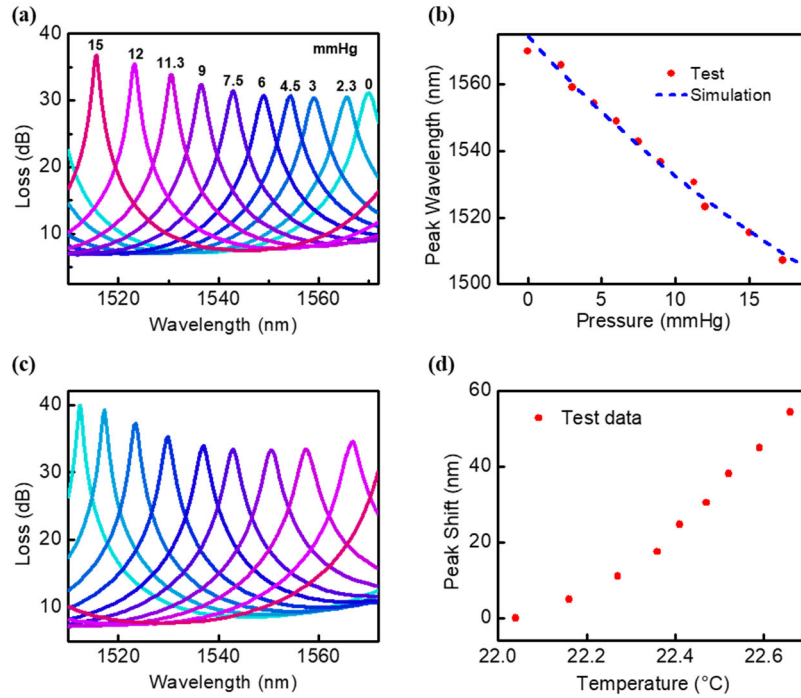


Figure 21 Measured spectrum of 10µm thick FPI pressure sensor

(a) under varying pressure at 36°C and (c) at rising temperatures under 1atm pressure. Mode shift dependence (b) on pressure and (d) on temperature extracted from (a) and (c) respectively.

Three-dimensional finite element analysis (3D-FEA) yields estimates of the vertical displacement of the diaphragm due to changes in external pressure. Computational electromagnetism (CEM) analysis determines spectra for cavity geometries defined by these mechanical computations. The combined simulation data match well with experimental pressure calibration curves in Figure 21(b). The results indicate a pressure sensitivity of -3.8 nm/mmHg and accuracy of ±0.40 mmHg for the FPI pressure sensor in 0-15 mmHg range. Note this pressure range

can be expanded significantly, by either changing the pressure sensor sensitivity, or by using a light source with an even broader spectral coverage, or by tracking other resonances. Approaches that rely on calibration tables and automated peak detection algorithms can be used in this case.

As shown in Table 2 , by comparing the performances of different devices with different chamber thicknesses, Si NM thicknesses, we come to the following conclusion in the FPI sensor design:

- (1). The chamber wafer (SOI-A) should be around 20 μ m, to allow 2 FPI modes in the target range, and device dissolution time within one year if implanted into human body.
- (2). 250nm thick Si NM provides high sensitivity around -3.8nm/mmHg, and can maintain functionality for around one week before dissolution

Table 2 Comparison of deferent FPI pressure sensor and PhC pressure sensor performance

Type	Device	Top BOX	Top Si	Air	Sensitivity	Range	Pros	Cons
FP	t31	1	250	100	0.14	>70	Various sensitivity and sensing range; Fiber integration	
	t32	1	250	100	0.17	>70		
	t43	3	250	10	2.9	27.3		
	t35	0	250	100	12	1		
	t44	0	250	10	29	4.5		
PC	PC03	3	250	100	0.0143	/	Large sensing range	Low

The essential characteristics of a sealed air chamber in FPI sensors brings along the inherent nature of temperature dependence performance. This dependence is more dominant in the

case of a smaller chamber according to the ideal gas law $pV = nRT$. It is necessary to develop compatible devices to extract the temperature information of the pressure sensor.

2.3 Development of FPI and photonic crystal (PhC) temperature sensor

2.3.1. Temperature dependence of refractive index of silicon

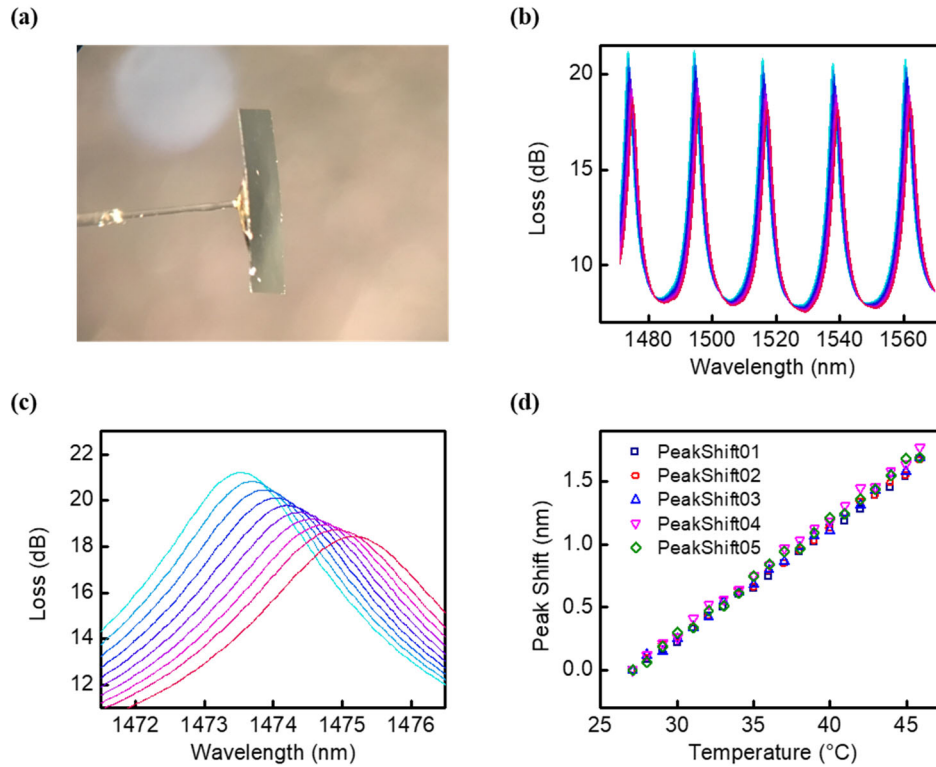


Figure 22. Photograph and measured spectra of an FPI temperature sensor

(a) Photograph of a Si FPI temperature sensor on fiber tip; (b) measured spectrum of the FPI sensor; (c) zoom-in spectrum of the first peak in (b); and (d) the sensitivity of all peaks extracted from (b).

Our FPI temperature sensor is Si based for the purpose of CMOS compatible fabrication process, as well as its bioresorbability. Si also has a relatively high thermos-optic coefficient (dn/dT)

among other semiconductor materials, $1.88 \times 10^{-4} K^{-1}$ against most others at 10^{-6} level. To demonstrate the feasibility of implementing Si as a temperature sensing material, we fabricated simple FPI temperature sensors on a fiber tip, similar to the pressure sensor, with only a $10 \mu\text{m}$ Si slab as the FPI cavity. Figure 22 (a) is the photograph of this sensor. Figure 22 (b) shows the measured spectrum of the sensor as the temperature changes. In our target wavelength range there are 5 modes, the zoom-in view of the first one is shown in (c), and the sensitivity of all modes are shown in (d). Among other reported temperature sensors, this sensor has a relatively high sensitivity of $98 \text{pm}/^\circ\text{C}$.

2.3.2. Photonic crystal temperature sensor on SOI substrate

Photonic crystal (PhC) is a 2-dimensional structure periodically arranged to regulate refractive index. It provides effective way to achieve reflection or transmission characteristics that can be implemented for sensing characteristics.

We fabricated a filter-type SOI based PhC structure for temperature sensing, implementing the exact same characteristic of Si as discussed in previous section. This offers a practical method later to integrated temperature compensations FPI pressure sensor. The fabrication process of PhC temperature sensor is similar to that of FPI, except for the top Si NM which goes through an extra step of PhC patterning on the SOI A by electron beam lithography. This sensor is a standalone device, and the measurement is done with a free space optical setup where collimated light incident on the surface normally and the reflected power is collected.

Figure 23(a) shows the illustrative sketch of the SOI PhC sensor; its spectrum measured at room temperature in (b), compared to the simulation from rigorous coupled wave analysis (RCWA) tool Stanford Stratified Structure Solver (S4) [23]. Figure 23 (c) shows the measured spectrum with polarizers added in the light path to filter out the non-resonating part of the signal. The temperature sensitivity of $81 \text{pm}/^\circ\text{C}$ extracted from (c) is shown in part (d). This means although PhC structures

has smaller sensitivity than FPI structure, it is still a feasible candidate for temperature compensating on the proposed FPI pressure sensor

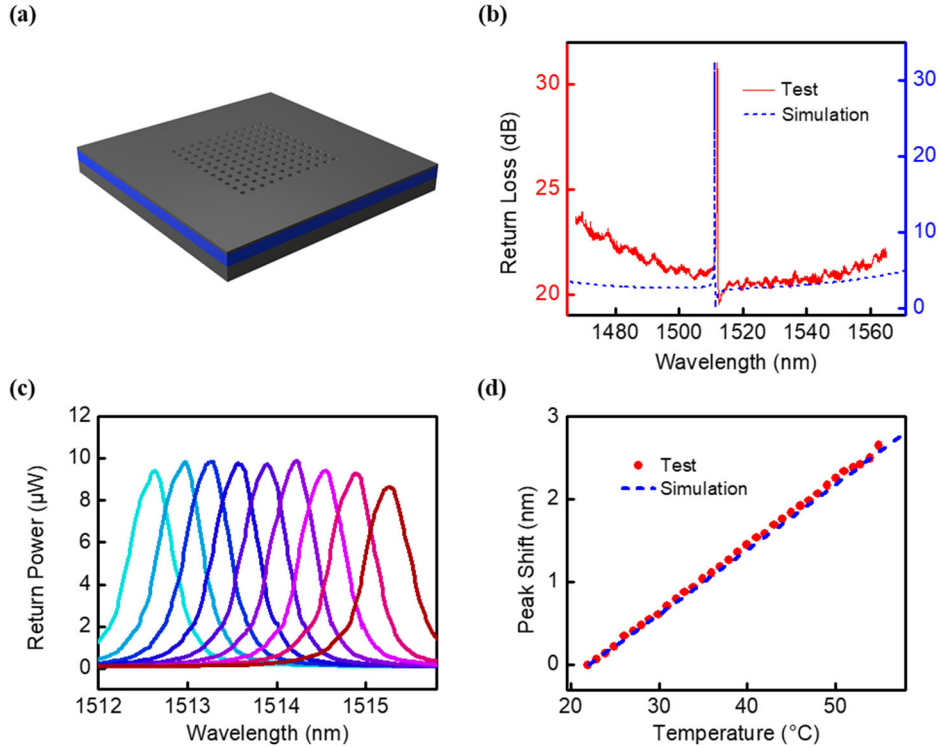


Figure 23 Schematic and spectra of PhC temperature sensor

(a) illustrative cartoon of a SOI photonic crystal temperature sensor; (b) measured spectrum of the PhC temperature sensor; (c) measured mode shift at different temperature; and (d) temperature sensitivity extracted from (c).

2.3.3. Proposed FPI pressure sensor with PhC feature for temperature compensation

For an effective way to decouple the temperature influence from the pressure measurement of our FPI sensor, we proposed a PhC integrated FPI configuration that can sense temperature and pressure simultaneously. As discussed above, Si PhC structure is also a good candidate for

temperature sensing, with slightly smaller sensitivity. Adding a PhC sensing configuration to the original FPI sensor gives at least clearly distinctive modes in both simulation and experiment.

Figure 24 (a) shows the illustrative sketch of the components for a PhC integrated FPI pressure sensor. In this configuration, there is an extra PhC Si NM in the place of the original FPI sensor working as a temperature sensor. Figure 24 (b) shows the simulated spectrum of the device at fixed pressure and temperature. Labeled peaks 1 are the FPI modes of the air cavity for pressure sensing, labeled peaks 2 and 3 are the PhC modes of Si NM for temperature sensing. The FPI modes are broader, presenting more as a background compared to the sharper PhC modes. Experimentally the spectrum of this configuration agrees more to the simulated spectrum, eliminating the difficulties of separating 2 types of modes. In fact, the measured data in Figure 24(b) is an example of such spectrum, where the narrow PhC mode resides on a broader FPI background (too broad to see in the limited testing range though). Figure 24 (c) is the simulated spectrum of this device under assumed rising pressure with no temperature variation. The extracted peaks of the PhC mode shows no fluctuation at all, since the 2 resonances are totally of different mechanisms with no interaction.

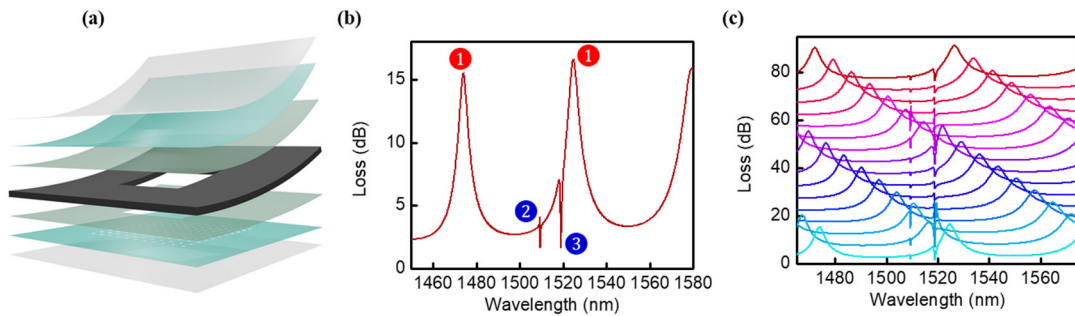


Figure 24 Sketch and simulated spectra of FPI+PhC sensor

(a) Sketch cartoon; (b) simulated spectrum at room temperature and 1atm pressure; and (c) simulated spectrum under applied pressure of FPI pressure sensor with PhC temperature compensation. FPI mode is labeled as 1, and PhC mode is labeled 2 and 3 in (b).

2.4 Bio-implantable angle independent free-space temperature sensor.

Measuring temperature of tissue microenvironments serves as a simple, yet effective approach in constructing diagnostic conclusions for a wide range of diseases and illnesses, including chronic inflammation, traumatic injury, immunological disorders, organic failures, neurological disorders, and many others. Thermoregulatory processes ensure normal cellular functions by maintaining core-body temperature homeostatically balanced with energy production and dissipation coordinated through metabolic mechanisms, local-tissue perfusion, and hemodynamics. Abnormality in values and/or temporal patterns of local-tissue temperature associated with certain immune responses and metabolic adjustments can provide early signs of critical illness, as the basis for proactive treatments with timely and effective optimization. Traditional thermal sensors such as infrared digital cameras, metallic thermistors, and others provide measurements at surfaces that are either visually or physically accessible. Precise and continuous measurements of temperatures at regions deep inside body, however, require invasive probes and/or disruptive surgical interventions, with potential for various adverse effects, including infection, immune response, and scar formation.

To extract the temperature information from deeper-tissue locations, the bioresorbable sensor must work wirelessly or cable free to enable long term measurement tracking. It then brings up new issues in non-guided optical sensing/imaging, particularly the angle dependency of light propagation upon the sensing components.

We designed, fabricated, and tested an angle independent bioresorbable multilayer cavity structure with standard CMOS compatible processes. The device consisted of one silicon Fabry-Perot cavity and one Distributed Bragg Reflector (DBR) structure, it utilized the high contrast in the thermos-optic coefficients between silicon and silicon nitrides/oxides: for Si, SiN_y and SiO_x, $dn/dT \sim 2 \times 10^{-4} \text{ K}^{-1}$, $2 \times 10^{-5} \text{ K}^{-1}$, $1 \times 10^{-6} \text{ K}^{-1}$ respectively.

2.4.1. Individual Fabry-Perot and DBR cavities

First, we fabricated the Si FPI slab F-P cavity and the SiOx/SiNy DBR cavity, individually, to verify the fabrication process and the thickness accuracy. Figure 9 shows the comparison of spectra of simulated data and measured data of the Si FPI and the DBR cavities.

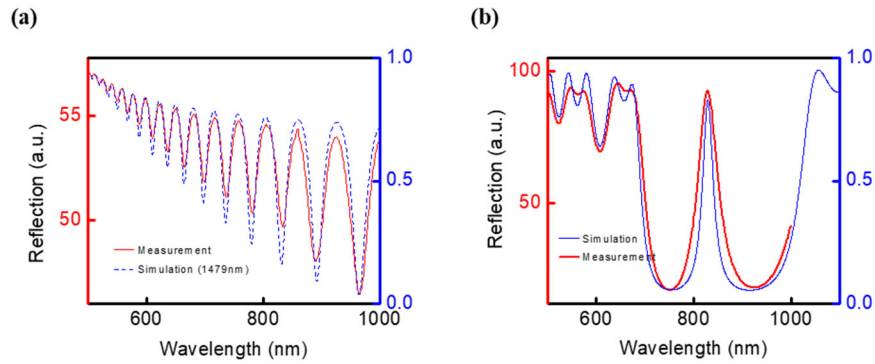


Figure 25 Simulated and measured spectra of the Si FPI and Oxide/Nitride DBR Cavities (a) Si slab F-P cavity and (b) SiOx / SiNy DBR cavity

For both Si F-P cavity and the SiOx/SiNy DBR cavity, the reflection depends on both the refractive index and propagation length (angle dependent) in the cavity, but on different levels, which enables the combined device to work as a temperature sensor with angle independency. Table 3 shows the differences in temperature and angle dependencies of Si F-P cavity and DBR defect cavity.

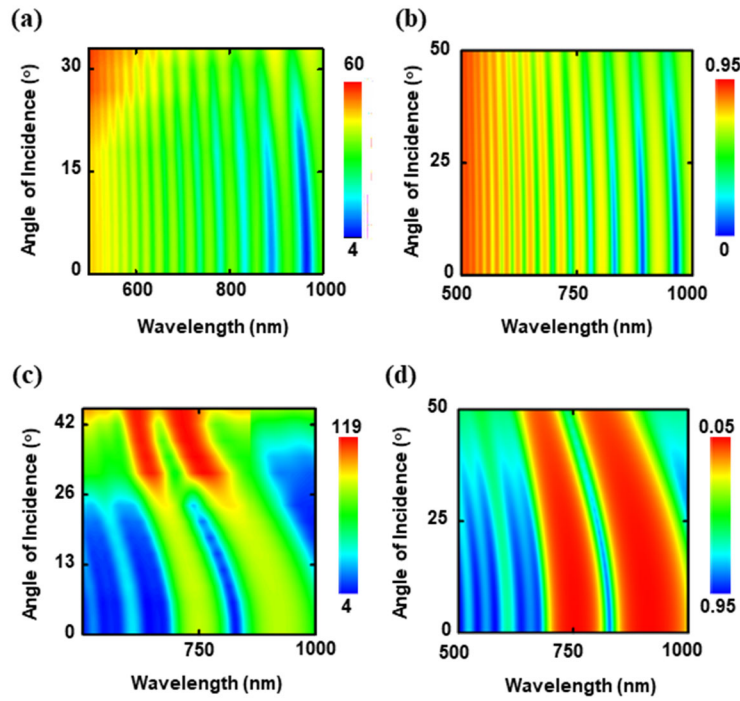


Figure 26 Reflection intensity maps of FPI and DBR cavities

Measured and simulated temperature contour plot of (a), (b) Si slab F-P cavity and (c), (d) SiOx / SiNy DBR cavity respectively.

Table 3 Temperature and angle sensitivity of F-P modes and DBR mode

	Si F-P cavity	DBR defect cavity
Temperature (nm/°C)	0.047	10^{-15}
Incident angle (nm/°)	-0.30	-1.32

Figure 26(a) and (b) show experimental and simulation results for reflection spectra of the Si F-P cavity (1.5 μm thick) at various angles of incident light. The resonant peaks shift by ~0.3 nm per degree, with good agreement between experiment and simulation. The DBR defect cavity

exhibits a large angular dependence, with shifts of ~ 1.32 nm per degree, as shown in Figure 26 (c) and (d).

2.4.2. Design, fabrication, and testing of F-P/DBR multilayer temperature sensor

Figure 27(a) shows the Scanning Electron Microscope (SEM) image and (b) schematic illustration of the fabricated multilayer temperature sensor. It consists of three parts: (i) a distributed Bragg reflector (DBR) made of alternating layers of silicon oxides (SiO_x) and silicon nitrides (SiN_y) with a layer of SiO_x (twice the thickness of the others) in the center to yield a defect cavity; (ii) a $1.5 \mu\text{m}$ -thick membrane of monocrystalline silicon (Si), to create a Fabry-Perot resonance (Si F-P cavity); and (iii) a $10 \mu\text{m}$ -thick substrate of poly(lactic-co-glycolic acid) (PLGA) to provide mechanical support during surgical implantation. The total thickness of the multilayer reflector is $\sim 13.6 \mu\text{m}$. The structures studied here have lateral dimensions of 3 mm by 3 mm.

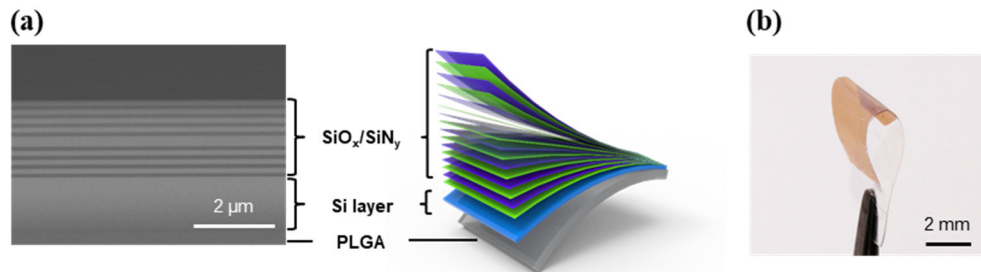


Figure 27 Structure of the DBR defect temperature sensor

(a) Scanning Electron Microscope (SEM) image and (b) schematic illustration of the multilayer temperature sensor, and (c) photograph of the device hold on a twiser.

In our device design and mechanism, we only take into consideration the thermo-optic effect, and ruled out the thermal expansion effect based on the comparison of orders of those coefficients. Equation (1) below defines the q^{th} peak wavelength of a F-P cavity with thickness t and refractive index n , and Equation (2) defines the 1-D thermal expansion coefficient of an object of length t . Since for silicon material the thermal expansion coefficient is almost 2 orders smaller than

thermo-optic coefficient, as the derivation in equation (3) shows, the shifts in the resonant peaks for the structures reported here, therefore, can be considered to arise almost entirely from the thermo-optic effect.

$$\lambda_q = \frac{2nt}{q} \quad (1)$$

$$\alpha = \frac{1}{t} \frac{dt}{dT} \quad (2)$$

$$\frac{d}{dT} \lambda_q = \frac{2}{q} \left(\frac{dn}{dT} t + \frac{dt}{dT} n \right) = \frac{2}{q} \left(\frac{dn}{dT} t + \alpha n t \right) = \frac{2t}{q} \left(\frac{dn}{dT} + \alpha n \right) \cong \frac{2t}{q} \frac{dn}{dT} = \frac{\lambda_q}{n} \frac{dn}{dT} \quad (3)$$

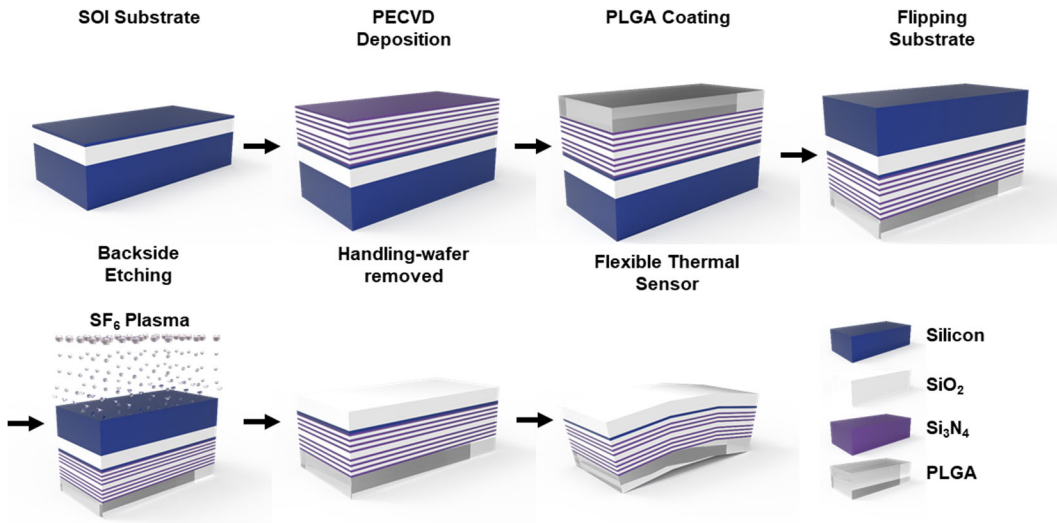


Figure 28 DBR temperature sensor fabrication flow

3D schematic illustration of key fabrication steps for a bioresorbable multilayer photonic cavity reflector.

Figure 28 shows the schematic illustration of the fabrication process for the multilayer temperature sensor. Fabrication began with programmed deposition of alternating layers of SiO_x and SiN_y using Plasma-enhanced chemical vapor deposition (PECVD) onto a Silicon-On-Insulator wafer (thickness of device layer: 1500 nm; thickness of buried oxide layer: 1000 nm; Base silicon (Si) layer polished to a thickness of 200 μm). Spin coating polyimide (PI) at 3000 rpm for 30 s and

baking at 250 °C for 1 hour yielded a 2 μm-thick PI film on the surface of the multilayer. Etching under a vapor of xenon difluoride removed the Si wafer from the backside. Drop casting PLGA from ethyl acetate solution (7 wt%) and baking at 70 °C for 10 min produced a 10 μm-thick coating of PLGA on the multilayer to complete the fabrication.

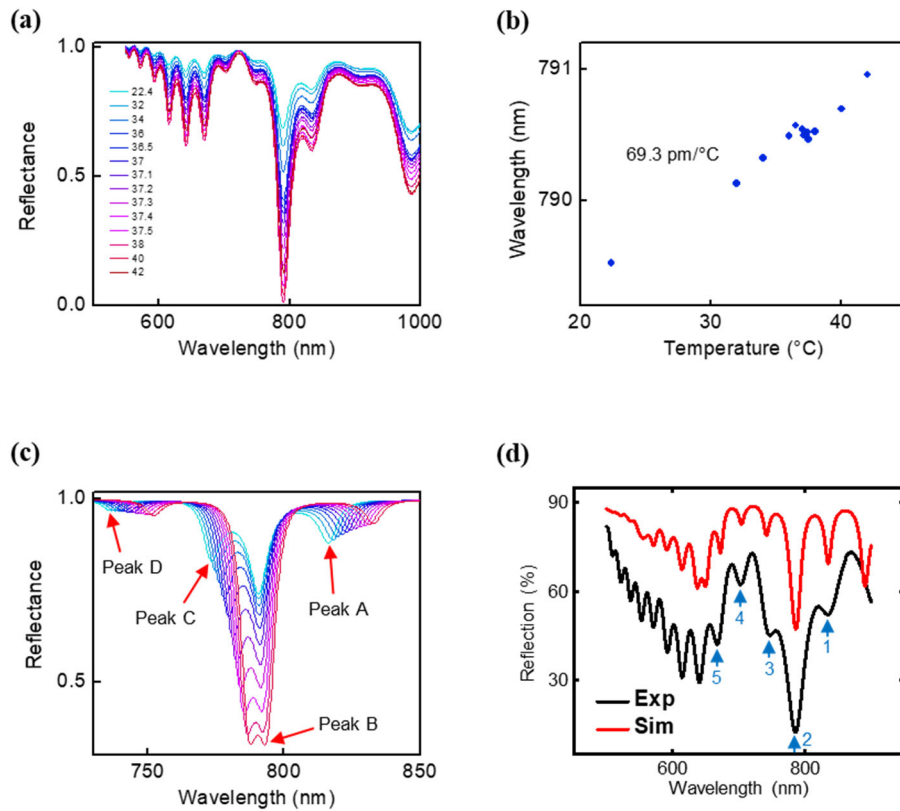


Figure 29 Measured and simulated spectra of the DBR temperature sensor
 (a) measured spectra of the multilayer sensor under varying temperature. (b). Peak shift of the F-P mode. (c) simulated spectra of the device temperature performance at normal incident condition. (d) comparison of the simulated data and measured data.

Figure 29(a) shows the measured spectra of our multilayer device under increasing temperature and the shift of the F-P mode peak is shown in (b); (c) shows the simulated reflectance spectra of the sensor under increasing temperature at normal incident condition, and (d) is a comparison of the simulated and measured spectra.

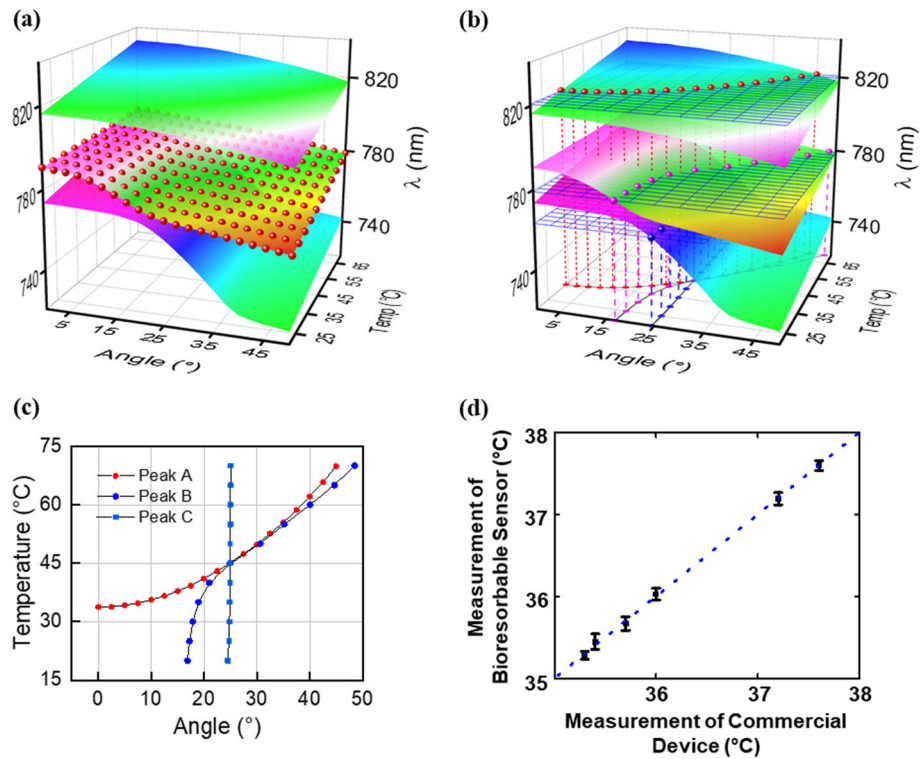


Figure 30 Measurement principle of the DBR temperature sensor

(a) peak surfaces of simulated reflection spectra under changing temperature and incident angle where the red sphere represents a surface reconstructed from fitting function of the original surface. (b). temperature-angle projection onto the simulation surfaces from 3 measured peak values. (c) projected temperature-angle lines from (b); and (d) comparison of the extracted temperature and reference temperature..






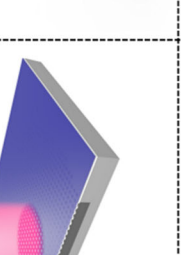
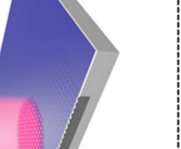

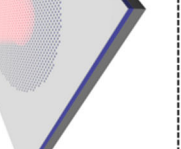

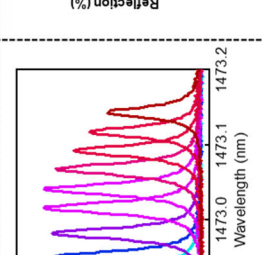
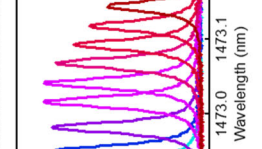
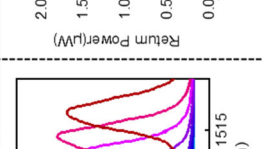
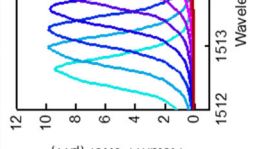
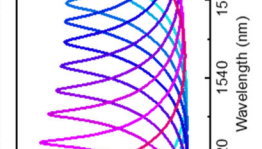
The mechanism of measuring temperature with our multilayer device involves matching simulation and pre-calibration of the device in lab, construction of peak-temperature-angle surfaces as the look-up surfaces, and projection of measured peaks onto these surfaces to extract the temperature-angle information.

As shown in Figure 30(a), we plot the peaks from simulated spectra as functions of temperature and angle, and then find the fitting function of each surface. To show how well these functions are, a re-constructed surface is also plotted for the middle surface in red sphere points. We use the fitting surface functions to find temperature and angle by substituting 2 or more measured peaks into 2 surfaces and solving the equations. This process is visualized in (b) where each given (measured) peak value is projected onto corresponding surface, the result interception lines are only temperature-angle lines that can be casted onto the temperature-angle coordinates, as shown in (c). 2 of such lines would determine a single temperature-angle point, which is the measurement condition. Using more peaks would increase the accuracy of the projection. The comparison of the projected temperature and the reference temperature is shown in (d).

2.5 Summary of sensors

We explored the optical pressure and temperature sensors with different sensing mechanisms including Fabry-Perot interference, photonic crystal resonance, and distributed Bragg grating defect mode. The summarized performance comparison of these sensors is list in Table 4 below. We conclude that it is totally feasible to develop all optical and bioresorbable sensors that can work in the implanted biomedical environments to provide the temperature and pressure information for biomedical treatment and diagnostic purposes.

Table 4 Summary of all bioresorbable optical sensors

FP temperature sensor	FP pressure sensor	PC temperature sensor	PC pressure sensor	DBR temperature sensor
Si NM on fiber 	FP cavity with Si NM on fiber 	Si PC on SOI wafer 	FP cavity with Si PC in free space 	
				
				
89.8pm/°C	-3.8nm/mmHg	79.7pm/°C	1.9pm/mmHg	69 pm/°C

This page is left black intentionally

CHAPTER 3.

SINGLE SHEET 2D MATERIAL PHOTONIC CRYSTAL LASERS

3.1 Introduction

Ultra-low threshold and power consumption lasers and light emitting diode (LED) have always been attractive for researchers. Monolayer transition metal dichalcogenide (TMDC) is an ideal candidate for such applications thanks to its direct bandgap, strong optical absorption, and ultimately thin active region. In recent years, TMDC based lasers [56-61] and LED [62-66] have been developed on various optical cavities including micro-disk cavities [56,58] and photonic crystal (PhC) defect mode micro-cavities [57], with emission wavelength over both visible and infrared range. However, the emission from these devices has a large divergence angle, which requires a high numerical aperture (NA) lens to collect and is impractical in. To reduce the emission divergence, distributed Bragg reflector (DBR) cavity was introduced, which intrinsically has a surface normal emission, but in turn compromises the small volume and linewidth advantages of the TMDC material.

Here, we propose a lateral confinement scheme heterostructure photonic crystal surface emitting laser (PCSEL) design that can provide large area lasing with high beam quality [67]. Unlike the PhC defect-based cavity that relies on the in-plane band gap below the light line, our PCSEL cavity is based on the Fano resonance at the mode gap near the Γ point above the light cone created by modulation of the hole radii. This design can also relax the index contrast requirements in the vertical direction.

We will present and experimentally demonstrate PCSEL on a silicon nitride (Si_3N_4) slab with monolayer tungsten disulfide (WS_2) as the gain medium.

3.2 Laterally confined heterostructure 2D photonic crystal cavities

Enabled by the slow light phenomenon at the band edge, photonic crystal heterostructure cavities have been widely used for achieving lateral confinement within two-dimensional photonic crystal slabs. Heterostructure cavities can be formed by either modulating the filling factors [68-71] or embedding different types of lattices [72]. Currently, most reported heterostructure PhC cavities are based on the band edge modes below the light cone, where the light is vertically confined within the dielectric slab by total internal reflection. However, the emission from such cavities is strongest at large angles from the surface normal direction. There is also an increasing interest on the PhC modes above the line cone [13]. Particularly, at the Γ point the radiation is intrinsically surface normal and an extremely high quality factor (Q) can be made possible using the concept of bound state in continuum [73] (BIC).

Our BIC cavity design is a hexagonal PhC lattice of air holes on a 112 nm thick silicon nitride (Si_3N_4) slab on quartz, with the lattice constant $a = 454$ nm. With such a low contrast of refractive index between the PhC slab and the substrate, achieving vertical confinement through index guiding, and lateral confinement through a complete in-plane band gap are both challenging. Instead, we looked into the modes above the light cone. It is well known that a symmetry-protected bound state in continuum (BIC) exists at the Γ point with an infinite vertical quality (Q) factor [13]. For a finite structure, the pseudo-BIC near Γ would provide a sufficiently high Q for vertical confinement. And lateral confinement can be realized by utilizing a mode gap and the mismatch of modes at different bands [74]. Previous work [74-76] has established the photonic crystal design and fabrication process on bulk WS_2 material integrated laser.

The cavity structure is shown in Figure 31(a). The photonic crystal lattice is divided by the hexagonal dashed lines into three regions: the cavity “core region” in the center, the “cladding region” at the outside and the “transition region” in between. The period of the holes is kept constant at $a = 470$ nm while the hole radii r is slightly different for each region. To be specific $r_{\text{core}} = 0.24a$, $r_{\text{trans}} = 0.22a$, and $r_{\text{clad}} = 0.2a$.

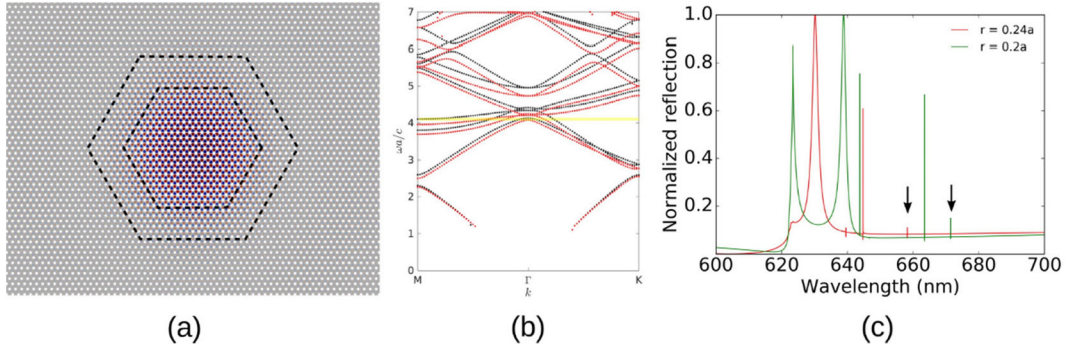


Figure 31 Design of the lateral confined heterostructure photonic crystal cavities

(a) FDTD simulated magnetic field H_z of the resonant mode, overlaid with the heterostructure photonic crystal. Regions of different hole radii are separated with dashed lines. (b) Band structure of the cavity core (black) and cladding (red) regions. (c) Simulated reflection spectra of the core (red curve) and cladding (green curve) photonic crystals. The arrows indicate the positions of the first order dark mode.

Figure 31(b) shows calculated band diagram for both core (black) and cladding (red) photonic crystals. As the first order dark mode is non-degenerate, a mode gap (yellow) can be seen near Γ where the modes of the core region cannot propagate in the cladding region thus are laterally confined. Figure 31(c) shows calculated near-normal incidence (tilted by 0.1° to excite the dark modes) reflection spectra of both core (red) and cladding (green) photonic crystals. The positions of the first dark mode considered are marked by black arrows

3.3 Integrated 2-dimensional material laser

3.3.1. Monolayer WS_2 transfer printing

After identifying the device with a high Q resonance in the wavelength range of interest, large area monolayer WS_2 was prepared and transferred onto the sample.

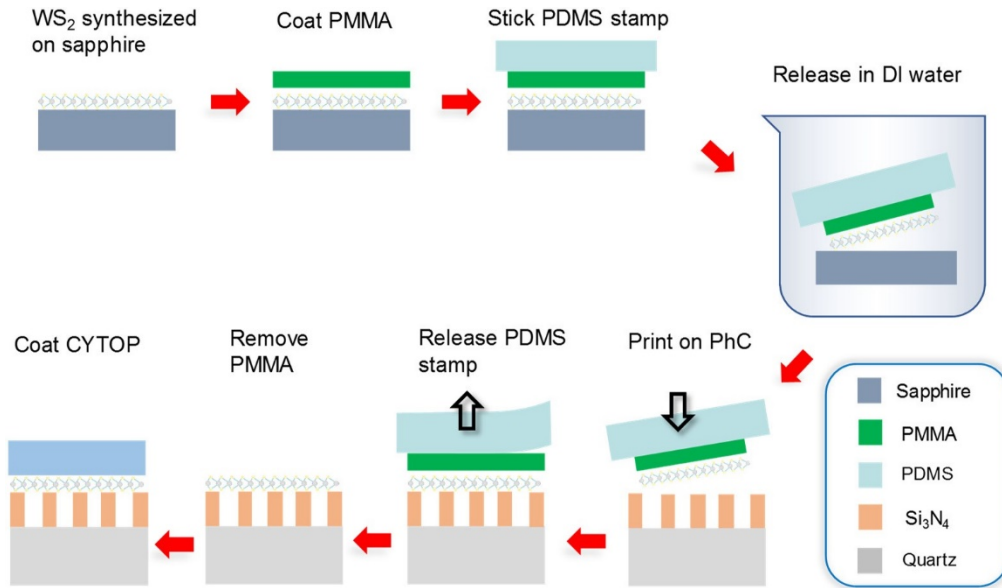


Figure 32 Processing flow of integrating large area synthesized WS₂ onto Si₃N₄ PhC cavity.

As shown in Figure 32, we developed a water-based method for releasing and transferring synthesized TMDC. As the sapphire substrate that the TMDC is grown on is more hydrophilic than the SiO₂ substrate we used for exfoliated flakes, and generally no alignment is required for the large area film, the overall process is much simpler and has the potential in practical applications. The PMMA film is firstly spun-coated onto the TMDC and baked to form a carrier for mechanical support during releasing. It can also act as a buffer layer between the TMDC and PDMS to reduce contamination. The PDMS stamp on a glass handler is then attached to the PMMA and the full stack is immersed into DI water. After a brief ultrasonication, water penetrates between the TMDC film and sapphire which releases the film from substrate. The release film can be transferred onto the target by either transfer-printing or heating. To protect the TMDC from exposure to oxygen and water, after removing the PMMA carrier and drying the film, we coated a layer to CYTOP as encapsulation.

Shown in Figure 33(a) is the 3D sketch of the integrated WS_2 material with Si_3N_4 PhC cavity of 160 nm thickness on quartz substrate. Large area $1\text{ cm} \times 1\text{ cm}$ WS_2 material is transfer-printed with PDMS stamp.

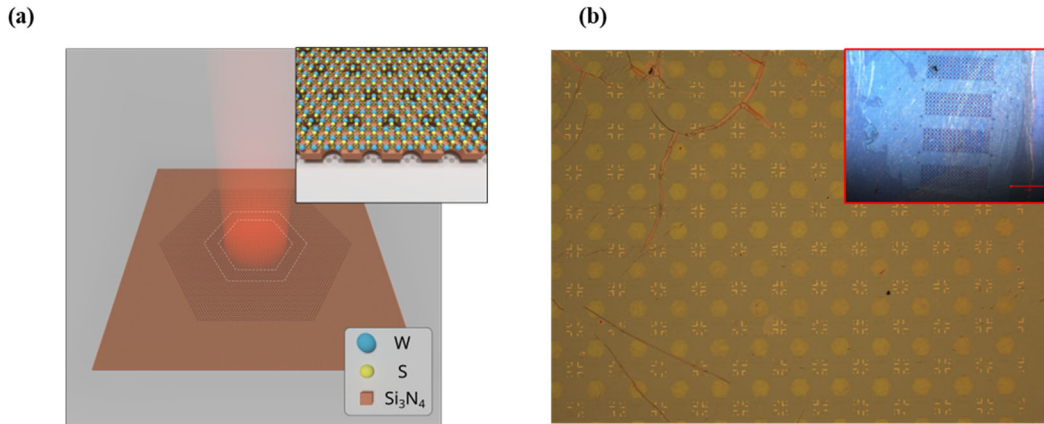


Figure 33 Schematics and micrograph of WS_2 integrated laser

(a) Schematic illustration and (b) surface micrograph of the heterostructure photonic crystal cavity with printed WS_2 material.

Figure 33(b) shows the surface micrograph of PhC cavity array, the inset displays the overall view of the printed surface area where 4 sets of cavity arrays devices are entirely covered with the 2D material.

3.3.2. Heterostructure PhC laser characterization

The resonance characteristics of the PhC cavity array is measured by pumping the defect state in the Si_3N_4 film at room temperature using a 450 nm laser diode with continuous wave (CW) mode at power level of 1mW and spot size of $1\mu\text{m}$ diameter. Figure 34(a) shows the resonance spectra of one row in the Si_3N_4 PhC cavity array where the lattice constant is set to an increasing order from 465 nm to 490 nm.

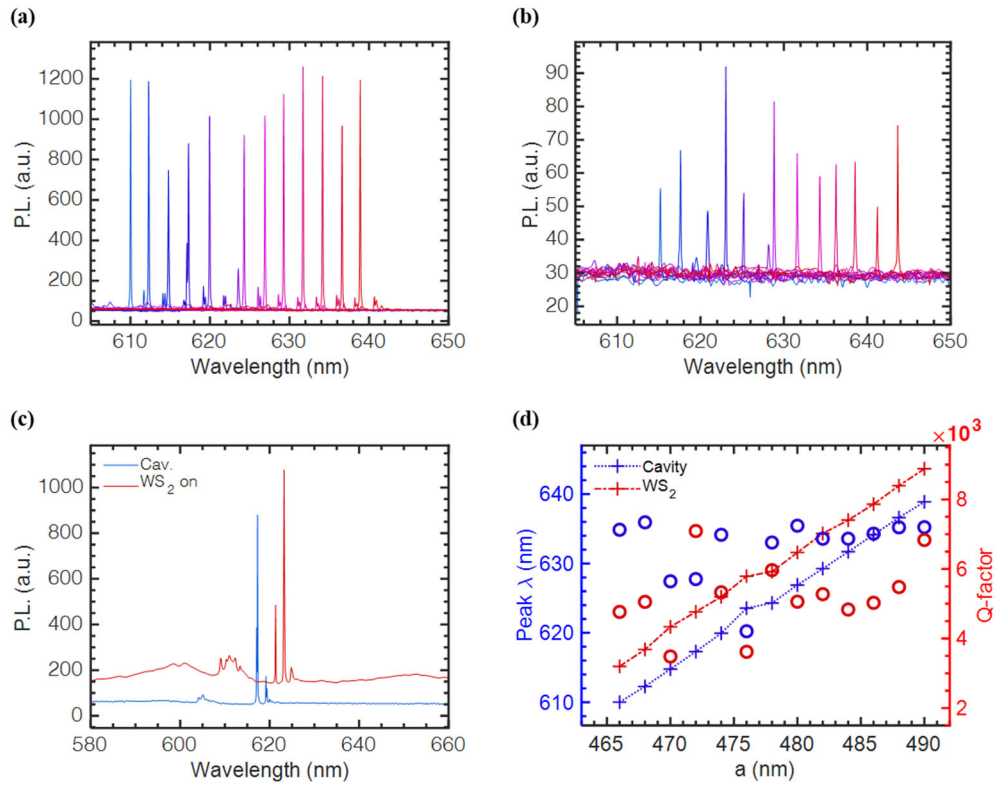


Figure 34 Optically pumped photonic crystal illumination

(a) before and (b) after WS₂ printing; (c) comparison of the illumination spectra before and after WS₂ printing. (d) comparison of the resonance wavelength and quality factor before and after WS₂ printing.

The water-based method transfer-printing process previously developed is used for releasing and transferring synthesized TMDC. After integration of WS₂, the devices were pumped at room temperature using a 450 nm laser diode operated in quasi-CW mode (100 ns width, 10% duty cycle). Features corresponding to the cavity resonances can be clearly identified in Figure 34(b). One-by-one comparison of the cavity resonance spectra before and after WS₂ integration is plotted in in Figure 34(c). The resonance peak shift and quality factor (Q) change of the cavity row is shown in Figure 34(d), where the fundamental mode has a 10 nm red shift and around 2×10^3 Q factor decrease caused by the WS₂ layer and the protective CYTOP layer.

It proves that the large area transfer printing of CVD grown WS_2 material is a reliable method for integrating the monolayer threshold-less laser, which preserves the material integrity and optical emission properties. This could provide an effective way to produce low power consumption, large area laser arrays for low power sensing applications.

We characterized our integrated laser with power dependent measurement. Figure 35(a) shows 3D plot of the spectra of power dependent PL measurement on one PhC device, with the x-axis in wavelength (nm), and y-axis in pumping power (μW). The peak intensity and linewidth are shown in Figure 35(b), we can observe the narrowing of the linewidth of the fundamental mode with increasing pump power, although the turn-on effect of the emission power is not as obvious in this case.

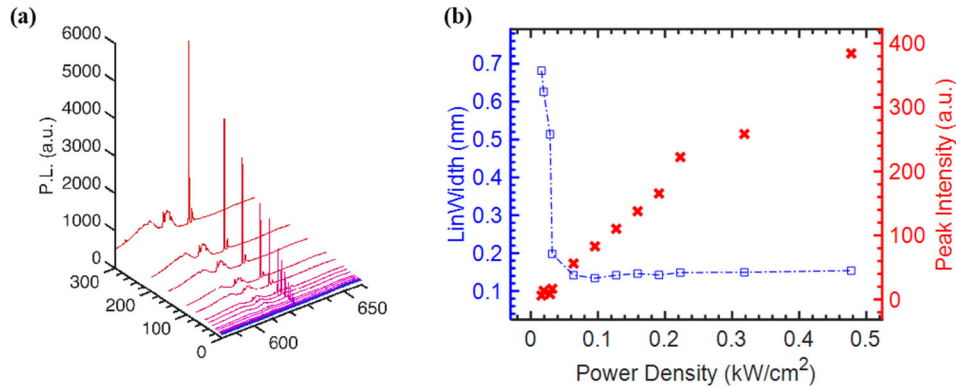


Figure 35 Laser characteristics of the heterostructure PCSEL

(a) Power dependent illumination spectra from the integrated WS_2 laser, and (b) the intensity-linewidth characterization.

3.3.3. Lattice design comparison

The far field emission pattern is affected by airhole symmetry in the lattice [77,78]. Two different airhole shape were patterned with the same lattice and the compared result is shown in

Figure 36. The measured result in Figure 36 (a) shows that circular airhole shape has larger Q-factor (plotted in blue circles) overall and has a resonance wavelength (plotted in blue crosses) is 2nm above that of the rectangular airhole. The pumping power dependent illumination and linewidth are plotted in (b) and (c), we can see that the lattice with circular airhole shape has higher turn-on power density. Although the linewidth narrowing of these emissions are obvious, their threshold power behavior is not as clear as in a typical laser.

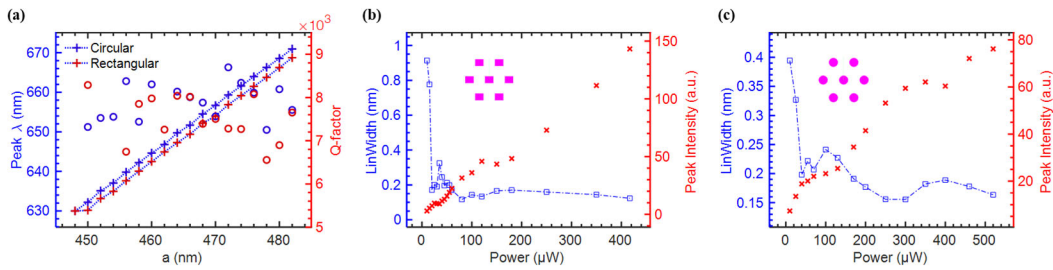


Figure 36 Comparison of illumination from rectangular and circular airhole hetero PhC

(a) Optical performance comparison of circular shape airhole rectangular shape airhole cavities. (b) lasing characterization of rectangular airhole PhC cavity. (c) lasing characterization of Circular airhole PhC cavity. The insets in (b) and (c) are the sketches of each lattice layout.

3.3.4. 2D material metrology comparison

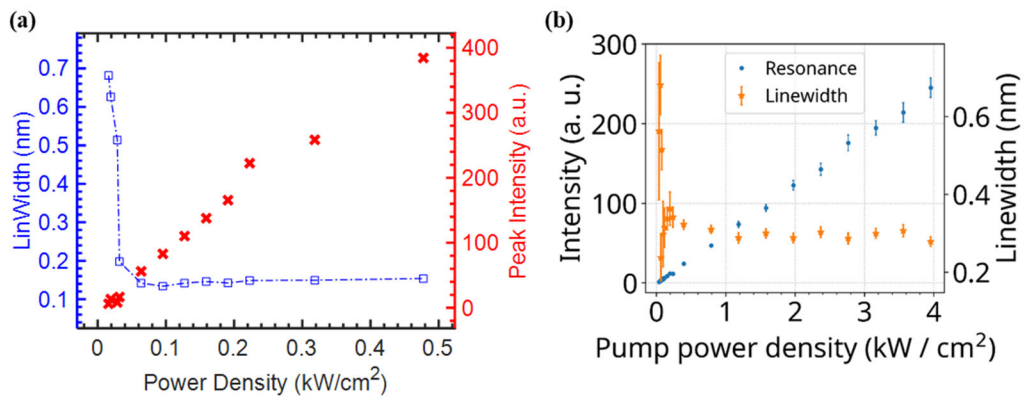


Figure 37 Comparison of laser characteristic from 2 types of WS₂ material

(a) Lasing characterization of device integrated with CVD 2D material. (c) lasing characterization of device integrated with bulk 2D material.

The improved fabrication process not only made it possible for cm-scale integration of the 2D material, but it also affects the device performance. Figure 37 (a) and (b) are the pumping power dependent illumination characteristics of lasers fabricated from CVD grown 2D material and exfoliated 2D material from bulk. It is clearly seen that compared to the bulk material, WS₂ grown by CVD technology has much lower energy and higher efficiency as shown in Figure 37.

CHAPTER 4.

PHOTONIC CRYSTAL NANOBEAM CAVITIES WITH FINS

4.1 Introduction

During the last several decades, the field of photonic crystal have seen drastic developments in both theory and application [79-83]. Scaling of optical cavities has been of great interests for future high performance, low energy consumption and high-speed optical devices such as semiconductor lasers, light emitting diodes, optical sensors, and modulators. Nanobeam cavity, among other microcavities, has drawn stronger attention for its superior characteristics of ultra-compact size, extreme low mode volume (V), and high quality (Q) factor [84-87]. These characteristics have made nanobeam cavity a competitive candidate for nano lasers, on-chip modulators, optical switches, and filters [88]. In the past decade, nanobeam cavity on III-V platform has achieved lasing threshold of $2.3 \mu W$ by optical pumping [89] and $5 \mu A$ by electrical pumping [90]; Integrated lasers on silicon nitride nanobeam cavity have also demonstrated to be promising options for lasers on Si [91,92]. Nanobeam modulators on Si and Si integrated platforms have reached footprint of a few μm^2 [93] in experiment and have potentials to realize high modulation speed larger than 100 GHz at the energy efficiency below fJ/bit theoretically [94,95]. Nanobeam based optical switches utilize thermo-optic (TO) [96], Electro-optic effect [97], and Kerr nonlinearity [98] have been of growing interests for its simplicity in fabrication. On-chip nanobeam sensors can obtain figure of merit $>2,000$ for label free sensing, one order higher compared to other PC sensors [99].

However, the natures of ultra-high performance nanobeam resulted from deep etching [100] and suspending [101] also compromises the implementation of nanobeam structures. Current nanobeam cavities have non-negligible trade-offs in electrical/optical/mechanical/thermal efficiencies due to the required high index contrast cladding and suspended structure. Earlier, non-

suspending tunable nanobeam cavities were reported with one-sided nano-tentacles (connecting fins) that improves thermal conductivity and tunability [102]. Other configurations of vertical supporting structure were also proposed that offers electric injection for nanobeam lasers [90].

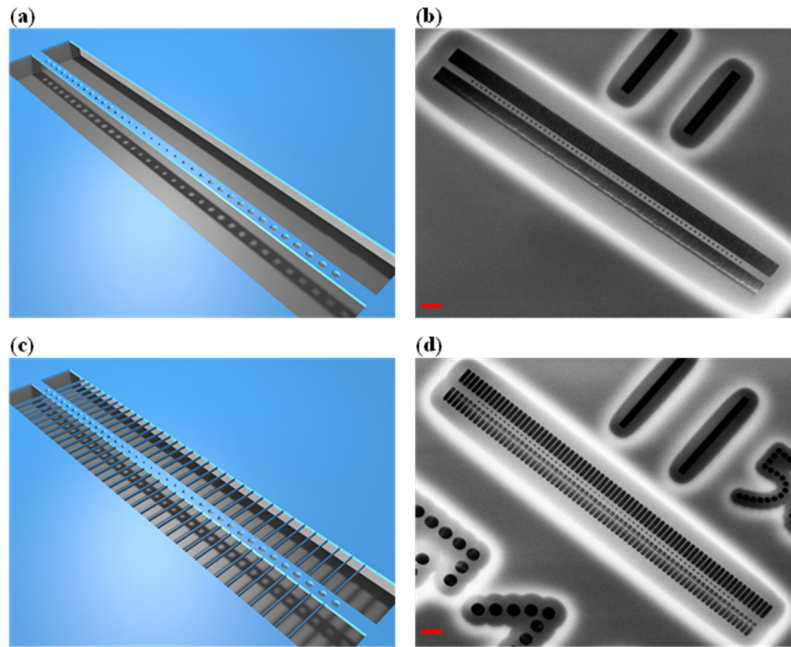


Figure 38 Schematics and SEM of suspended nanobeam cavities

(a), (c) Schematic illustrations and (b), (d) Scanning electron micrographs of the suspended nanobeam cavity without, and with fin structures, respectively. Scale bars in (b) and (d) are 1 μm .

In this dissertation, we propose and investigate a suspended silicon nitride PCNB cavity with lateral nanorod fin structures on both sides of the nanobeam cavity, where the alignment of the fin position is tunable to achieve a range of desired Q-factor and resonance wavelength. We also compare the optical performances of the very same PCNB with and without fins. The PCNB structures are shown schematically in Figure 38(a) and (c), for PCNBs without and with fin structures, respectively. Shown in Figure 38(b) and Figure 38(d) are scanning electron micrographs (SEMs) for PCNBs without and with fins, respectively. Compared to the traditional suspended

nanobeam cavity, the introduction of the lateral fins improves the mechanical strength, thermal conduction, and electrical carrier injection of the suspended PCNB cavity.

4.2 Photonic crystal nanobeam cavity design

The PCNB cavity is designed to utilize the maximum mirror strength in the 1-D PC, thus it is desirable to have a symmetric radius taper of 6 periods on each side about the center of the cavity according to the deterministic method [103]. As shown in Figure 39(a), two different parabolic radius tapers are fabricated, one with taper radius changing from 46.9 nm to 66.8 nm (taper01, red square), and another with taper radius changing from 52.8 nm to 69.2 nm (taper02, blue circle), to verify the mirror strength theory. Figure 39(b) shows all the key design parameters for PCNB with fins, including cavity thickness t , PC non-taper regular radius r , PC lattice constant a , fin width w , beam width W_b , and the fin alignment position D . We define $D=0$ for fins aligned to the center point of 2 airholes, as shown by the solid fins; and $D=0.5a$ for fins aligned to the center of each airhole, as shown by the transparent fin. The optimized values by the deterministic recipe in [103] for these parameters are $r=71.8$ nm, $a=272$ nm, $w=30$ nm, $t=150$ nm and $W_b=300$ nm for the target resonance wavelength at 660 nm.

Previous work by J. Zhang [102] has demonstrated that the presence of an optimized lateral tentacle structure on one side of the cavity has minimal effect on the optical performance of the cavity. To investigate impact brought by the presence of fins on both sides of our PCNB cavities, we explored 2 scenarios of nanobeam cavity in numerical simulation as shown in Figure 40. a suspended nanobeam (a) without and (b) with fins; and a nanobeam cavity on SiO₂ substrate (c) without and (d) with fins. Simulations are performed with the finite-difference time-domain (FDTD) method, using an open-source software package [25]. It shows that the presence of fins on our PCNBs also has minimal impact to the mode distribution in the cavity and brings less than 2%

change in Q-factor when fins are thin ($\sim 0.1a$) and aligned to the electric field minima. This is verified by the experimental data shown later.

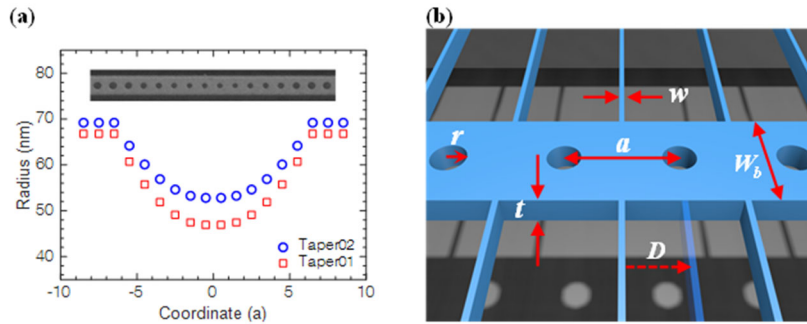


Figure 39 Design parameters of the nanobeam cavity

(a) Fabricated radius taper of the nanobeam cavity (inset is the SEM image of the taper part, and (b) defining parameters of the nanobeam cavity, the dashed arrow and the transparent fin illustrate the fin position shift in the cavity array.

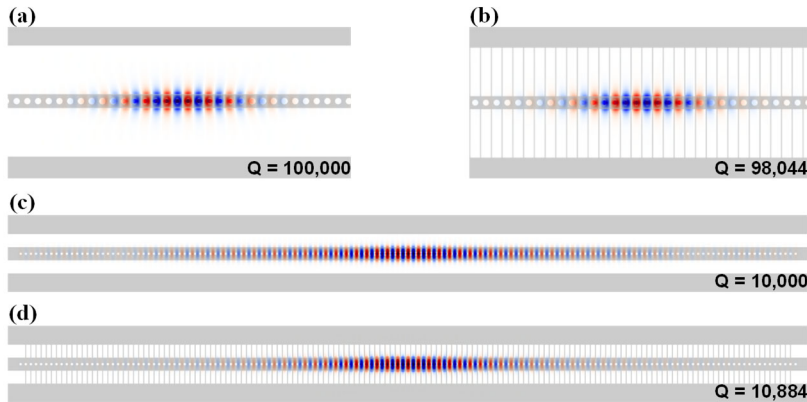


Figure 40 Simulation of field distribution of nanobeam cavity with and without fins

Comparison of simulated E_y component of the electrical field distribution and quality factor of suspended Si_3N_4 nanobeam cavity (a), without and (b), with lateral fins (fin width $0.1a$, 2nd order band edge of air mode), and of Si_3N_4 nanobeam cavity on SiO_2 substrate (c), without and (d), with lateral fins (fin width $0.2a$, 1st order band edge of dielectric mode).

4.3 Photonic crystal nanobeam cavity fabrication and measurement

4.3.1. Fabrication

The fabrication process of the PCNB cavities includes Si_3N_4 film deposition on Si wafer and PCNB cavity pattern lithography. The 150 nm thick Si_3N_4 film is stoichiometrically grown with low pressure chemical vapor deposition (LPCVD) method at 770°C on p-type silicon wafer in a Tystar Tytan nitridation furnace. The patterning of PCNB cavity consists of standard electron beam (e-beam) lithography (EBL), directional reactive ion etching (RIE) of Si_3N_4 layer, isotropic RIE of Si substrate, stripping and plasma cleaning of the e-beam resist.

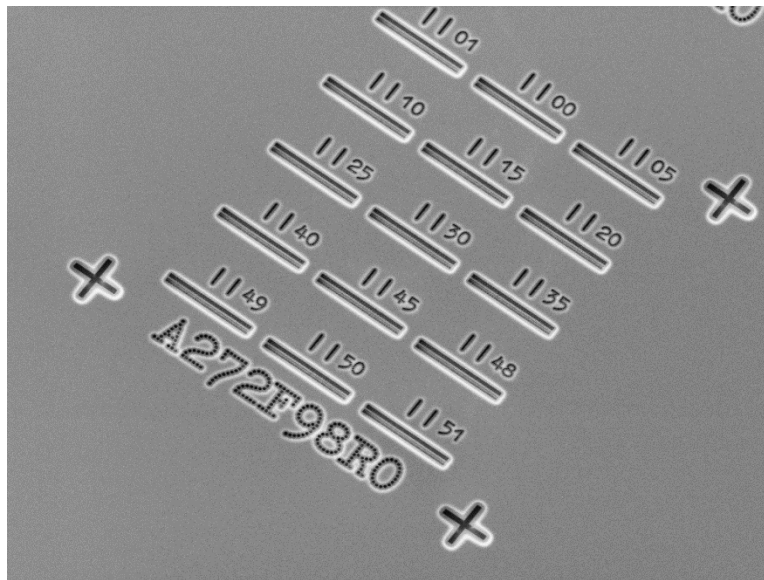


Figure 41 SEM of PCNB with fins in array layout

The EBL process starts from spin coating (4000 rpm, thickness 371 nm) of e-beam resist (ZEP 520A), followed by pre-baking at 180°C for 3 minutes, and afterwards e-beam exposure under accelerating voltage of 20 kV on the Nanometer Pattern Generation System (NPGS, by J. C. Nauty

Lithography Systems). The exposed pattern is then developed by Amyl Acetate under refrigeration temperature for 60s followed by a post-baking at temperatures heating up from 60 °C to 100 °C.

The PCNB pattern on the e-beam resist is then etched onto the Si₃N₄ layer by inductively coupled reactive ion etching (IPC-RIE) process, at gas flow rate ratio of SF₆: CHF₃: He = (1: 2.5: 2.77), with resulted aspect ratio of 5.3. A following isotropic IPC-RIE process with only SF₆ gas etches the Si substrate to create the suspension of the PCNB on Si₃N₄. The residues of e-beam resist are then dissolved in N-Methyl-2-pyrrolidone (NMP) solution heated up to 75 °C. The suspended thin fins are proved to be intact during this wet process, but the mostly used combination step of ultrasonication is completely prohibited. Instead, a final process of oxygen plasma ashing for 1 hour completely cleans up all the remains of e-beam resist.

4.3.2. Measurement and analysis

For the nanobeam cavity design without lateral fins, two different tapers are fabricated and compared on the same 1-dimensional (1-D) PC structure, with the taper profiles shown Figure 39(a). The resonance wavelength of the 1-D PC is determined by the photonic band diagram, as shown in Figure 42(a) where the air band (solid lines) and dielectric band (dashed lines) are plotted for 1-D PCs with different r/a ratios. For the target wavelength at 660 nm, $r/a=0.27$ is picked. The fabricated cavity resonance is then measured by optically pumping the Si₃N₄ cavity with a 450 nm laser to activate the defect states in the Si₃N₄. Shown in Figure 42(b) is the measurement result of cavities where a series of radius offset is scanned to achieve the target device dimension. For both tapers, the resonance wavelength shifts linearly, with Q-factor maximizes near the optimized radius. Taper02 has a closer match of radius profile to the optimized design and the optimized cavity resonance spectrum is shown Figure 42(c). The highest Q-factor obtained is 2.3×10^4 with full width at half maximum (FWHM) of 28pm. Shown in the inset is the full spectrum measured. Figure 42(d) shows the SEM image of taper02.

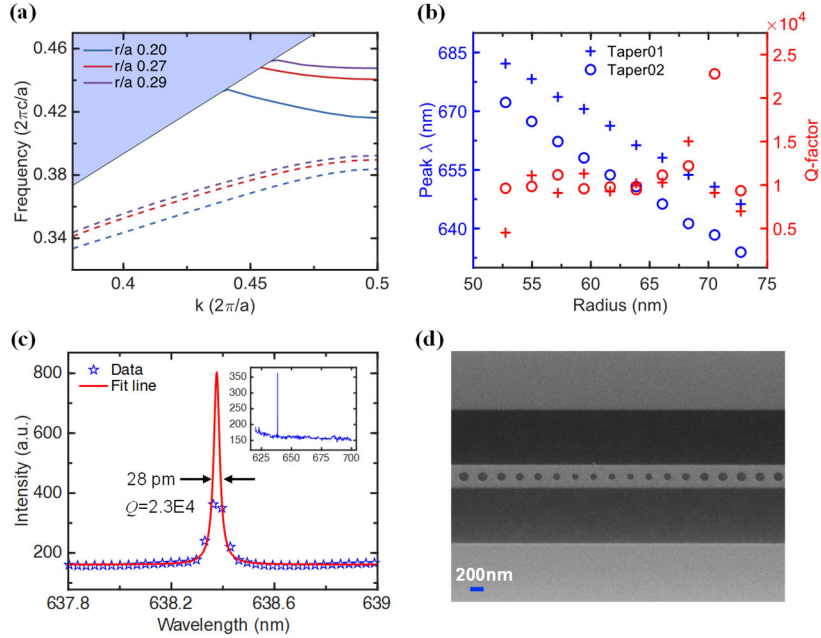


Figure 42 Photonic bands and characterization of nanobeam without fins

(a) Photonic band plot of 1-dimensional photonic crystal structure for r/a ratio of 0.2, 0.27, and 0.29, shaded region is the light cone of Si_3N_4 . (b) measured resonance wavelength and quality factor of two different taper structure at different radius offsets. (c) measured optical emission spectrum around the resonance peak and its Lorentzian fitting (inset is the full range spectrum) of one nanobeam cavity without fin that has the same radius as the cavity with fins. (d) top view SEM of the taper region on the suspended nanobeam cavity without fins.

After confirming the cavity radius taper profile, arrays of nanobeam cavities with fins are fabricated with fin alignment varies from the center point of 2 airholes (defined as $D=0$) to the center of each airhole (defined as $D=0.5a$). At $D=0$, the presence of fin rod has minimal influence on the distribution of the electromagnetic (E&M) field distribution compared to non-fin nanobeam cavity, as shown in the measured spectrum in Figure 43(a), where the measured $Q=2.46 \times 10^4$ and FWHM=26 pm. The true Q-factor can be higher since the resolution on our testing setup is limited to resolve finer peaks. This is close to the result shown in Figure 43 (c) and agrees well with the

simulation result described in the previous section. As the fin position shifts to the center of each airhole, the E&M field starts to couple to the lateral rod. As a result, the confinement (Q-factor) in the cavity is reduced and the resonance shifts to lower frequency (higher wavelength). The measured result is shown in Figure 43(b), where the red (blue) dashed line is the Q-factor (resonance wavelength) of the nanobeam cavity with the same dimension but without fins. It agrees well with the simulation result shown in Figure 43(c). The lower Q-factor in the measured result is due to both fabrication defects and measurement setup limit.

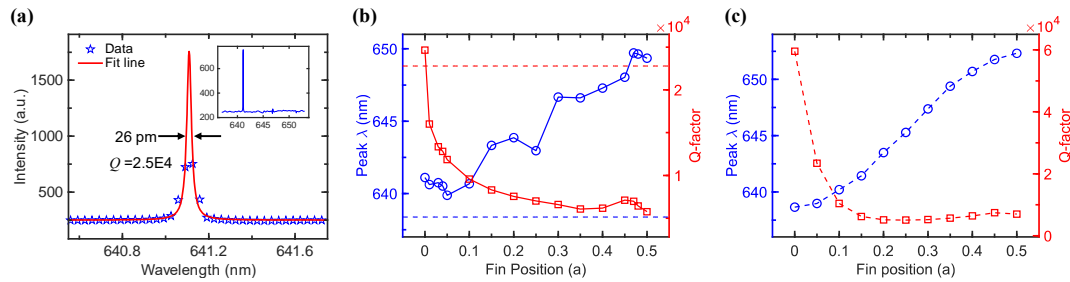


Figure 43 Characterization of nanobeam cavity with fins

(a) Measured optical emission spectrum around the resonance peak and its Lorentzian fitting of the nanobeam cavity with fins aligned to the center of 2 airholes, (b) measurement result of tuning of resonance wavelength and Q-factor as fin alignment position changes, where position $D=0$ is when fins are aligned to center of 2 airholes and position $D=0.5$ is when fins are aligned to airholes, (c) simulated result of tuning Q-factor and resonance wavelength by changing fin alignment position.

To find out the influence of fabrication offsets in the airhole radius, fin width, and more importantly, the resonance tuning capability of the fin-tuning nanobeam cavity array, another series of PCNBs is fabricated where the radius and fin width offsets are scanned. Shown in Figure 44(a) and Figure 44 (b) are the measured resonance wavelength and Q-factor on PCNBs with airhole radius and fin width varies independently. For both $D=0$ and $D=0.5a$ alignments, there is an optimized airhole radius and an optimized fin width. The variations of radius or fin width around the optimized design ($r = 64.5$ nm and $w = 24.2$ nm) cause the Q-factor and resonance wavelength

change gradually, which agrees with the numeric simulation results shown in Figure 44(c) and Figure 44(d) in general. The minor discrepancies may be related to the fabrication variations. For both radius and fin width that are 10 nm away from the optimized design value, the Q-factor drops to about half of the optimized Q-factor. It is worth mentioning that the range of wavelength tuning by fin position broadens for larger airhole radiuses and for wider fins. But the broader tuning range comes with a reduced Q-factor in both cases.

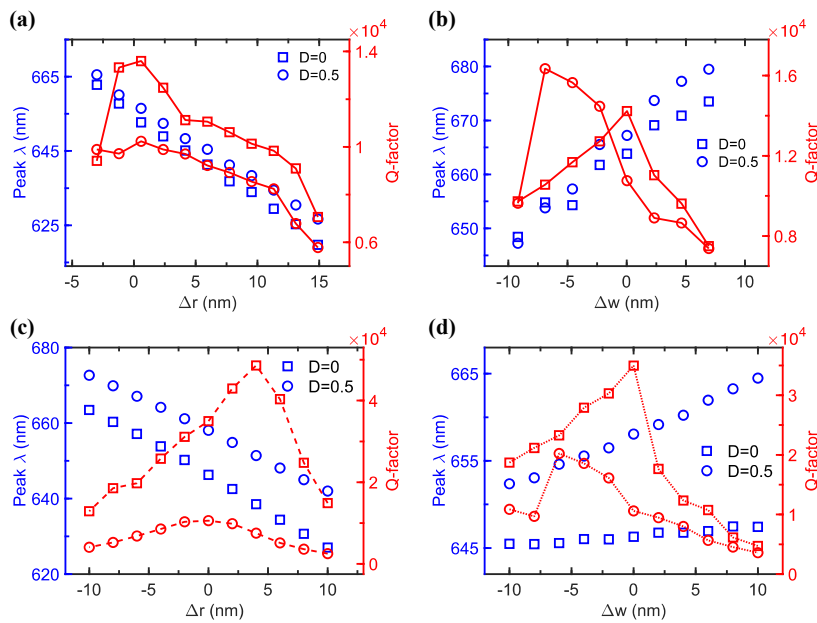


Figure 44 Influence of fin width and airhole radius

(a) Measured and (c) Simulated resonance wavelengths and Q-factors with different radius offsets; (b) Measured and (d) Simulated resonance wavelengths and Q-factors with different fin width offsets.

4.4 Summary

We designed, fabricated, and measured arrays of nanobeam cavity with lateral fins where the fin alignment position is tuned to control the resonance Q-factor and wavelength. The lateral

fins can provide mechanical support, act as thermal conduction channels, and enable carrier injection to the suspended nanobeam cavity. These low mode-volume, high Q-factor nanobeam cavities are ideal candidates for novel lasers, light emitting diodes, optical modulators, filters, and sensors. The nanobeam cavity can also be applied on different materials and can be integrated with new photonic/electronic on-chip platforms for high speed, low power consumption applications.

It is worth mentioning that the proposed structure can be designed to have extremely high Q factors or moderate Q factors depending on the application requirements. The impact of the lateral fins may be very small (2%) to the nanobeam cavity Q factors. So extremely high Q factors can be achieved. This could be useful for high-speed modulators or high sensitivity sensors. On the other hand, moderate Q factors are desirable for nanobeam lasers if we consider trade-offs in modulation speed and energy cost.

CHAPTER 5.

PHOTONIC CRYSTAL SLAB METALENS

5.1 Introduction of transmissive photonic crystal metalens

Nanoscale metamaterial have drawn increasing attention for the last two decades for its broadband, highly efficient capabilities of phase modulation by a flat medium. The research on the flat optics or meta surfaces open new capability for a great variety of applications in beam manipulations such as focusing/imaging [104], formation of vortex beam [105] and patterned spot projection [106]. So far, the common metamaterial are the dielectric pillar structures placed on the applicable substrate with tailored shapes, separation rotation, and placement to bend the transmitted light in the desired way. The mechanism of the localized scattering in these structures often requires the material thickness to be at micrometer scale to provide long enough light paths and to achieve a complete 2π phase transition range. It thus hinders the full adoption of the technology in commercialized product which has higher durability requirements. We propose here an amorphous silicon photonic crystal slab (PCS) metalens structure with full 2π phase modulation, high transmission efficiency and broadband operation centered at 940nm. The design of a focusing PCS Metalens is also verified with COMSOL and 3-dimensional large area finite-difference time-domain (FDTD) method.

5.2 Metalens flat optics constructed by meta-atoms

Metalens is a new a type of diffractive lens that has a subwavelength quasiperiodic structure and can induce phase change of light, just like a conventional lens, but with more functionality. As the terminology indicates, metalens consists of individual elements that are in perturbed forms of one building block configuration, which is called meta-atom. The form of the

meta-atoms is flexible, including nano-fins, nano-rods, nano-disk and so on. Thanks to the reduced thickness of the optical elements, metalens is an ideal candidate to replace the traditional bulk optics with its binary structure, CMOS compatibility [107,108], high-numerical aperture capabilities [109-113], chromatic correction [114-117], tunability [118,119], and polarization selectivity [120-122].

To design metalens for light detection and ranging (LiDAR) applications 940 nm, our choice material is amorphous silicon for its high refractive index and cost effectiveness. Figure 45 shows the refractive index n [123,124] in visible and near IR range. At 940 nm, we use refractive indices 1.68 for amorphous silicon (a-Si) for the meta-atoms, and 1.535 for glass substrate.

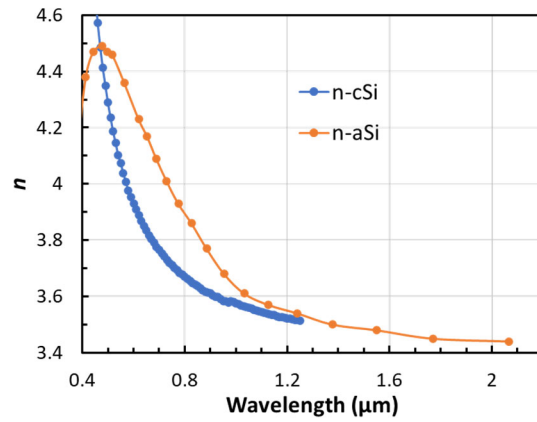


Figure 45 Refractive indices of crystal (c-Si) and amorphous silicon (a-Si).

5.2.1. Polarization dependent meta-atom

Polarization dependent meta-atoms relies on in-plane angle rotation to achieve transmission phase variation. For localized meta-atom, the geometric phase that meta-atom produces for transmission for rotation angle α is $\Phi_{geo} = 2\alpha$, while for non-localized meta-atom, the phase could be $\Phi_{geo} = 4\alpha$ or $\Phi_{geo} = -4\alpha$ [125]. Polarization dependency of these meta-atoms

will convert the propagation of light from left circular polarization (LCP) to right circular polarization (RCP).

Shown in Figure 46(a) is the 3D schematic of the nano-fin meta-atom with periodicity $S=530$ nm, height $H=510$ nm, fin width $W=130$ nm, and fin length $L=435$ nm. The transmission efficiency and phase with variation of rotational angle are plotted in Figure 46(b).

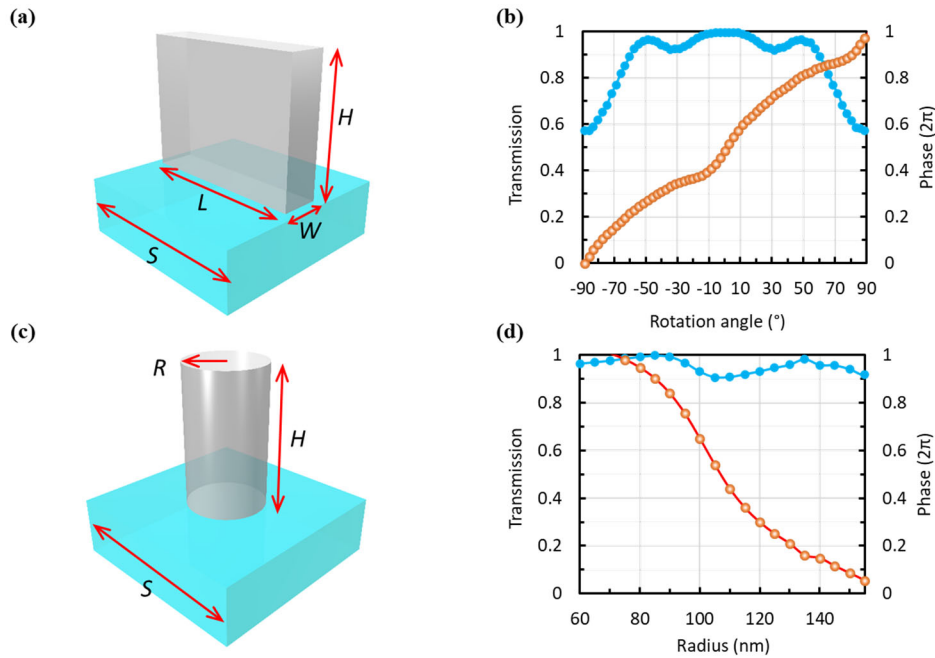


Figure 46 Schematics and transmission phase of meta-atoms

(a) and (c) Schematic illustration of meta-atoms of nanofin and nanorod respectively, (b) and (d) corresponding transmission coefficient and phase.

5.2.2. Polarization independent meta-atom

The polarization independency requires the geometry to preserve azimuthal symmetry; thus, the choice of structure is naturally a cylindrical post. Shown in Figure 46(c) is the schematics

of the nano-rod meta-atom with periodicity $S=380$ nm, rod height $H=510$ nm. The transmission efficiency and phase with variation of radius from 60 nm to 150 nm are plotted in Figure 46(d)

5.2.3. Construction of phase array for focusing lens

For focusing lens, the numerical aperture NA , the lens size (diameter) L , and the focal length follows the lens equation:

$$f = \frac{L/2}{NA} \sqrt{1 - NA^2}$$

At any position (x, y) on the lens plane, the transmitted light should carry an extra phase $\phi(x, y)$ in hyperboloid form as shown in Figure 47(a) so that the light path length from every point to the focal point is a constant,

$$\phi(x, y) = \frac{2\pi}{\lambda} (\sqrt{x^2 + y^2 + f^2} - f)$$

where λ is the working wavelength. Figure 47(b) shows the schematic illustration of light focusing effect upon transmitting through the metalens with the above phase distribution.

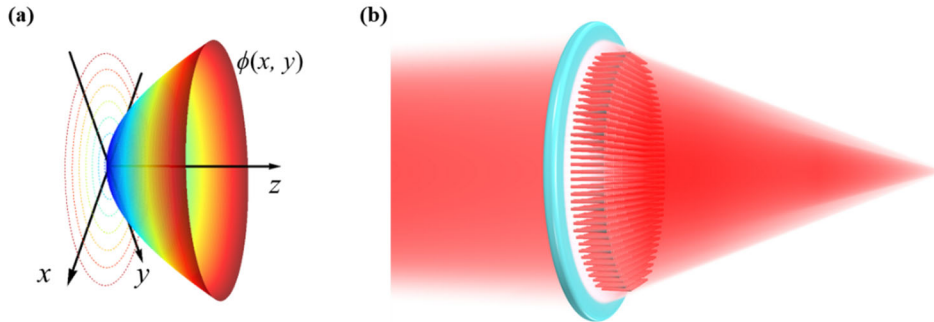


Figure 47 Refractive indices of crystal and amorphous silicon

5.2.4. Focusing lens lattice choice

Since our metalens is working in the localized regime without any resonance, the choice of lattice of the meta-atom is flexible and can take quasi-periodic arrangement. Shown in Figure 48 is a sketch of the in-plane distribution of nano-fin and nano-rod with square lattice and circular lattice.

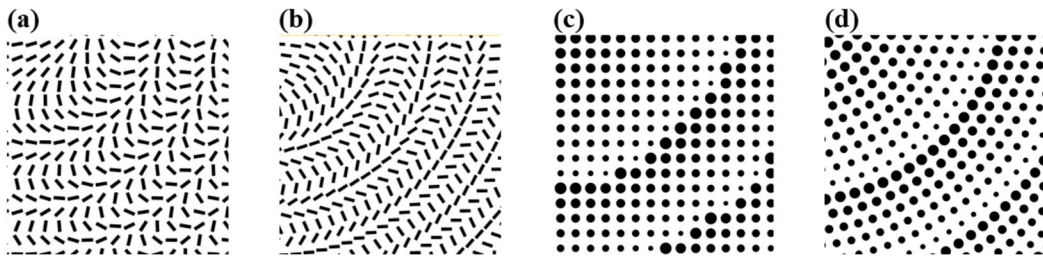


Figure 48 Meta-atoms arranged in different lattices

Nano-fins in (a) square lattice (SL), and (b) circular lattice (CL). Nano-rods in (c) square lattice, and (d) circular lattice.

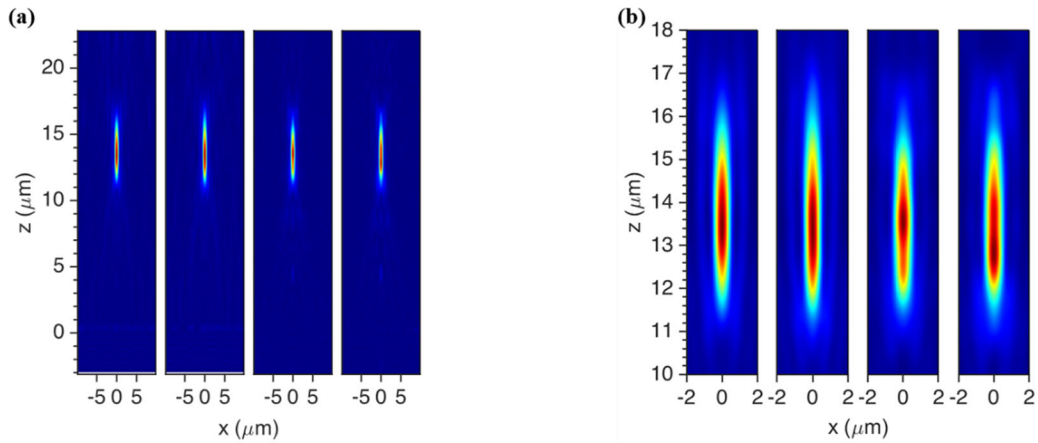


Figure 49 Distribution of $|E|^2$ on x - z plane for plane wave transmission

(a) Distribution map of $|E|^2$ over full range of $20 \times 20 \times 23 \mu\text{m}^3$ of metalens of (from left to right) nano-fins in SL, CL, and nano-rods in SL and CL. (b) is the zoom-in of (a) over the focusing region.

We constructed these 4 metalenses with a-Si deposition on glass. The focusing effect is shown in Figure 49(a) by simulation with the FDTD tool Tidy3D [26]. The simulated lens size is $20\mu\text{m}$ in x - y direction and $NA=0.6$. In all cases the focal length is at $13.6\mu\text{m}$ as the lens equation above predicted. It shows that the lattice choice does not affect the focusing in significant way.

5.2.5. Spot size dependence on NA

We also investigated the focusing capabilities of nano-rod metalens at various NA from 0.1 to 0.9. The field amplitude of each NA is plotted in Figure 50. We noticed that at lower NA, the focusing power of the lens could be an ideal candidate for emission angle control for laser sources such as VCSEL in the LiDAR applications where divergence of the laser is still an issue for effective collection of reflected signals.

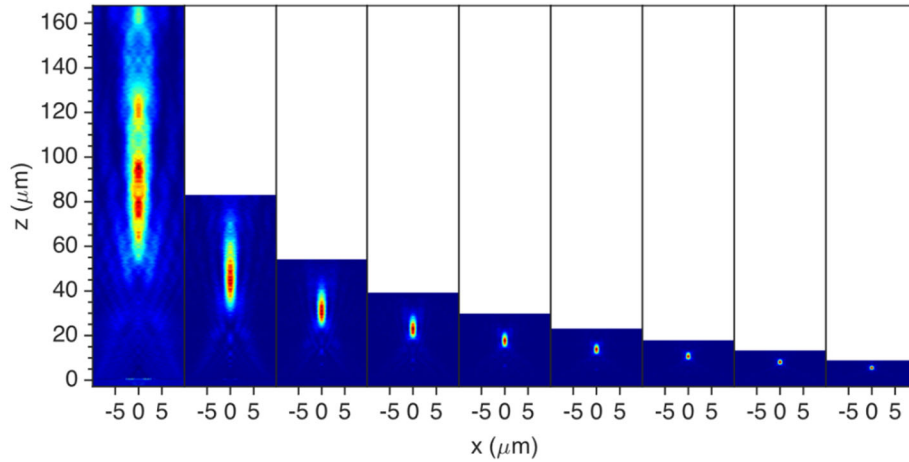


Figure 50 Distribution of $|\mathbf{E}|^2$ on x - z plane for at $NA = 0.1\sim 0.9$

Shown in Figure 51 are the extracted focal length and spot size of the lenses with different NA discussed above. All spot sizes are smaller than the diffraction limited resolution, which is one of the attractions of the flat optics.

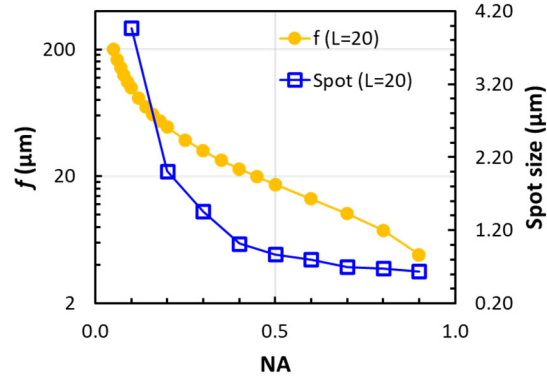


Figure 51 Focal length and spot size for at $NA = 0.1\sim 0.9$

5.2.6. Broad-band operation

We optimized the nano-rod metalens by sweeping the thickness and lattice constant of the meta-atom in the simulation. At lattice constant $S=380$ nm and rod height $H=440$ nm, the meta-atom has the best transmission efficiency over 95% and is also capable of operate at very wide spectral range from 740 nm to 1140 nm. Shown in Figure 52(a) and (b) are the transmission intensity and phase map (unit in π) of the nano-rod meta-atom over r/a ratio from 0.05 to 0.49 and wavelength from 800 nm to 1080 nm. If we focus on a single wavelength at 940 nm, the transmission intensity and phase line over the specified r/a ratio range is shown in Figure 52(c). The numerical simulation results in Figure 52 indicate that the phase line that covers a complete 2π range, starting from the blue zone at small r/a ratios in Figure 52(b), crossing the red zone, reaching to the thin blue strip zone, with the variation of r/a ratio of the meta-atom is consistent within the wavelength range. This means that the focusing metalens constructed with this meta-atom could operate in a broadband range without significant distortion in the focusing capability or compromise in the transmission efficiency.

To verify our prediction from the meta-atom, we built a metalens with the parameters of this nano-rod meta-atom, which has an in-plane phase distribution shown in Figure 53 as described in the previous section.

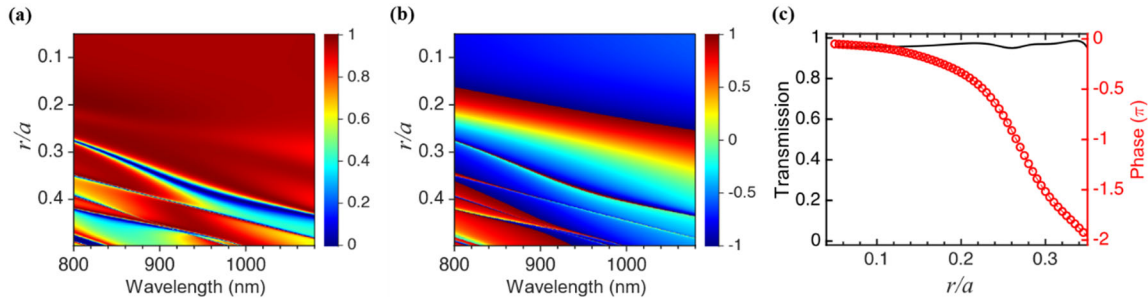


Figure 52 Transmission intensity and phase of nano-rod metalens

(a) Transmission intensity map and (b) transmission phase map over r/a ratio from 0.05 to 0.49 and spectrum from 800 nm to 1080 nm. (c) transmission intensity and phase line at 940 nm.

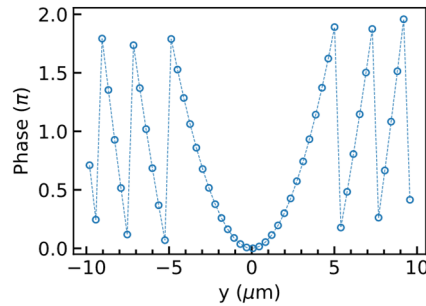


Figure 53 In-plane phase distribution of the metalens built from the nano-rod metalens

The numerical simulation results of the nano-rod metalens by Tidy3D is shown in Figure 54. It clearly verifies the prediction from the phase map of the nano-rod meta-atom. Our metalens can operate withing broadband span of 400 nm centered at 940 nm. The focal length change displayed in the result is a direct consequence of the hyperboloid phase relation of focusing lens.

Further discussion on the correction of this chromatic aberration is needed in the future research efforts.

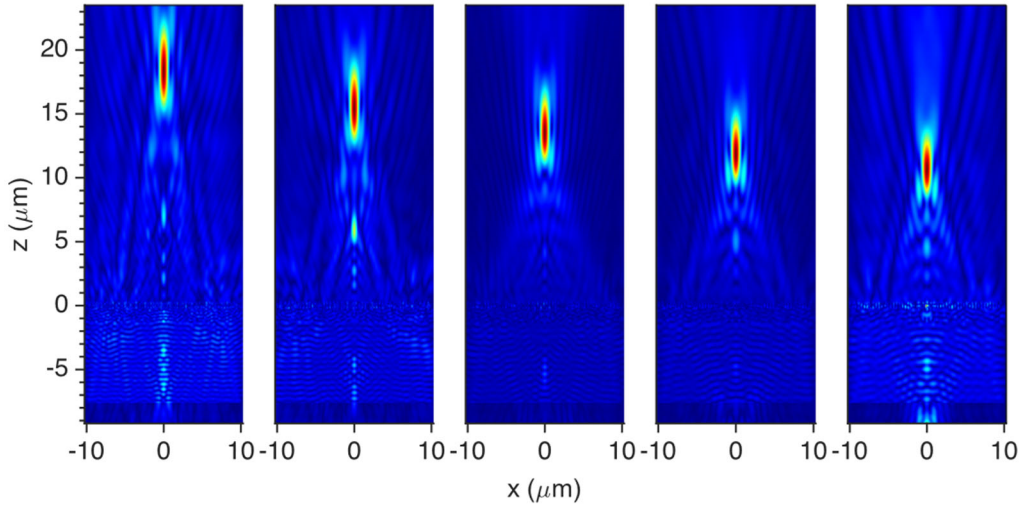


Figure 54 Focusing effect of the metalens built from nano-rod meta-atoms.

Distribution map of $|\mathbf{E}|^2$ over full range of $20 \times 20 \times 23 \mu\text{m}^3$ of metalens for working wavelength (from left to right) at 740 nm, 840 nm, 940 nm, 1040 nm and 1140 nm.

5.3 Transmissive 2π phase on photonic crystal slabs

The metalens structure discussed above is promising for applications in highly efficient, broadband flat optics. But the robustness of the isolated posts and the relatively large thickness pose a strong challenge to the full implementation of the structure in the practical commercialized devices. We look alternatively at the thin-film technology, particularly the photonic crystal slab (PCS) structure which can solve the issues inherently.

The fundamental principle of the transmission phase control by PCS is the non-localized resonance (guided mode). This could potentially compromise the utilization of PCS for construction of large area metalens. We recall that for meta-atoms the phase control mechanism is localized

scattering, which means the interaction between the individual meta-atom won't be disturbed in principle when composed into the large area lens device. For the PCS resonance, the interaction between the neighboring lattices could still be considered as quasi-periodic when the lattice constant is fixed and the airhole radius varies in small amount which could be characterized as a small perturbation. In this case, when the perturbation is within 1% the resonance frequency and strength are still constant.

5.3.1. Coupled mode theory and formation of 2π phase continuity

The PCS guided resonance modes can be quantitatively analyzed by the coupled mode theory which establishes the temporal relation of transmittance, reflectance, and the resonant modes that exhibits Fano line shape in the spectrum [126]. Our previous investigation on the PCS modes has also proposed the condition for reflective 2π phase formation [127]. Similar procedures can be taken to derive conditions for transmissive 2π phase formation. The condition for having a transmissive 2π phase continuity is that the PC transmission coupling strength should be larger than the background transmission. This condition is satisfied for modes that degenerate near the edge of a broad high transmission band.

We investigated the amorphous silicon PCS-on-glass structure and found the degenerate mode at slab thickness $t = 160$ nm, $a = 500$ nm and $r/a > 0.4$ for working wavelength at 940 nm. It is then possible to construct a various phase plate by varying the air hole radius (thus r/a ratio) only to achieve the 2π phase line. It was discovered also that further improvements on transmission efficiency can be realized by changing both the air hole radius and the lattice constant. Close to 100% transmission can be achieved for the most part of the designs, as shown in (c). More details will be presented in the conference on both theory and design.

Showing in Figure 55 is a schematic illustration of a PCS with 4 coupling ports. The transmission of the PCS can be written as

$$S_{21}(\omega) = C_{21}(\omega) + h(\omega)d_2^*d_1$$

where S_{21} is the total transmission, C_{21} is the background transmission, $h(\omega)$ is the resonance line shape and d_1 and d_2 represent the PC coupling strength to the background wave. The line shape of the resonance can be expressed as

$$h(\omega) = \frac{1}{j(\omega - \omega_0) + \frac{\omega_0}{2Q}}$$

The background transmission $|C_{21}|^2$ is calculated on the slab using effective refractive index:

$$\varepsilon_{avg} = \left(\frac{a^2 - \pi r^2}{a^2}\right) \varepsilon_{Si} + \left(\frac{\pi r^2}{a^2}\right) \varepsilon_{air}$$

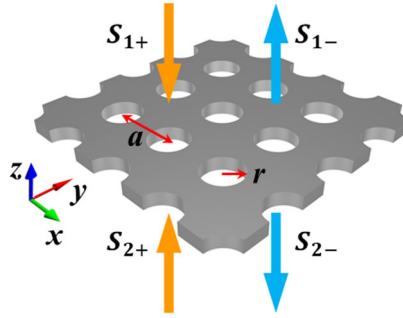


Figure 55 3D sketch of the coupling ports on a PCS.

Coupling ports S_1 and S_2 for a PCS of lattice constant a and airhole radius r , the + and - signs are for input and output.

For a transmission guided resonance mode, the condition of forming a continuous 2π phase transition in spectrum is

$$|d_1 d_2| > \frac{|t|}{|h(\omega)|}$$

This is an apparent conclusion which we will prove later in the degenerate mode discussion.

5.3.2. Degenerate PC mode and formation of 2π transmission phase

Most of the PC mode displays a Fano line shape where the intensity of the transmission or reflection goes to the maximum and drop to the minimum or the other way in the spectrum. The origin of this rapid change in the intensity are two folds: firstly, the intensity of such line shape is the coupled intensity of the resonance and the background wave; secondly, the resonance phase spectrum carries a phase discontinuity of π , which means that the coupling between the guided resonance and the background experiences a complete in-phases to complete out-phase transition when the frequency/wavelength changes near the resonance mode.

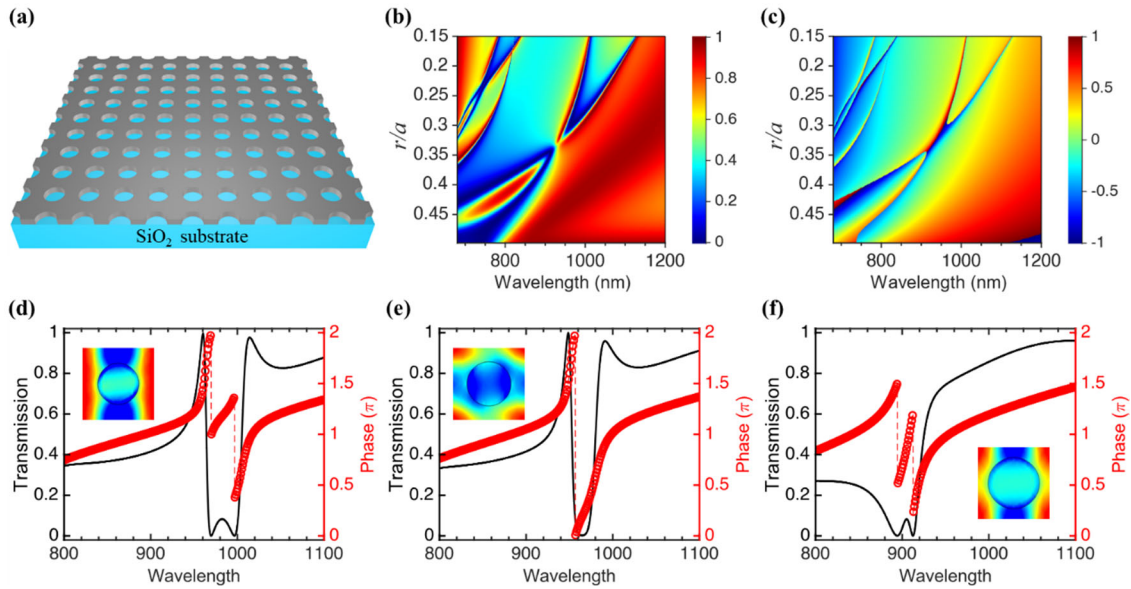


Figure 56 Degenerate mode near the high transmission band edge .

(a) Schematic illustration of the Si PCS on glass with lattice constant $a=390\text{nm}$ and slab thickness of 185nm . (b) transmission intensity map and (c) transmission phase map over wavelength and r/a ratio. (d), (e) and (f) are the transmission intensity and phase spectra of the PCS at r/a ratio of 0.3, 0.32 and 0.36 respectively. The insets in (d), (e) and (f) are the inplane field component distributions of $|E_x|^2$ in the PCS layer for the PC mode.

However, there are PC modes that could generate a continuous phase through the resonance mode. We found that for Si PCS on glass as shown in Figure 56(a) with lattice constant $a=390\text{nm}$, slab thickness $t=185\text{nm}$, and r/a ratio sweeping from 0.15 to 0.49, there are 2 PC mode that degenerate near r/a ratio of 0.35. As shown in the transmission intensity map Figure 56 (b) and transmission phase map (c), two PC modes degenerate when r/a ratio is in between 0.3 and 0.35. The degeneracy merges the phase discontinuity from the two PC modes as shown in Figure 56 (d), (e) and (f). We can also see in the inset plots of the $|E_x|^2$ component in the PCS layer, the degeneracy squeezes the field into the high index media such that the phase is now continuous in one uniform media.

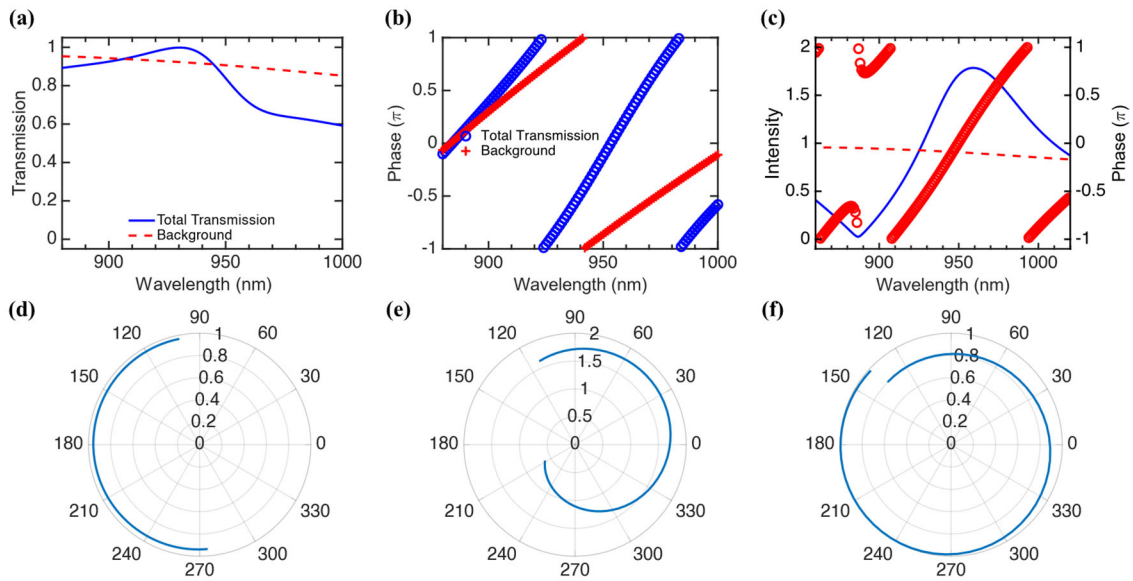


Figure 57 Coupled mode theory analysis of the degenerate mode

(a) Total and background transmission intensity and (b) transmission phase of the degenerate mode. (c) PC resonance coupling intensity and phase. (d), (e) and (f) are the polar plots of background transmission, resonance coupling strength and total transmission of the degenerate mode.

Applying the coupled mode theory analysis on the degenerate mode shows how the PC resonance coupling and the background transmission contribute to the formation of the 2π phase continuity respectively. Shown in Figure 57 (a) and (b) are the intensity and phase of the total and background transmission respectively. The 2π phase continuity condition is shown in Figure 57 (c), when the PC resonance coupling strength is larger than the background transmission around the mode in-between 920nm and 1020nm, the total transmission phase is continuous as shown in (b). Furthermore, within this range, we plot the complex quantities of background transmission, PC resonance coupling strength and the total transmission in (d), (e) and (f) respectively, and see that the phase continuity of the total transmission is contributed by the background and PC coupling together.

5.3.3. Construction of PC metalens

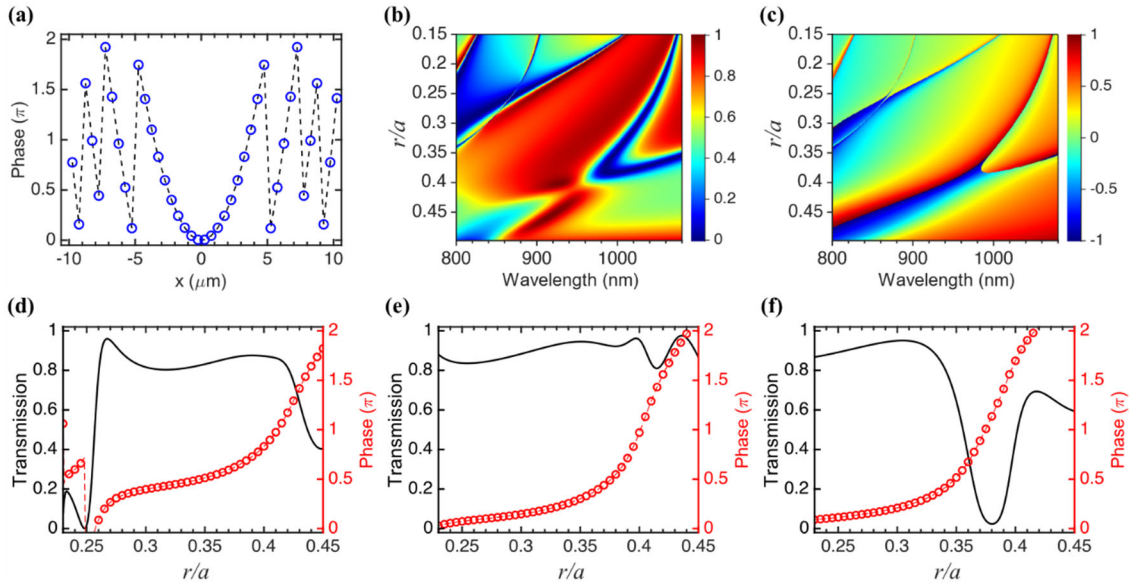


Figure 58 Optimized PCS continuous phase mode .

(a) Phase distribution of a focusing lens composed of PCS with lattice constant $a=500\text{nm}$ and slab thickness of 165nm . (b) transmission intensity map and (c) transmission phase map over wavelength and r/a ratio. (d), (e) and (f) are the transmittance and transmissive phase line over r/a ratio range (0.25 to 0.45) for incident wavelength at 880nm, 940nm and 980nm respectively.

The degenerate mode discussed above can be further optimized to have a broad high transmission band with phase continuity. Shown in Figure 58 (b) and (c) are the transmittance map and transmissive phase map of a PCS with lattice constant $a=500\text{nm}$ and slab thickness of 165nm over wavelength range of 800nm to 1080nm , and r/a ratio range of 0.15 to 0.49 . This PCS has the broad band transmissive phase response over 100nm from 880nm to 980nm . (d), (e) and (f) are the transmittance and transmissive phase line over r/a ratio range (0.25 to 0.45) for incident wavelength at 880nm , 940nm and 980nm respectively. All phase lines cover the full 2π range with variations in transmittance. We construct a focusing lens with in-plane phase distribution as shown in Figure 58 (a). The broadband focusing effect of this metalens is shown in Figure 59 for incident wavelengths from 740 nm to 940 nm with 10nm step size.

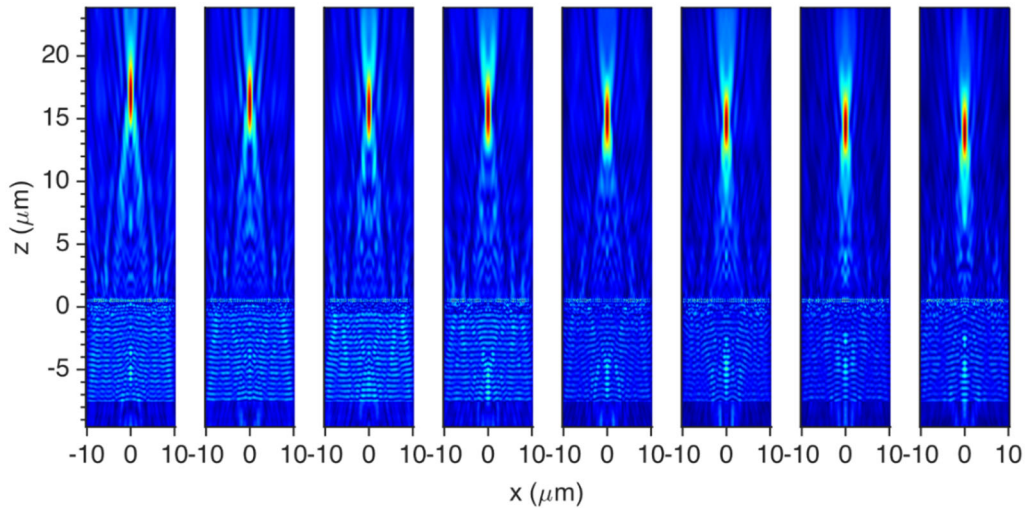


Figure 59 Focusing effect of the metalens built from PCS.

Distribution map of $|\mathbf{E}|^2$ over full range of $20 \times 20 \times 23 \mu\text{m}^3$ of metalens for working wavelength (from left to right) at 740 nm to 940 nm with 10nm step size.

5.3.4. Conclusion: PCS versus meta-atoms

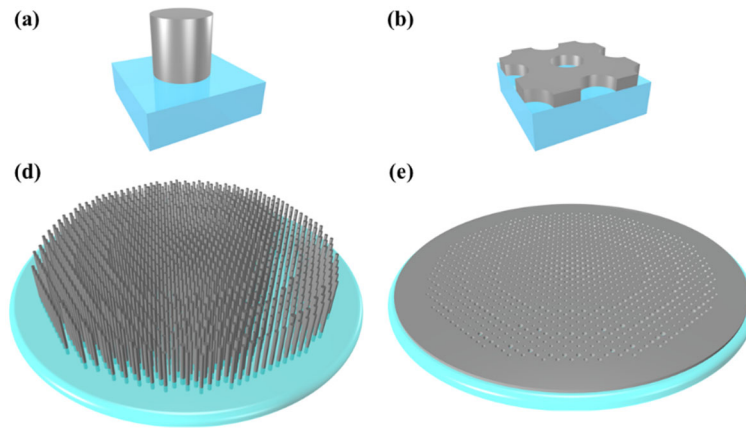


Figure 60 3D sketch of metalens composed of meta-atom and PCS.

(a) Meta-atom and (c) metalens composed of meta-atom; (b) PCS and (d) metalens composed of PCS.

The discussion above reveals that both meta-atoms and PCS are capable of transmission phase control with high efficiency. Shown in Figure 60 are the 3D schematic illustration of the metalens composed of meta-atoms and PCS. We compare the mechanism and numerical performance of both technologies in Table 5. It shows that meta-atom is performing better in spot size, transmission efficiency and operation bandwidth. However, PCS is advantageous in the layer thickness, focal length and depth of focus (DOF). Considering the application scenarios of metalens, thin film technology of PCS would be preferred than the deposited isolated toll meta-atoms.

Table 5 Comparison of meta-atom and PC candidacy for metalens

	Scattering type	Height	Focal length	DOF	Spot size	Trans. efficiency	Operation band
Meta atom	Localized	440nm	13.51 μ m	3.43 μ m	0.65 μ m	82.3%	>400nm with C.A.
Photonic crystal	Non-localized	160nm	13.83 μ m	3.67 μ m	0.75 μ m	70.8%	280nm with C.A.

5.4 Reflective 2π phase transition

Photonic crystal also is widely used in reflection applications such as sensing and imaging. In these applications, conventionally the reflection PC modes are implemented spectrally. If a reflective PCS can provide a continuous 2π phase transition, it then could lift the demand of spectral information for PC application with a monotonic phase line that is tunable with dimension index change.

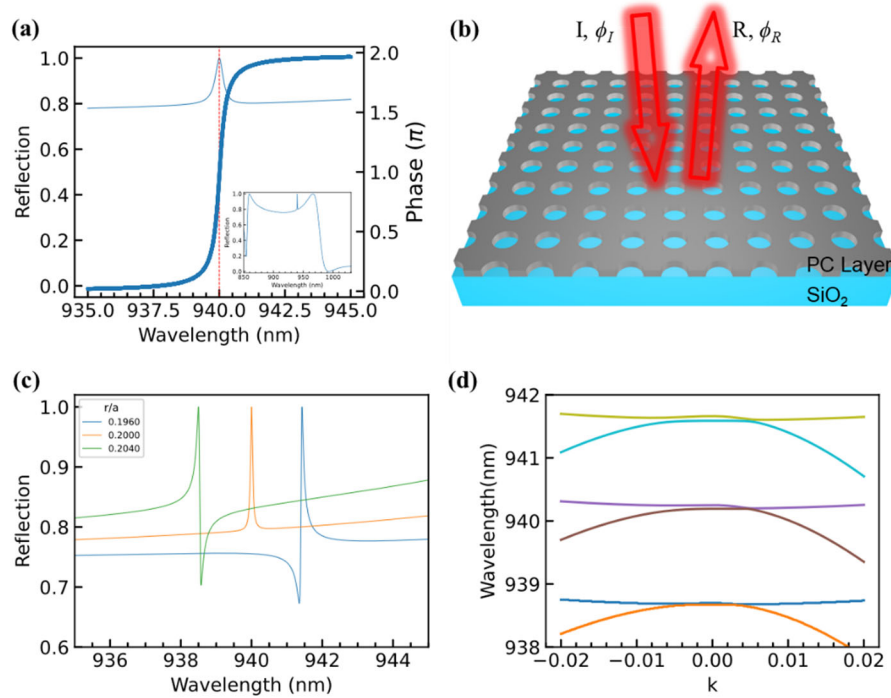


Figure 61 PCS reflective 2π mode.

(a) Reflection spectrum and phase of the designed photonic 2π mode crystal at r/a ratio of 0.25. The inset is the full range spectrum of reflection. (b) Schematic illustration of silicon photonic crystal on glass. (c) Reflection spectrum of 3 photonic crystal with different symmetry. (d) Photonic band diagram of the modes in (c).

5.4.1. Continuous reflection 2π phase on photonic crystal slabs

Our investigation on the PCS modes has proposed the condition for reflective 2π phase formation [127]. As shown in the sketch image in Figure 61 (b), for a PCS on glass with slab thickness 300nm, lattice constant 990nm and r/a ratio 0.25, the reflection phase is defined as the difference of the reflected field phase ϕ_r and the incident field phase ϕ_i . This structure has a high reflection band as the inset shows in Figure 61 (a). There is a PC mode on this band that has 2π phase transition in the spectrum as shown in (a). More interestingly, the line shape of this PC mode changes from Fano-like to Lorentzian-like and back to Fano-like with the line shape symmetry flipped when r/a ratio deviates from 0.25 as shown in (c). This line shape change is connected to the photonic band structures shown in (d).

The Lorentzian line shape is particularly interesting in that it enhances the broadband high reflection to nearly 100% while also displays a 2π phase transition. This means that in applications it is guaranteed to have high reflection with no rapid intensity change compared to the common Fano-like PC modes.

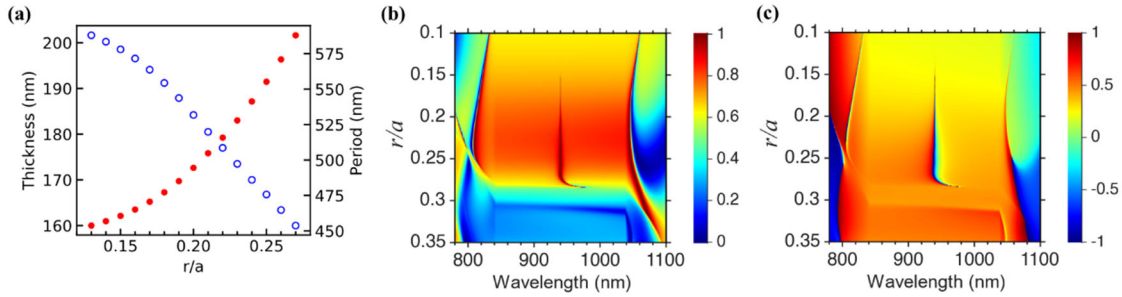


Figure 62 2π reflection phase on PCS with defferent parameters .

(a) Slab thickness and lattice constant (period) combination of the reflection 2π phase mode.(b) transmission intensity and (c) phase map of the reflection 2π phase mode.

It is also possible to tune the line width of this reflective 2π phase mode by varying the combination of the lattice constant, r/a ratio and the slab thickness as shown in Figure 62 (a). The intensity and phase map of these combinations are shown in Figure 62 (b) and (c).

5.4.2. Tunable sensitivity

Different combinations of parameters of this PC mode also give tunable linewidth, Q-factor, enhancement factor and index change needed for a 2π phase shift.

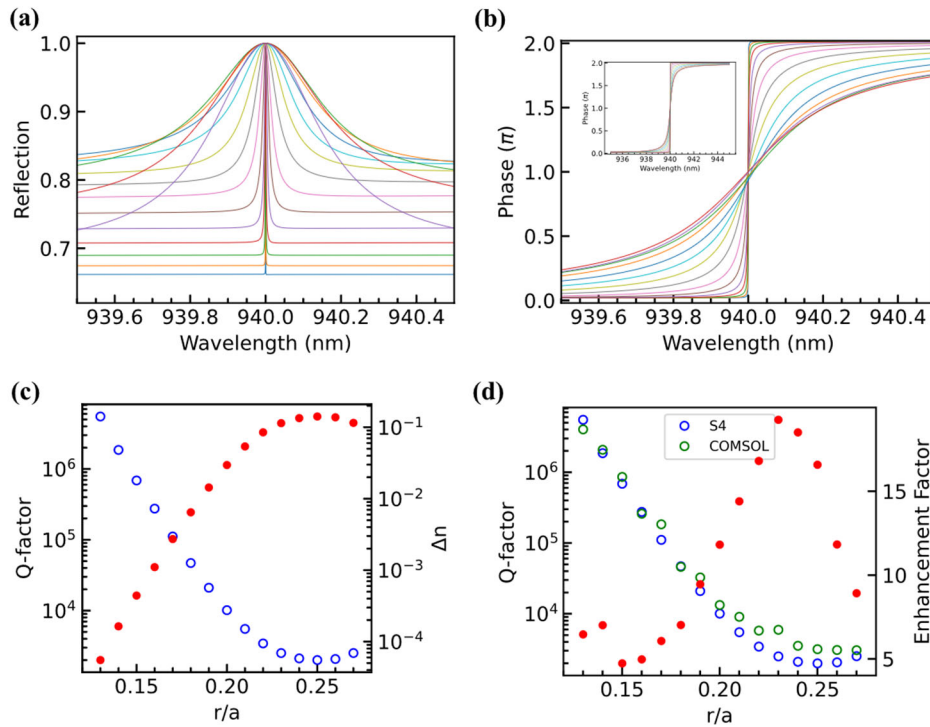


Figure 63 Tunability of the reflective 2π phase PCS mode .

(a) Linewidth tuning, (b) phase transition tuning, (c) Q-factor and 2π phase index tuning, and (d) enhancement factor tuning.

Shown in Figure 63 (a) and (b) are the reflection intensity and phase spectra of the 2π reflection PCS mode with different parameters. Q-factor gets larger as r/a ratio becomes smaller, which is generally true for PC modes, as shown in (c), while the refractive index needed to bring a

2π phase transition becomes smaller. It means that the index sensitivity of the PC mode increases, to as high as $2\pi/10^{-4}$. The findings are also consistent with our coupled mode analysis as shown in Figure 63 (d).

In conclusion, the reflective 2π phase mode signifies in not only the enhanced reflection with a monotonic phase line, but also the flexibility in the sensitivity design. These features enable us to design monochromatic sensors with high sensitivity.

CHAPTER 6.

CONCLUSION REMARKS AND FUTURE RESEARCH

6.1 Conclusion

We have investigated the application of PC structure on laser cavity, optical sensor and optical element as metalens. The unique light-matter interaction of PC modes has opened the door for even more possibilities for other optical devices that has higher power, lower energy cost, higher efficiency and higher speed.

We found that the application of PC in sensors works along with the choice of material of the PC layer, either to utilize the high thermo-optical effect, or the bioresorbability of the material. The limitation of this application is in the optical path of PC measurement in free space where light absorption and incident angle are the challenges for a full implementation of the device out of laboratories.

We found that the application of PC as the laser cavity is of great potential on different PC configuration such as 1D nanobeam cavity and hetero-PC cavity. It will become the next generation optical cavity for high power, high speed and low energy cost lasers. It also has the potential to integrate with novel gain materials such as 2D material with low threshold exciton emission.

We also found that the application of PC in metalens is promising since it is thin film technology compared to the well-studied meta-atom approach. It could be favored by the industry for the robustness and performance in flat optics applications.

6.2 Future work

The investigation in the PC applications in this dissertation, though as broad as it could possibly be, would be more complete if the application of nanobeam cavity on GaAs laser device

could be verified and if the PCS metalens could be fabricated and demonstrated. The nanobeam PC cavity is promising in the tunability of the Q-factor to achieve the low energy cost and high speed. The PCS metalens is a competitor of the meta-atom approach that is drawing overwhelming attention in the field of flat optics.

LIST OF PUBLICATIONS

- [1]. **Liu, Z.**, Pan, M., Liu, A., Sampsell, M., Kelly, G., Liu, J., Zhou, W. "Photonic crystal slab metalens", (2022, In submission)
- [2]. **Liu, Z.**, Chen, Y., Ge, X. & Zhou, W. Photonic crystal nanobeam cavities with lateral fins, *Nanophotonics*, 10, 3889-3894. (2021) <https://doi.org/10.1515/nanoph-2021-0361>
- [3]. Bai, W., Iric, M., **Liu, Z.**, Luan, H., Franklin, D., Nandoliya, K., Guo, H., Zang, H., Weng, Y., Lu, D. *et al.* Bioresorbable Multilayer Photonic Cavities as Temporary Implants for Tether-Free Measurements of Regional Tissue Temperatures. *BME Frontiers* **2021**, 1-14. (2021). <https://doi.org/10.34133/2021/8653218>
- [4]. Shin, J., **Liu, Z.**, Bai, W., Liu, Y., Yan, Y., Xue, Y., Kandela, I., Pezhouh, M., MacEwan, M. R., Huang, Y. *et al.* Bioresorbable optical sensor systems for monitoring of intracranial pressure and temperature. *Sci Adv* **5**, eaaw1899. (2019). <https://doi.org/10.1126/sciadv.aaw1899>
- [5]. Jayanand, K., Saenz, A., Keylyuk, S., Davydov, A., Karapetrov, G., **Liu, Z.**, Zhou, W., Kaul, A. "Optically-induced quantum transitions in direct-probed mesoscopic 2H-NbSe₂ for prototypical bolometers", *npj 2D Materials and Applications*. (2022, Accepted)
- [6]. Pan, M., **Liu, Z.**, Kalapala, A. R. K., Chen, Y., Sun, Y. & Zhou, W. Complete 2π Phase Control by Photonic Crystal Slabs. *Optics Express* 29. (2021). <https://doi.org/10.1364/OE.440687>
- [7]. Biswas, P., Zhang, C., Chen, Y., **Liu, Z.**, Vaziri, S., Zhou, W. & Sun, Y. A Portable Micro-Gas Chromatography with Integrated Photonic Crystal Slab Sensors on Chip. *Biosensors* **11**. (2021). <https://doi.org/10.3390/bios11090326>
- [8]. Reuterskiöld Hedlund, C., Martins De Pina, J., Kalapala, A., **Liu, Z.**, Zhou, W. & Hammar, M. Buried InP/Airhole Photonic-Crystal Surface-Emitting Lasers. *physica status solidi (a)* **218**. (2020). <https://doi.org/10.1002/pssa.202000416>
- [9]. Bai, W., Shin, J., Fu, R., Kandela, I., Lu, D., Ni, X., Park, Y., **Liu, Z.**, Hang, T., Wu, D. *et al.* Bioresorbable photonic devices for the spectroscopic characterization of physiological status

- and neural activity. *Nat Biomed Eng* **3**, 644-654. (2019). <https://doi.org/10.1038/s41551-019-0435-y>
- [10]. Bai, W., Yang, H., Ma, Y., Chen, H., Shin, J., Liu, Y., Yang, Q., Kandela, I., **Liu, Z.**, Kang, S. K. *et al.* Flexible Transient Optical Waveguides and Surface-Wave Biosensors Constructed from Monocrystalline Silicon. *Adv Mater* **30**, e1801584. (2018). <https://doi.org/10.1002/adma.201801584>
- [11]. **Liu, Z.**, Pan, M, Liu, J, & Zhou, W, “Photonic crystal slab metalens”. 2022 IEEE Photonics Conference (IPC). 2022 (**Submitted**)
- [12]. **Liu, Z.**, Vasilyev, M., Pan, M., Sun, Y., Guo, C. & Zhou, W. "Full 2π phase shift from single and double layer photonic crystal slabs". 2021 IEEE Photonics Conference (IPC).2021, pp. 1-2 <https://doi:10.1109/ipc48725.2021.9593022>
- [13]. **Liu, Z.**, Ge, X., Chen, Y. & Zhou, W. in 2021 IEEE Photonics Conference (IPC), 1-2 (2021). <https://doi:10.1109/ipc48725.2021.9593039>
- [14]. **Liu, Z.**, Shin, J., Bai, W., Rogers, J. A. & Zhou, W. "Integrated Bioresorbable Optical Sensor Systems for Biomedical Pressure and Temperature Monitoring". 2019 IEEE Photonics Conference (IPC). 2019, pp.1-2 <https://doi:10.1109/IPCCon.2019.8908524>
- [15]. Kalapala, A., Reilly, K., Rotter, T., Gautum, C., Pan, M., Liu, Z., Chen, Y., Zhu, M., Bedford, R., Overman, L., Fan, S., Balakrishnan, G., & Zhou, W. “Impact of vavity resonance Detuning on Watt-level PCSEL”. 2022 IEEE Photonics Conference (IPC). 2022 (**Submitted**)
- [16]. Reilly, K. J., Kalapala, A., Song, A., Rotter, T., **Liu, Z.**, Renteria, E., Fan, S., Zhou, W. & Balakrishnan, G. "Fabrication of Photonic Crystal Surface Emitting Lasers (PCSELS) by Epitaxial Regrowth". Conference on Lasers and Electro-Optics. 2021, https://doi:10.1364/CLEO_AT.2021.JTu3A.78
- [17]. Ge, X., **Liu, Z.** & Zhou, W. "2D Material Printing for Cavity Integration". 2018 IEEE Research and Applications of Photonics In Defense Conference (RAPID). 2018, pp.1-2 <https://doi:10.1109/rapid.2018.8509019>

- [18]. Liu, S.-C., Zhao, D., Reuterskiöld-Hedlund, C., **Liu, Z.**, Hammar, M. & Zhou, W. "Electrically Pumped Hybrid III-V/Si Photonic Crystal Surface Emitting Lasers with Buried Tunnel-Junction". Conference on Lasers and Electro-Optics. 2018, https://doi:10.1364/cleo_si.2018.Sw3q.5

BIOGRAPHICAL STATEMENT

Zhonghe Liu was born in the northwestern part of China. He received his B.S. degree from Hunan University in 2011 in China, M.S. degree in Physics from the University of Oklahoma in 2016, and PhD. degree in Electrical Engineering from University of Texas at Arlington in 2022. His research interests are in semiconductor opto-electronic devices. His work has been focused on different types of Photonic Crystal (PC) lasers for higher power, low energy cost, and high speed applications. He also worked on passive PC applications such as PC membrane sensors, PC phase plate and meta-PC devices that are widely in demand for compact optical applications such as LiDAR system, Augmented Reality (AR) and Virtual Reality (VR) devices.

REFERENCES

- 1 Iadanza, S., Liles, A. A., Butler, S. M., Hegarty, S. P. & O’Faolain, L. Photonic crystal lasers: from photonic crystal surface emitting lasers (PCSELs) to hybrid external cavity lasers (HECLs) and topological PhC lasers [Invited]. *Optical Materials Express* **11**, (2021) doi:10.1364/ome.430748.
- 2 Li, Z., Lin, P., Huang, Y. W., Park, J. S., Chen, W. T. *et al.* Meta-optics achieves RGB-achromatic focusing for virtual reality. *Sci Adv* **7**, (2021) doi:10.1126/sciadv.abe4458.
- 3 Pahlevaninezhad, M., Huang, Y. W., Pahlevani, M., Bouma, B., Suter, M. J. *et al.* Metasurface-based bijective illumination collection provides high-resolution tomography in three dimensions. *Nat Photonics* **16**, 203-211, (2022) doi:10.1038/s41566-022-00956-6.
- 4 Kang, S.-K., Murphy, R. K., Hwang, S.-W., Lee, S. M., Harburg, D. V. *et al.* Bioresorbable silicon electronic sensors for the brain. *Nature* **530**, 71-76, (2016).
- 5 Luo, M., Martinez, A. W., Song, C., Herrault, F. & Allen, M. G. A microfabricated wireless RF pressure sensor made completely of biodegradable materials. *Journal of microelectromechanical systems* **23**, 4-13, (2013).
- 6 Shin, J., Yan, Y., Bai, W., Xue, Y., Gamble, P. *et al.* Bioresorbable pressure sensors protected with thermally grown silicon dioxide for the monitoring of chronic diseases and healing processes. *Nature biomedical engineering* **3**, 37-46, (2019).
- 7 Simon, S. H. *The Oxford Solid State Basics*. 1 edn, (Oxford University Press, 2013).
- 8 John D. Joannopoulos, S. G. J., Joshua N. Winn, and Robert D. Meade. *Photonic crystals molding the flow of light*. 2 edn, (Princeton University Press, 2008).
- 9 Liu, Y., Wang, S., Zhao, D., Zhou, W. & Sun, Y. High quality factor photonic crystal filter at k approximately 0 and its application for refractive index sensing. *Opt Express* **25**, 10536-10545, (2017) doi:10.1364/OE.25.010536.
- 10 Yang, H., Zhao, D., Chuwongin, S., Seo, J.-H., Yang, W. *et al.* Transfer-printed stacked nanomembrane lasers on silicon. *Nature Photonics* **6**, 615-620, (2012) doi:10.1038/nphoton.2012.160.
- 11 Liu, Z., Vasilyev, M., Pan, M., Sun, Y., Guo, C. *et al.* in *2021 IEEE Photonics Conference (IPC)* 1-2 (2021).
- 12 Qiang, Z. X., Yang, H. J., Chen, L., Pang, H. Q., Ma, Z. Q. *et al.* Fano filters based on transferred silicon nanomembranes on plastic substrates. *Appl Phys Lett* **93**, 061106, (2008) doi:10.1063/1.2971199.
- 13 Fan, S. & Joannopoulos, J. D. Analysis of guided resonances in photonic crystal slabs. *Physical Review B* **65**, (2002) doi:10.1103/PhysRevB.65.235112.
- 14 Kwon, S. H., Kim, S. H., Kim, S. K., Lee, Y. H. & Kim, S. B. Small, low-loss heterogeneous photonic bandedge laser. *Opt Express* **12**, 5356-5361, (2004) doi:10.1364/opex.12.005356.

- 15 Bordas, F., Steel, M. J., Seassal, C. & Rahmani, A. Confinement of band-edge modes in a photonic crystal slab. *Opt Express* **15**, 10890-10902, (2007) doi:10.1364/oe.15.010890.
- 16 Ferrier, L., Rojo-Romeo, P., Drouard, E., Letatre, X. & Viktorovitch, P. Slow Bloch mode confinement in 2D photonic crystals for surface operating devices. *Opt Express* **16**, 3136-3145, (2008) doi:10.1364/oe.16.003136.
- 17 Nedel, P., Letatre, X., Seassal, C., Auffeves, A., Ferrier, L. *et al.* Design and investigation of surface addressable photonic crystal cavity confined band edge modes for quantum photonic devices. *Opt Express* **19**, 5014-5025, (2011) doi:10.1364/OE.19.005014.
- 18 Giannopoulos, A. V., Li, Y. J., Long, C. M., Jin, J. M. & Choquette, K. D. Optical properties of photonic crystal heterostructure cavity lasers. *Opt Express* **17**, 5379-5390, (2009) doi:10.1364/oe.17.005379.
- 19 Srinivasan, K., Borselli, M. & Painter, O. Cavity Q, mode volume, and lasing threshold in small diameter AlGaAs microdisks with embedded quantum dots. *Optics Express* **14**, 1094-1105, (2006) doi:10.1364/OE.14.001094.
- 20 Shambat, G., Ellis, B., Petykiewicz, J., Mayer, M., Sarmiento, T. *et al.* Nanobeam photonic crystal cavity light-emitting diodes. *Applied Physics Letters* **99**, 71105-71105, (2011).
- 21 Ellis, B., Mayer, M., Shambat, G., Sarmiento, T., Harris, J. *et al.* Ultralow-threshold electrically pumped quantum-dot photonic-crystal nanocavity laser. *Nature Photonics* **5**, 297-300, (2011).
- 22 Zhang, Y., McCutcheon, M., Burgess, I. & Loncar, M. Ultra-high-Q TE/TM dual-polarized photonic crystal nanocavities. *Optics Letters* **34**, 2694-2696, (2009) doi:10.1364/OL.34.002694.
- 23 Liu, V. & Fan, S. S4 : A free electromagnetic solver for layered periodic structures. *Computer Physics Communications* **183**, 2233-2244, (2012) doi:10.1016/j.cpc.2012.04.026.
- 24 Kane, Y. Numerical solution of initial boundary value problems involving maxwell's equations in isotropic media. *IEEE Transactions on Antennas and Propagation* **14**, 302-307, (1966) doi:10.1109/tap.1966.1138693.
- 25 Oskooi, A. F., Roundy, D., Ibanescu, M., Bermel, P., Joannopoulos, J. D. *et al.* Meep: A flexible free-software package for electromagnetic simulations by the FDTD method. *Computer Physics Communications* **181**, 687-702, (2010) doi:10.1016/j.cpc.2009.11.008.
- 26 Hughes, T. W., Minkov, M., Liu, V., Yu, Z. & Fan, S. A perspective on the pathway toward full wave simulation of large area metalenses. *Appl Phys Lett* **119**, (2021) doi:10.1063/5.0071245.
- 27 Minkov, M., Williamson, I. A. D., Andreani, L. C., Gerace, D., Lou, B. *et al.* Inverse Design of Photonic Crystals through Automatic Differentiation. *ACS Photonics* **7**, 1729-1741, (2020) doi:10.1021/acsp Photonics.0c00327.
- 28 Jiang, G. Design challenges of implantable pressure monitoring system. *Front Neurosci* **4**, 29, (2010) doi:10.3389/neuro.20.002.2010.
- 29 Sit, A. J. Continuous monitoring of intraocular pressure: rationale and progress toward a clinical device. *J Glaucoma* **18**, 272-279, (2009) doi:10.1097/IJG.0b013e3181862490.

- 30 Yu, L., Kim, B. & Meng, E. Chronically Implanted Pressure Sensors: Challenges and State of the Field. *Sensors* **14**, 20620, (2014).
- 31 Poeggel, S., Tosi, D., Duraibabu, D., Leen, G., McGrath, D. *et al.* Optical Fibre Pressure Sensors in Medical Applications. *Sensors* **15**, 17115, (2015).
- 32 Taffoni, F., Formica, D., Saccomandi, P., Pino, G. & Schena, E. Optical Fiber-Based MR-Compatible Sensors for Medical Applications: An Overview. *Sensors* **13**, 14105, (2013).
- 33 Abi-Abdallah Rodriguez, D., Durand, E., de Rochefort, L., Boudjemline, Y. & Mousseaux, E. Simultaneous pressure-volume measurements using optical sensors and MRI for left ventricle function assessment during animal experiment. *Med Eng Phys* **37**, 100-108, (2015) doi:10.1016/j.medengphy.2014.11.004.
- 34 Newcombe, V. F., Hawkes, R. C., Harding, S. G., Willcox, R., Brock, S. *et al.* Potential heating caused by intraparenchymal intracranial pressure transducers in a 3-tesla magnetic resonance imaging system using a body radiofrequency resonator: assessment of the Codman MicroSensor Transducer. *J Neurosurg* **109**, 159-164, (2008) doi:10.3171/JNS/2008/109/7/0159.
- 35 Phang, I., Mada, M., Koliass, A. G., Newcombe, V. F. J., Trivedi, R. A. *et al.* Magnetic Resonance Imaging of the Codman Microsensor Transducer Used for Intraspinal Pressure Monitoring. *Spine* **41**, E605-E610, (2016) doi:10.1097/brs.0000000000001334.
- 36 Roguin, A., Schwitter, J., Vahlhaus, C., Lombardi, M., Brugada, J. *et al.* Magnetic resonance imaging in individuals with cardiovascular implantable electronic devices. *Europace* **10**, 336-346, (2008) doi:10.1093/europace/eun021.
- 37 Williams, E. J., Bunch, C. S., Carpenter, T. A., Downey, S. P., Kendall, I. V. *et al.* Magnetic resonance imaging compatibility testing of intracranial pressure probes. Technical note. *J Neurosurg* **91**, 706-709, (1999) doi:10.3171/jns.1999.91.4.0706.
- 38 Vanhoostenberghe, A. Implantable electronic devices technology challenges for long-term human implantation. *Sensor Review* **29**, 345-348, (2009) doi:10.1108/02602280910986593.
- 39 Boutry, C. M., Chandrahali, H., Streit, P., Schinhammer, M., Hanzi, A. C. *et al.* Towards biodegradable wireless implants. *Philos Trans A Math Phys Eng Sci* **370**, 2418-2432, (2012) doi:10.1098/rsta.2011.0439.
- 40 Chamis, A. L., Peterson, G. E., Cabell, C. H., Corey, G. R., Sorrentino, R. A. *et al.* Staphylococcus aureus bacteremia in patients with permanent pacemakers or implantable cardioverter-defibrillators. *Circulation* **104**, 1029-1033, (2001) doi:10.1161/hc3401.095097.
- 41 Hall-Stoodley, L., Costerton, J. W. & Stoodley, P. Bacterial biofilms: from the natural environment to infectious diseases. *Nat Rev Microbiol* **2**, 95-108, (2004) doi:10.1038/nrmicro821.
- 42 Kang, S. K., Murphy, R. K., Hwang, S. W., Lee, S. M., Harburg, D. V. *et al.* Bioresorbable silicon electronic sensors for the brain. *Nature* **530**, 71-76, (2016) doi:10.1038/nature16492.
- 43 Luo, M., Martinez, A. W., Song, C., Herrault, F. & Allen, M. G. A Microfabricated Wireless RF Pressure Sensor Made Completely of Biodegradable Materials. *Journal of Microelectromechanical Systems* **23**, 4-13, (2014) doi:10.1109/jmems.2013.2290111.

- 44 Shin, J., Yan, Y., Bai, W., Xue, Y., Gamble, P. *et al.* Bioresorbable pressure sensors protected with thermally grown silicon dioxide for the monitoring of chronic diseases and healing processes. *Nat Biomed Eng* **3**, 37-46, (2019) doi:10.1038/s41551-018-0300-4.
- 45 Hwang, S. W., Lee, C. H., Cheng, H., Jeong, J. W., Kang, S. K. *et al.* Biodegradable elastomers and silicon nanomembranes/nanoribbons for stretchable, transient electronics, and biosensors. *Nano Lett* **15**, 2801-2808, (2015) doi:10.1021/nl503997m.
- 46 Yu, K. J., Kuzum, D., Hwang, S. W., Kim, B. H., Juul, H. *et al.* Bioresorbable silicon electronics for transient spatiotemporal mapping of electrical activity from the cerebral cortex. *Nat Mater* **15**, 782-791, (2016) doi:10.1038/nmat4624.
- 47 Lee, G., Kang, S.-K., Won, S. M., Gutruf, P., Jeong, Y. R. *et al.* Fully Biodegradable Microsupercapacitor for Power Storage in Transient Electronics. *Advanced Energy Materials* **7**, 1700157-n/a, (2017) doi:10.1002/aenm.201700157.
- 48 Lee, Y. K., Yu, K. J., Song, E., Barati Farimani, A., Vitale, F. *et al.* Dissolution of Monocrystalline Silicon Nanomembranes and Their Use as Encapsulation Layers and Electrical Interfaces in Water-Soluble Electronics. *ACS Nano* **11**, 12562-12572, (2017) doi:10.1021/acsnano.7b06697.
- 49 Hwang, S. W., Tao, H., Kim, D. H., Cheng, H., Song, J. K. *et al.* A physically transient form of silicon electronics. *Science* **337**, 1640-1644, (2012) doi:10.1126/science.1226325.
- 50 Annese, V. F., Venuto, D. D., Martin, C. & Cumming, D. R. S. in *2014 21st IEEE International Conference on Electronics, Circuits and Systems (ICECS)*. 598-601 doi:10.1109/ICECS.2014.7050056.
- 51 Boutry, C. M., Nguyen, A., Lawal, Q. O., Chortos, A., Rondeau-Gagne, S. *et al.* A Sensitive and Biodegradable Pressure Sensor Array for Cardiovascular Monitoring. *Adv Mater* **27**, 6954-6961, (2015) doi:10.1002/adma.201502535.
- 52 Boutry, C. M., Kaizawa, Y., Schroeder, B. C., Chortos, A., Legrand, A. *et al.* A stretchable and biodegradable strain and pressure sensor for orthopaedic application. *Nature Electronics* **1**, 314-321, (2018) doi:10.1038/s41928-018-0071-7.
- 53 Hwang, S. W., Song, J. K., Huang, X., Cheng, H., Kang, S. K. *et al.* High-performance biodegradable/transient electronics on biodegradable polymers. *Adv Mater* **26**, 3905-3911, (2014) doi:10.1002/adma.201306050.
- 54 Kang, S.-K., Hwang, S.-W., Cheng, H., Yu, S., Kim, B. H. *et al.* Dissolution Behaviors and Applications of Silicon Oxides and Nitrides in Transient Electronics. *Advanced Functional Materials* **24**, 4427-4434, (2014) doi:10.1002/adfm.201304293.
- 55 Kang, S.-K., Hwang, S.-W., Yu, S., Seo, J.-H., Corbin, E. A. *et al.* Biodegradable Thin Metal Foils and Spin-On Glass Materials for Transient Electronics. *Advanced Functional Materials* **25**, 1789-1797, (2015) doi:10.1002/adfm.201403469.
- 56 Ye, Y., Wong, Z. J., Lu, X., Ni, X., Zhu, H. *et al.* Monolayer excitonic laser. *Nature Photonics* **9**, 733-737, (2015) doi:10.1038/nphoton.2015.197.
- 57 Wu, S., Buckley, S., Schaibley, J. R., Feng, L., Yan, J. *et al.* Monolayer semiconductor nanocavity lasers with ultralow thresholds. *Nature* **520**, 69-72, (2015) doi:10.1038/nature14290.

- 58 Salehzadeh, O., Djavid, M., Tran, N. H., Shih, I. & Mi, Z. Optically Pumped Two-Dimensional MoS₂ Lasers Operating at Room-Temperature. *Nano Lett* **15**, 5302-5306, (2015) doi:10.1021/acs.nanolett.5b01665.
- 59 Li, Y., Zhang, J., Huang, D., Sun, H., Fan, F. *et al.* Room-temperature continuous-wave lasing from monolayer molybdenum ditelluride integrated with a silicon nanobeam cavity. *Nat Nanotechnol* **12**, 987-992, (2017) doi:10.1038/nnano.2017.128.
- 60 Shang, J., Cong, C., Wang, Z., Peimyoo, N., Wu, L. *et al.* Room-temperature 2D semiconductor activated vertical-cavity surface-emitting lasers. *Nat Commun* **8**, 543, (2017) doi:10.1038/s41467-017-00743-w.
- 61 Fang, H., Liu, J., Li, H., Zhou, L., Liu, L. *et al.* 1305 nm Few-Layer MoTe₂-on-Silicon Laser-Like Emission. *Laser & Photonics Reviews* **12**, (2018) doi:10.1002/lpor.201800015.
- 62 Withers, F., Del Pozo-Zamudio, O., Mishchenko, A., Rooney, A. P., Gholinia, A. *et al.* Light-emitting diodes by band-structure engineering in van der Waals heterostructures. *Nat Mater* **14**, 301-306, (2015) doi:10.1038/nmat4205.
- 63 Liu, C. H., Clark, G., Fryett, T., Wu, S., Zheng, J. *et al.* Nanocavity Integrated van der Waals Heterostructure Light-Emitting Tunneling Diode. *Nano Lett* **17**, 200-205, (2017) doi:10.1021/acs.nanolett.6b03801.
- 64 Yang, W., Shang, J., Wang, J., Shen, X., Cao, B. *et al.* Electrically Tunable Valley-Light Emitting Diode (vLED) Based on CVD-Grown Monolayer WS₂. *Nano Lett* **16**, 1560-1567, (2016) doi:10.1021/acs.nanolett.5b04066.
- 65 Bie, Y. Q., Grosso, G., Heuck, M., Furchi, M. M., Cao, Y. *et al.* A MoTe₂-based light-emitting diode and photodetector for silicon photonic integrated circuits. *Nat Nanotechnol* **12**, 1124-1129, (2017) doi:10.1038/nnano.2017.209.
- 66 Lien, D. H., Amani, M., Desai, S. B., Ahn, G. H., Han, K. *et al.* Large-area and bright pulsed electroluminescence in monolayer semiconductors. *Nat Commun* **9**, 1229, (2018) doi:10.1038/s41467-018-03218-8.
- 67 Castellanos-Gomez, A., Buscema, M., Molenaar, R., Singh, V., Janssen, L. *et al.* Deterministic transfer of two-dimensional materials by all-dry viscoelastic stamping. *2D Materials* **1**, (2014) doi:10.1088/2053-1583/1/1/011002.
- 68 Kwon, S.-H., Kim, S.-H., Kim, S.-K., Lee, Y.-H. & Kim, S.-B. Small, low-loss heterogeneous photonic bandedge laser. *Opt. Express* **12**, 5356-5361, (2004).
- 69 Bordas, F., Steel, M. J., Seassal, C. & Rahmani, A. Confinement of band-edge modes in a photonic crystal slab. *Opt. Express* **15**, 10890-10902, (2007).
- 70 Ferrier, L., Rojo-Romeo, P., Drouard, E., Letartre, X. & Viktorovitch, P. Slow Bloch mode confinement in 2D photonic crystals for surface operating devices. *Opt. Express* **16**, 3136-3145, (2008).
- 71 Chua, S.-L., Chong, Y., Stone, A. D., Soljačić, M. & Bravo-Abad, J. Low-threshold lasing action in photonic crystal slabs enabled by Fano resonances. *Opt. Express* **19**, 1539-1562, (2011).
- 72 Giannopoulos, A. V., Li, Y.-J., Long, C. M., Jin, J.-M. & Choquette, K. D. Optical properties of photonic crystal heterostructure cavity lasers. *Opt. Express* **17**, 5379-5390, (2009).

- 73 Lee, J., Zhen, B., Chua, S.-L., Qiu, W., Joannopoulos, J. D. *et al.* Observation and differentiation of unique high-Q optical resonances near zero wave vector in macroscopic photonic crystal slabs. *Phys. Rev. Lett.* **109**, 067401-067401, (2012).
- 74 Ge, X., Minkov, M., Fan, S., Li, X. & Zhou, W. Low index contrast heterostructure photonic crystal cavities with high quality factors and vertical radiation coupling. *Appl Phys Lett* **112**, (2018) doi:10.1063/1.5026433.
- 75 Ge, X. C., Minkov, M., Fan, S. H., Li, X. L. & Zhou, W. D. Laterally confined photonic crystal surface emitting laser incorporating monolayer tungsten disulfide. *Npj 2d Materials and Applications* **3**, (2019) doi:10.1038/s41699-019-0099-1.
- 76 Ge, X., Minkov, M., Choudhury, T., Chubarov, M., Fan, S. *et al.* in *2018 IEEE International Semiconductor Laser Conference (ISLC)* 1-2 (2018).
- 77 Ge, X. C., Minkov, M., Fan, S. H., Li, X. L. & Zhou, W. D. Low index contrast heterostructure photonic crystal cavities with high quality factors and vertical radiation coupling. *Appl Phys Lett* **112**, 141105, (2018) doi:10.1063/1.5026433.
- 78 Ge, X. C., Minkov, M., Fan, S. H., Li, X. L. & Zhou, W. D. Laterally confined photonic crystal surface emitting laser incorporating monolayer tungsten disulfide. *Npj 2d Materials and Applications* **3**, 16, (2019) doi:<https://doi.org/10.1038/s41699-019-0099-1>.
- 79 Joannopoulos, J. D., Villeneuve, P. R. & Fan, S. Photonic crystals: putting a new twist on light. *Nature* **386**, 143-149, (1997).
- 80 Johnson, S. G., Fan, S., Villeneuve, P. R., Joannopoulos, J. D. & Kolodziejski, L. Guided modes in photonic crystal slabs. *Physical Review B* **60**, 5751, (1999).
- 81 Fan, S. & Joannopoulos, J. D. Analysis of guided resonances in photonic crystal slabs. *Physical Review B* **65**, 235112, (2002).
- 82 John D. Joannopoulos, S. G. J., Joshua N. Winn, and Robert D. Meade. *Photonic Crystals: Molding the Flow of Light*. (Princeton Univ. Press, 2008).
- 83 Zhou, W., Zhao, D., Shuai, Y.-C., Yang, H., Chuwongin, S. *et al.* Progress in 2D photonic crystal Fano resonance photonics. *Progress in Quantum Electronics* **38**, 1-74, (2014) doi:10.1016/j.pquantelec.2014.01.001.
- 84 Sauvan, C., Lecamp, G., Lalanne, P. & Hugonin, J. Modal-reflectivity enhancement by geometry tuning in Photonic Crystal microcavities. *Opt Express* **13**, 245-255, (2005) doi:10.1364/opex.13.000245.
- 85 Deotare, P. B., McCutcheon, M. W., Frank, I. W., Khan, M. & Loncar, M. High quality factor photonic crystal nanobeam cavities. *Appl Phys Lett* **94**, 121106, (2009) doi:10.1063/1.3107263.
- 86 Burek, M. J., Chu, Y., Liddy, M. S., Patel, P., Rochman, J. *et al.* High quality-factor optical nanocavities in bulk single-crystal diamond. *Nat Commun* **5**, 5718, (2014) doi:10.1038/ncomms6718.
- 87 Shambat, G., Ellis, B., Petykiewicz, J., Mayer, M. A., Sarmiento, T. *et al.* Nanobeam photonic crystal cavity light-emitting diodes. *Appl Phys Lett* **99**, 071105, (2011) doi:10.1063/1.3625432.

- 88 Yang, D., Liu, X., Li, X., Duan, B., Wang, A. *et al.* Photonic crystal nanobeam cavity devices for on-chip integrated silicon photonics. *Journal of Semiconductors* **42**, 023103, (2021) doi:10.1088/1674-4926/42/2/023103.
- 89 Trivino, N. V., Butte, R., Carlin, J. F. & Grandjean, N. Continuous wave blue lasing in III-nitride nanobeam cavity on silicon. *Nano Lett* **15**, 1259-1263, (2015) doi:10.1021/nl504432d.
- 90 Jeong, K.-Y., No, Y.-S., Hwang, Y., Kim, K. S., Seo, M.-K. *et al.* Electrically driven nanobeam laser. *Nature Communications* **4**, 2822, (2013) doi:10.1038/ncomms3822.
- 91 He, Z., Chen, B., Hua, Y., Liu, Z. J., Wei, Y. M. *et al.* CMOS Compatible High-Performance Nanolasing Based on Perovskite-SiN Hybrid Integration. *Advanced Optical Materials* **8**, 2000453, (2020) doi:10.1002/adom.202000453.
- 92 Yang, Z., Pelton, M., Fedin, I., Talapin, D. V. & Waks, E. A room temperature continuous-wave nanolaser using colloidal quantum wells. *Nat Commun* **8**, 143, (2017) doi:10.1038/s41467-017-00198-z.
- 93 Shakoor, A., Nozaki, K., Kuramochi, E., Nishiguchi, K., Shinya, A. *et al.* Compact 1D-silicon photonic crystal electro-optic modulator operating with ultra-low switching voltage and energy. *Opt Express* **22**, 28623-28634, (2014) doi:10.1364/OE.22.028623.
- 94 Javid, M. R., Miri, M. & Zarifkar, A. Design of a compact high-speed optical modulator based on a hybrid plasmonic nanobeam cavity. *Optics Communications* **410**, 652-659, (2018) doi:10.1016/j.optcom.2017.11.016.
- 95 Hadian Siahkal-Mahalle, B. & Abedi, K. Ultra-compact low loss electro-optical nanobeam cavity modulator embedded photonic crystal. *Optical and Quantum Electronics* **51**, 128, (2019) doi:10.1007/s11082-019-1835-7.
- 96 Cheng, Z., Dong, J. & Zhang, X. Ultracompact optical switch using a single semisymmetric Fano nanobeam cavity. *Opt Lett* **45**, 2363-2366, (2020) doi:10.1364/OL.383250.
- 97 Soref, R. & Hendrickson, J. Proposed ultralow-energy dual photonic-crystal nanobeam devices for on-chip N x N switching, logic, and wavelength multiplexing. *Opt Express* **23**, 32582-32596, (2015) doi:10.1364/OE.23.032582.
- 98 Meng, Z. M., Chen, C. B. & Qin, F. Theoretical investigation of integratable photonic crystal nanobeam all-optical switching with ultrafast response and ultralow switching energy. *J Phys D Appl Phys* **53**, 205105, (2020) doi:10.1088/1361-6463/ab768c.
- 99 Yang, D. Q., Kita, S., Liang, F., Wang, C., Tian, H. P. *et al.* High sensitivity and high Q-factor nanoslot parallel quadrabeam photonic crystal cavity for real-time and label-free sensing. *Appl Phys Lett* **105**, 063118, (2014) doi:10.1063/1.4867254.
- 100 Dong, P., Qian, W., Liang, H., Shafiiha, R., Feng, N. N. *et al.* Low power and compact reconfigurable multiplexing devices based on silicon microring resonators. *Opt Express* **18**, 9852-9858, (2010) doi:10.1364/OE.18.009852.
- 101 Dong, P., Qian, W., Liang, H., Shafiiha, R., Feng, D. *et al.* Thermally tunable silicon racetrack resonators with ultralow tuning power. *Opt Express* **18**, 20298-20304, (2010) doi:10.1364/OE.18.020298.
- 102 Zhang, J. & He, S. Cladding-free efficiently tunable nanobeam cavity with nanotentacles. *Opt Express* **25**, 12541-12551, (2017) doi:10.1364/OE.25.012541.

- 103 Quan, Q. & Loncar, M. Deterministic design of wavelength scale, ultra-high Q photonic crystal nanobeam cavities. *Opt Express* **19**, 18529-18542, (2011) doi:10.1364/OE.19.018529.
- 104 Khorasaninejad, M., Chen, W. T., Devlin, R. C., Oh, J., Zhu, A. Y. *et al.* Metalenses at visible wavelengths: Diffraction-limited focusing and subwavelength resolution imaging. *Science* **352**, 1190-1194, (2016) doi:10.1126/science.aaf6644.
- 105 Dharmavarapu, R., Izumi, K.-i., Katayama, I., Ng, S. H., Vongsvivut, J. *et al.* Dielectric cross-shaped-resonator-based metasurface for vortex beam generation at mid-IR and THz wavelengths. *Nanophotonics* **8**, 1263-1270, (2019) doi:10.1515/nanoph-2019-0112.
- 106 Ni, Y., Chen, S., Wang, Y., Tan, Q., Xiao, S. *et al.* Metasurface for Structured Light Projection over 120 degrees Field of View. *Nano Lett* **20**, 6719-6724, (2020) doi:10.1021/acs.nanolett.0c02586.
- 107 Hu, T., Zhong, Q., Li, N., Dong, Y., Xu, Z. *et al.* CMOS-compatible a-Si metalenses on a 12-inch glass wafer for fingerprint imaging. *Nanophotonics* **9**, 823-830, (2020) doi:10.1515/nanoph-2019-0470.
- 108 Mikheeva, E., Claude, J. B., Salomoni, M., Wenger, J., Lumeau, J. *et al.* CMOS-compatible all-dielectric metalens for improving pixel photodetector arrays. *APL Photonics* **5**, (2020) doi:10.1063/5.0022162.
- 109 Arbabi, A., Horie, Y., Ball, A. J., Bagheri, M. & Faraon, A. Subwavelength-thick lenses with high numerical apertures and large efficiency based on high-contrast transmitarrays. *Nat Commun* **6**, 7069, (2015) doi:10.1038/ncomms8069.
- 110 Byrnes, S. J., Lenef, A., Aieta, F. & Capasso, F. Designing large, high-efficiency, high-numerical-aperture, transmissive meta-lenses for visible light. *Opt Express* **24**, 5110-5124, (2016) doi:10.1364/OE.24.005110.
- 111 Liang, H., Martins, A., Borges, B.-H. V., Zhou, J., Martins, E. R. *et al.* High performance metalenses: numerical aperture, aberrations, chromaticity, and trade-offs. *Optica* **6**, (2019) doi:10.1364/optica.6.001461.
- 112 Lin, K.-F., Hsieh, C.-C., Hsin, S.-C., Hsieh, W.-F., Chang-Hasnain, C. J. *et al.* in *High Contrast Metastructures IX* (2020).
- 113 Wang, Z., Li, Q. & Yan, F. A high numerical aperture terahertz all-silicon metalens with sub-diffraction focus and long depth of focus. *Journal of Physics D: Applied Physics* **54**, (2020) doi:10.1088/1361-6463/abc3ee.
- 114 Chung, H. & Miller, O. D. High-NA achromatic metalenses by inverse design. *Opt Express* **28**, 6945-6965, (2020) doi:10.1364/OE.385440.
- 115 Wang, S. W., Lai, J. J., Wu, T., Li, X. P. & Sun, J. Q. Wide-band achromatic metalens for visible light by dispersion compensation method. *J Phys D Appl Phys* **50**, (2017) doi:10.1088/1361-6463/aa8c90.
- 116 Chen, W. T., Zhu, A. Y., Sanjeev, V., Khorasaninejad, M., Shi, Z. *et al.* A broadband achromatic metalens for focusing and imaging in the visible. *Nat Nanotechnol* **13**, 220-226, (2018) doi:10.1038/s41565-017-0034-6.
- 117 Huang, Z., Qin, M., Guo, X., Yang, C. & Li, S. Achromatic and wide-field metalens in the visible region. *Opt Express* **29**, 13542-13551, (2021) doi:10.1364/OE.422126.

- 118 Badloe, T., Kim, I., Kim, Y., Kim, J. & Rho, J. Electrically Tunable Bifocal Metalens with Diffraction-Limited Focusing and Imaging at Visible Wavelengths. *Adv Sci (Weinh)* **8**, e2102646, (2021) doi:10.1002/advs.202102646.
- 119 Song, Y., Liu, W., Wang, X., Wang, F., Wei, Z. *et al.* Multifunctional Metasurface Lens With Tunable Focus Based on Phase Transition Material. *Frontiers in Physics* **9**, (2021) doi:10.3389/fphy.2021.651898.
- 120 Tan, Z., Fan, F., Zhao, D., Li, S., Wang, X. *et al.* Linear-polarized terahertz isolator by breaking the gyro-mirror symmetry in cascaded magneto-optical metagrating. *Nanophotonics* **10**, 4141-4148, (2021) doi:10.1515/nanoph-2021-0416.
- 121 Zaidi, A., Rubin, N. A., Dorrah, A. H., Park, J. S. & Capasso, F. Generalized polarization transformations with metasurfaces. *Opt Express* **29**, 39065-39078, (2021) doi:10.1364/OE.442844.
- 122 Rubin, N. A., Shi, Z. & Capasso, F. Polarization in diffractive optics and metasurfaces. *Advances in Optics and Photonics* **13**, (2022) doi:10.1364/aop.439986.
- 123 Schinke, C., Christian Peest, P., Schmidt, J., Brendel, R., Bothe, K. *et al.* Uncertainty analysis for the coefficient of band-to-band absorption of crystalline silicon. *AIP Advances* **5**, (2015) doi:10.1063/1.4923379.
- 124 Pierce, D. T. & Spicer, W. E. Electronic Structure of Amorphous Si from Photoemission and Optical Studies. *Physical Review B* **5**, 3017-3029, (1972) doi:10.1103/PhysRevB.5.3017.
- 125 Overvig, A. C., Malek, S. C. & Yu, N. Multifunctional Nonlocal Metasurfaces. *Phys Rev Lett* **125**, 017402, (2020) doi:10.1103/PhysRevLett.125.017402.
- 126 Zhou, W. & Fan, S. in *Semiconductors and Semimetals* Vol. 100 (eds Weidong Zhou & Shanhui Fan) 149-188 (Elsevier, 2019).
- 127 Pan, M., Liu, Z., Kalapala, A., Chen, Y., Sun, Y. *et al.* Complete 2π phase control by photonic crystal slabs. *Optics Express* **29**, 40795-40803, (2021).